Modelling the kinematics of the cold gas in galaxies using GalAPAGOS

Author:

Keagan A. W. Blanchette

A Thesis submitted to the Faculty of Graduate Studies of

The University of Manitoba

in partial fulfillment of the requirements of the degree of

MASTER OF SCIENCE

Department of Physics and Astronomy

University of Manitoba

Winnipeg

Copyright © 2018 by Keagan A. W. Blanchette

Abstract

Galaxy rotation curves are the primary method of investigation into galaxy kinematics in this work. The University of Manitoba developed software package GalAPAGOS was renovated for optically thin gas, as well as used to generate the galaxy rotation curves. GalAPAGOS uses analytic fitting equations to produce models and describe the galaxy kinematics, as well as the density distribution.

GalAPAGOS was applied to both HI and CO observational spectral line cubes to demonstrate that these model rotation curves and density profiles would benefit studies of normal galaxies (e.g. NGC 3198), peculiar galaxies (e.g. NGC 2188), and the centres of ellipticals (e.g. NGC 3665). The family of models generated for each galaxy were able to accurately reproduce the morphology and kinematic characteristics of these galaxies, along with density profiles and rotation curves. We then used the rotation curves to calculate the total dynamical mass inside the radius of the observed gas disk.

Acknowledgments

Firstly, I would like to thank my supervisor, Dr. Jayanne English, for all her help, expertise, ideas, and all the skills and knowledge she has taught me.

I would also like to thank my co-supervisor, Dr. Jason Fiege, for all the computational resources he provided, as well as assistance with the coding of GalAPAGOS and mathematical subtleties involved in this project.

Thanks to Dr. Martin Bureau for helping to provide me with an opportunity to travel and work at the University of Oxford, as well as providing valuable help and insights, as well as sharing some of the CO data used.

Thanks to Dr. Timothy Davis and Kyoko Onishi for providing molecular gas data. Thanks to Dr. Theresa van Vliet Wiegert for her help with the construction of channel maps.

Thanks to the astronomy group at the University of Manitoba, including: Dr. Chris O'Dea, Dr. Samar Safi-Harb, Ben, Chelsea, Erica, Kelvin, and Robert. Thanks to Maiko for all the computer support.

Thanks to Josh for reading a very early draft of this thesis and giving valuable feedback.

Thank you to all my wonderful family and friends who have been so supportive and helped keep me mostly sane through the course of this project.

A special thanks to Auja, who has been there for me, helped with editing, and done anything else she could to help.

I would like to acknowledge the V-P Office of Research, Department of Physics & Astronomy, and the Faculty of Science at the University of Manitoba, as well as the Natural Sciences and Engineering Research Council of Canada (NSERC) for financial support.

Contents

List of Tables

List of Figures

1 Introduction

"It's the questions we can't answer that teach us the most. They teach us how to think. If you give a man an answer, all he gains is a little fact. But give him a question and he'll look for his own answers."

— Patrick Rothfuss

1.1 Overview

This project studies the kinematics of galaxies by building a model galaxy based on existing data, and deriving galaxy properties from our model parameters. We used the GalAPAGOS (Galaxy Astrophysical Parameter Acquisition by Genetic Optimization Software) (Section 1.7) modelling environment, under development by Dr. Jason Fiege and Dr. Jayanne English. I contributed some additional capabilities (outlined in Section 1.7) throughout the course of this project. GalAPAGOS uses the Ferret (Section 1.6) evolutionary optimizer [Fiege, 2010], also developed by Dr. Jason Fiege.

GalAPAGOS generates a galaxy model based on the observational data input, and searches for the parameter set (see Section 1.7.2) for which the resulting model best matches the observational data. It constructs a model with the same resolution, same number of voxels, and same number of velocity channels as the input data. A voxel is a value on a regular grid in three-dimensional space, and is analogous to a pixel in a bitmap.

The scientific goal of this project is to investigate the central kinematics and outer rotational behaviour of galaxies. This is accomplished by applying GalAPAGOS to both neutral hydrogen (HI) and carbon monoxide (CO) observational data. GalAPAGOS is capable of modelling both the galaxy's rotation curve and its density distribution. A galaxy's rotation curve is the distribution of the radial velocity of a galaxy as a function of the distance from the galaxy's center corrected for the inclination of the galaxy to the observer's line of sight. A galaxy's density profile is the galaxy's column density as

a function of radius. The column density is the total the number of particles, within a specified unit area, summed along a line-of-sight velocity range. In our case this is the number of particles within 1 square metre integrated along a column with the length of the velocity range of the data cube. At the beginning of this project, only lower resolution (> 20") HI data were available. The use of higher resolution (≈ 4") CO data allows the model to constrain a galaxy's central kinematics by providing a larger number of resolution elements over distances associated with a rapid change in velocity.

The kinematic information revealed to us by modelling the data can be used to provide insight to several aspects of galaxy formation and evolution, such as the dark matter (DM) mass (Section 1.2) and the density distribution of DM (Section 1.4). Another application for this work is to use the model generated by GalAPAGOS as a mask over specific spatial regions of the data, which allows one to examine the remaining data for additional details associated with galaxy evolution (Section 1.3).

In Chapter 1, a brief description of the astronomical phenomena that we investigate in this research is presented, as well as information on the computational techniques used. With an understanding of the background knowledge, we move on to a mathematical description of the workings of GalAPAGOS in Chapter 2. Details on the data used, both artificial and observational, is presented in Chapter 3. Chapter 4 gives an overview of the analytical techniques used throughout this research, before moving on to the results in Chapter 5. Chapter 6 discusses the implications of the results for the three different galaxies that we examined using GalAPAGOS (NGC 2188, NGC 3198, and NGC 3665). Finally, a brief summary of the findings, discussion, and ideas for potential future project directions are outlined in Chapter 7. Note that all technical terms are defined in the Glossary, located at the end of the thesis.

1.2 Dark Matter

Dark Matter (DM) refers to matter measured to be present in galaxies using observational data, however we cannot observe it directly as it emits little or no light, hence the title

"dark" matter. In order for galaxy rotation curves (see Section 2.1), to behave as they do, galaxies must have on average roughly four times the mass calculated using the light from the galaxy [Sparke and Gallagher, 2007]. Early evidence of DM dates back to the 1920's, coming from vertical oscillations of stars around the Galactic plane [Jeans, 1922], and in the 1930's from the dynamics of galaxies in clusters [Zwicky, 1933].

It was found that unlike with other systems, such as planets orbiting stars, where most of the mass is in the center, the orbital velocities of galaxies flatten to a constant velocity value far from the center. This observation is now modelled by the galaxy being composed of an approximately radially exponential spatial distribution of stellar matter that tends to decrease further from the galaxy center, along with a (typically) ellipsiodal DM halo extending past the gas disk radius of the galaxy (Fig. 9) [Bak and Statler, 2000].

More evidence for DM comes from gravitational lensing [Bertone, 2010]. These lenses are a prediction of Einstein's theory of General Relativity. The effect of gravitational lenses is due to curved gravitational fields caused by large mass concentrations deflecting the light path of photons. This modifies the apparent flux and morphology of a background galaxy due to the mass of the foreground object. The modified apparent flux and morphology often results in galaxies having visible distortions such as Einstein rings, arcs, or multiple images of the galaxy. Gravitational lensing therefore allows us to measure the mass of an object without relying on its dynamics.

Even more evidence for DM comes from fluctuations in the cosmic microwave background. Using surveys such as the Planck survey [Collaboration, 2016] and the Wilkinson Microwave Anisotropy Probe (WMAP) [Bennet et al., 2013], it was determined that the typical angular size of a fluctuation in the cosmic microwave background is approximately 1 degree. This result is in agreement with the Λ Cold DM (ΛCDM) theory, in which DM is a necessary feature. From this theory, it is estimated that up to 85% of the mass in the universe is comprised of DM.

Although such a large percentage of the universe consists of DM, we are still unsure of the physical nature of all DM. In this project, we focus on the kinematics of three individual

galaxies, a normal spiral galaxy (NGC 3198), an early-type galaxy (NGC 3665), and a peculiar galaxy (NGC 2188). These kinematics can then be used to find the total dynamical mass of a galaxy, which includes the amount of DM.

1.3 Inflow and Outflow

"Inflow" and "Outflow" are terms used to describe how a galaxy interacts with the surrounding circumgalactic medium (CGM) and intergalactic medium (IGM). An inflow is a mass flow from the CGM and IGM to the galaxy. Outflow describes mass being transferred from the galaxy to the IGM. Although there are more processes through which a galaxy may interact with the IGM, the following discussion will be confined to inflow and outflow processes. The primary effect of inflows and outflows in terms of galaxy evolution, is to regulate the star formation rate (SFR) in galaxies. They also impact galaxy morpholgy.

The primary inflow process relevant to the galaxies studied in this project is cosmic inflow along the Large Scale Structure (large scale structure) (the structure of the universe on scales larger than that of a galaxy), an example of which is shown in Fig. 1. The accretion of gas from the cosmic web has been predicted by numerical simulations (e.g. [Dekel and Birnboim, 2006]) and is thought to contribute significantly to the formation of disk galaxies [Almeida et al., 2014]. The gas flowing into the galaxy originates outside of the virial radius (the furthest radius at which objects are still gravitationally bound to the galaxy) of the DM halo in which the galaxy resides, and through accretion over cosmic time scales (6-8 Gyrs), it contributes to the reservoir of baryons used for star formation. There are generally two modes for inflow from the cosmic web, hot and cold, both occurring simultaneously in all galaxies.

The "hot" mode occurs when the infalling gas encounters a large DM halo ($> 10^{12} M_{\odot}$). It becomes shock heated and becomes cooled over a long period of time ($\approx$Gyrs) and subsequently settles into the galaxy disk. The "cool" mode occurs when the gas meets a less massive halo, the infalling cool gas can arrive at the inner halo or disk directly. This

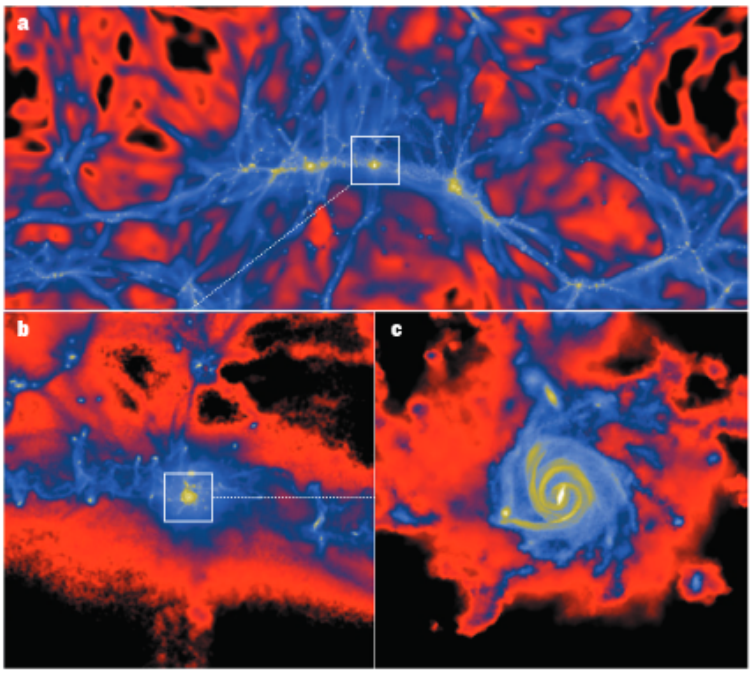

Figure 1: Taken from [Braun, 2013]. Above is a numerical simulation of galaxy formation and evolution, which shows an example of inflow of ionized gas along filaments in the intergalactic environment. In this sequence (**a**-**c**), the colour map is different for each level, but in all images green denotes higher gas density, and black denotes lower gas density.

cold flow accretion is thought to be the main mode of galaxy growth in early times, since high redshift haloes are generally lower in mass compared to low redshift haloes. There are also many examples of cool flow at low-redshift, provided by early-type galaxies, which typically have a mass of $> 10^{12} M_{\odot}$.

Outflow processes can generally fall into two categories: internal and external. The external example most relevant to this project is the phenomenon of tidal events, arising primarily through galaxy interactions. Galaxy interactions can consist of events such as a galaxy merger, where two or more galaxies "collide" and the gas, stars, and DM in each galaxy are affected by the colliding galaxy or galaxies. These interactions can be seen visually in the form of tidal tails and bridges, which are typically a thin, elongated region of stars and gas stretching out from the interacting galaxy's disk. Radio HI gas data can highlight these tidal interactions, as well as give information on their kinematics. An example of tidal tails in HI gas is the M81 group, shown in Fig. 2.

Ram pressure stripping is another example of an external process, an example of which

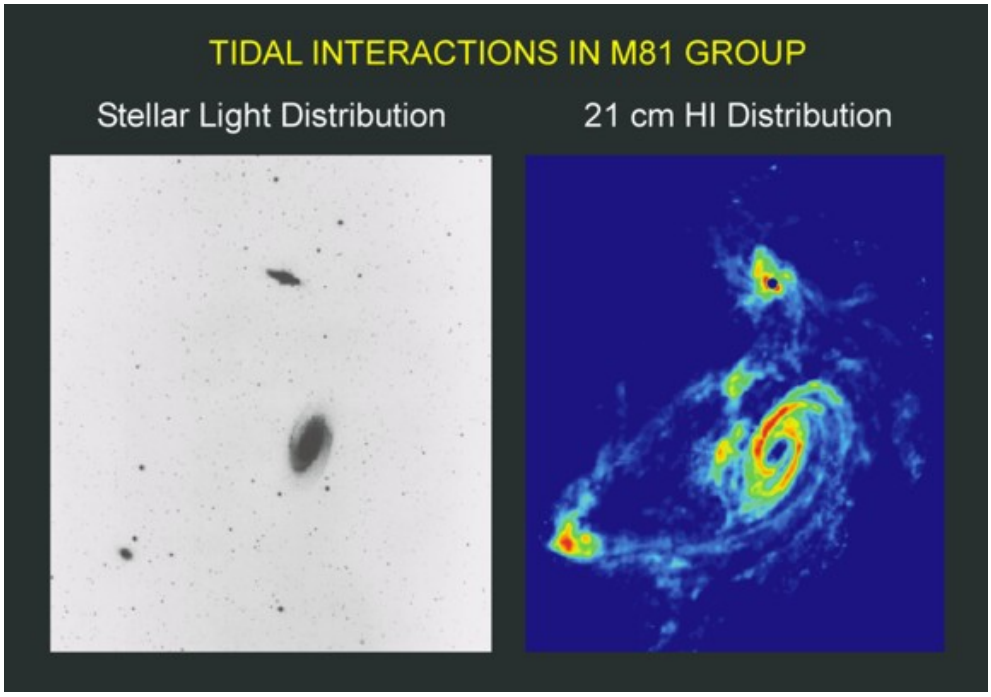

Figure 2: M81 group - The left image (from Digital Sky Survey) is an optical image of the M81 group of galaxies. The right image, made with the VLA, illustrates how the HI gas highlights the dramatic interactions occurring in the M81 group. Looking at the optical image, it is not clear that these are not isolated objects, while looking at the HI image makes it clear that this is an interacting group of galaxies. Image courtesy of NRAO/AUI [NRA, 2017], from [Yun et al., 1994].

is shown in Fig. 3. Some distinctive characteristics of ram pressure stripping include: a strongly disturbed morphology indicative of unilateral external forces, a pronounced brightness and color gradient suggesting extensive triggered star formation, compelling evidence of a debris trail, and the direction of motion of the aforementioned properties must be consistent with each other.

Another outflow process relevant to our studies is the creation of "superbubbles" in the interstellar medium (ISM), which is associated with supernovae and/or winds produced by massive stars in clusters often confined to the galaxy disk. These supernovae or star clusters can produce bubbles in the ISM that expand, becoming superbubbles. An example of this phenomena can be seen in Fig. 4. These superbubbles can burst out from the galaxy disk producing collimated outflows into the galactic halo. The collimated structures formed through this process are known as "chimneys". The signature of the exchange between the disk and the halo is typically high velocity red or blue-shifted

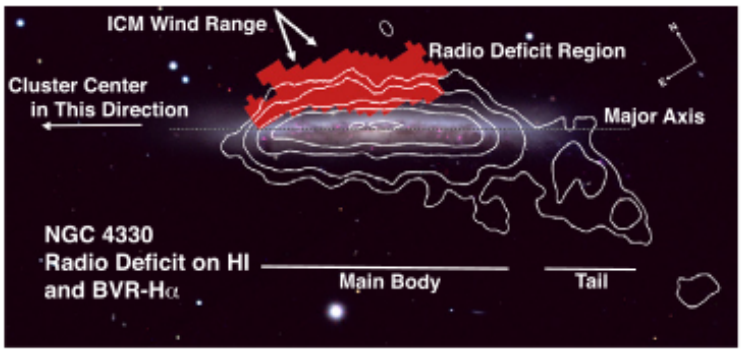

Figure 3: NGC 4330 - Taken from [Abramson et al., 2011]. Above is a BVR-Hα image with a radio deficit region (highlighted in red, and believed to be a tracer of ram pressure stripping), and HI contours (highlighted in white). A radio deficit region is a region where the flux is less than 50% of the expected value [Murphy et al., 2009]. The "wind" causing the ram pressure stripping is highlighted, and the typical disturbed morphology caused by a unilateral force is clearly visible.

(relative to the center-of-mass frame) gas away from the disk of the galaxy (extraplanar gas). The interaction can also be inferred by the presence of HI holes, extraplanar ionized gas, and radio haloes. This is an internal outflow process.

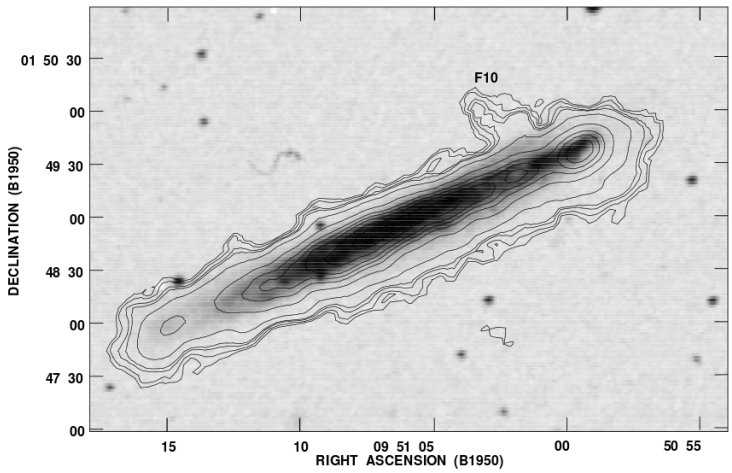

Figure 4: NGC 3044 - Taken from [Lee and Irwin, 1997]. Above is a column density map of NGC 3044, superimposed on the optical Digital Sky Survey image, highlighting the superbubble which is visible in the upper right of the image, and is labelled F10.

With GalAPAGOS, we model the velocities of the regularly rotating gas disk. We then use a standard radio astronomy technique called "masking" to set the pixels in the observed data cube to zero in the regularly rotating disk region. This region is determined by modelling the velocities of the gas disk using GalAPAGOS. The resulting data cube highlights observed gas features that are often dominated by interesting, anomalous ve-

locity behaviour. These features can then be analyzed to look for signatures of inflow or outflow processes. We apply this technique to the HI data cube (see Section 6.2) of nearby peculiar galaxy NGC 2188.

GalAPAGOS could potentially be applied in this way to the thousands of peculiar and interesting galaxies that are expected to be detected using the upcoming Square Kilometer Array (SKA). Using GalAPAGOS as described above to model these interesting galaxies revealed by the SKA would further our understanding of galaxies and the processes that dominate their evolution.

1.4 The Core/Cusp Problem

In the inner parts of galaxies there is typically a higher concentration of stars, which dominate a large fraction of the observed rotational velocity [de Blok, 2010]. As a result, there is a transition between the inner parts where stars dominate the rotation to an outer part driven by DM. In the inner parts of the galaxy, DM is still present and observational data from dwarf galaxies tells us the rotational velocity associated with this inner DM increases approximately linearly with radius. From this solid-body like behaviour, it is implied that there exists a central core in the DM distribution, as we show later in this section. The typical model used to represent "cored" models is the pseudo-isothermal (PI) sphere model [Begeman et al., 1991]. Note that it is also common to adopt a non-singular isothermal sphere, and that the choice between the two does not have a significant impact on the results. The approximation made by the PI sphere model is advantageous in that it does not depend on the velocity dispersion. The mass density distribution of the PI sphere is given by

$$\rho_{PI}(r) = \frac{\rho_0}{1 + (r/R_c)^2}, \tag{1.1}$$

where ρ_0 is the central halo density, r is the galaxy radius, and R_c is the core radius of the halo. In this PI model, the temperature is constant, the central density is assumed to be constant, and $r < R_c$, gives $\rho \propto r^0$.

However, when we look at the results of Navarro-Frenk-White (NFW) [Navarro et al., 1997] numerical N-body simulations of DM haloes based on the collisionless cold DM (CDM) theory, they do not show the expected core-like behaviour. Rather the inner parts of the distribution are better described by a steep power law mass-density distribution, referred to as the "cusp". It was found that the mass-distributions derived from these simulations were fit well by an inner DM density distribution of $\rho \sim r^{\alpha}$ with $\alpha = -1$ [Dubinsky and Carlberg, 1991].

These two different α values ($\alpha = 0$ for the PI model, and $\alpha = -1$ from the simulations) lead to very different descriptions of the DM distribution in galaxies in their centres, shown in Eq. 1.2b and Eq. 1.3b.

Core ($\alpha = 0$):

$$V^2 \propto \frac{M}{R} \propto \frac{R^3\rho_0}{R} \propto R^2\rho_0, \tag{1.2a}$$

$$\Rightarrow V \propto \sqrt{\rho_0}R, \tag{1.2b}$$

Cusp ($\alpha = -1$):

$$V^2 \propto \frac{M}{R} \propto \frac{R^2\rho_0}{R} \propto R\rho_0 \tag{1.3a}$$

$$\Rightarrow V \propto \sqrt{\rho_0 R}. \tag{1.3b}$$

This key difference of $V \propto R$ for a core and $V \propto \sqrt{R}$ for a cusp is investigated using the rotation curves produced in GalAPAGOS for the CO gas distribution in the inner region of a highly resolved early-type galaxy (NGC 3665) (see Section 5.3 and Sections 6.3).

1.5 Global Minimization Techniques

Before introducing the GalAPAGOS and Ferret software, we must first introduce the problem that Ferret was designed to solve, which is that of global minimization. Global

minimization is the principle of finding the optimal solution or set of solutions within the entire parameter space and subject to one or more objectives and all applicable constraints involved in the problem to be solved. A typical application would be curve fitting or data modelling, and attempting to minimize the χ^2 function that determines the deviation from the perfect fit. If the problem is simple, such as fitting a straight line through a number of data points, then the procedure is simple and any number of local optimization techniques can be applied. However, if the problem is complicated and involves a large number of parameters along with noise in the data, or has a number of local minima in the parameter space, then the simple techniques of local optimization usually fail at finding the global minimum in the fitness function. A fitness function evaluates how close any given intermediate solution is to the optimal solution of the problem. In the case of GalAPAGOS, we use the fitness function defined in Eq. 2.29 in Section 2.5. The user must then resort to more sophisticated global optimization techniques.

There exist a large number of computational techniques for tackling the daunting problem of global fitting of parametric models. Among the most common are deterministic methods, stochastic methods, and finally heuristic and metaheuristic methods. Here we focus on the evolutionary computation approach, which is a sub-class of the general heuristic approach to solving this problem, and the specific techniques used by Ferret (Section 1.6) and GalAPAGOS (Section 1.7).

The idea of evolutionary computing has been known for many years, and as early as 1948, Alan Turing proposed "genetical or evolutionary search". By 1962, Bremermann had executed optimization through evolution and recombination [Bre, 1962]. Throughout the 1960s and 1970s, there were three branches of the original basic idea implemented. They were known as *evolutionary programming* [Fogel et al., 1966], *genetic algorithms* [Jong, 1975], and *evolution strategies* [Rechenberg, 1973]. These later came together (1990s) under the common theme of evolutionary computing.

Simply put, an evolutionary algorithm (EA) is a class of techniques for finding the global best solution or set of solutions inspired by the process of natural evolution. Ferret is

an EA and is most closely related to the subclass of genetic algorithms (GA). However, it contains some features outside of the scope of a classic GA such as (among others): linkage learning, which reduces a complex multi-parameter problem to a set of smaller problems. Ferret operates in a (typically) high dimensional vector space, compared to a classic GA's binary data structure approach. Ferret uses the "EA" approach due to its ability to avoid local minima, and was designed with these kind of problems in mind.

The procedure of an GA is to take populations of individuals, and through mechanisms seen in natural evolution which exert environmental pressure such as mutation, crossover, and natural selection, find a population of optimal individuals. The first step is to generate an initial population of individuals randomly distributed throughout the parameter space, which would be the first generation. Secondly, the fitness of each individual in the first generation is measured by a given fitness function. The third step is to select a group of the best-fit individuals to keep as they are, or use as "parents" to breed new individuals, while also breeding new individuals via crossover between populations, mutations, and other evolutionarily inspired techniques. Once this second generation of individuals is generated, the fitness is once again measured and the process is repeated until the stopping criterion is met, and the optimal solution or set of solutions is found.

This iterative process is stochastic in the sense that during the selection of the best individuals, even the solutions which do not have the best fitness still have some chance of surviving. Similarly, when the individual is selected for mutation, it is possible for the selection to be random.

In general, the following components must be specified in order to achieve a successful GA [Eiben and Smith, 2015]:

- Definition of individuals;
- Fitness function;
- Population;
- Selection of individuals for survival; and

- Mutation, recombination, and crossover.

Ferret contains all of these components, as well as some other features outside the scope of a GA (autonomous auto-adaptation, zooming, etc.), which are described in Section 1.6.

1.6 Ferret

Ferret is the global optimizer at the heart of GalAPAGOS, lending GalAPAGOS its powerful toolset, described below. Ferret is a multi-objective evolutionary optimizer specializing in finding the optimal set of solutions to a given problem. In the case of GalAPAGOS, we only use a single objective, although a multi-objective implementation was tested. This implementation used moment maps (see Section 2.5) and therefore did not make full use of the information available within the data cube. Results from the multi-objective approach were in this case found to be inferior to the single-objective approach, and thus the multi-objective approach was abandoned. For a single-objective (in our case minimizing a fitness function), an optimal set of solutions consists of many single sets of parameters, each distinct from each other numerically, although equally viable due to the noise in the data (see Section 4.2.2). A single set of parameters would consist of one value for each of the parameters (see Section 1.7.2, Table 2 for a full list of the parameters used) searched for with Ferret. We refer to these many single sets of parameters as a "family of solutions". Ferret is integrated in a package, called Qubist, containing its own visualization tools along with the capabilities for parameter searching, global optimization, and data modelling.

Some of the features of Ferret include:

- Multi-objective search and parameter space mapping,
- Mapping a family of solutions in parameter space,
- Built in parallelization,
- Strategy auto-adaptation,

- Pausing, stopping, and resuming runs, and
- Integrated visualization.

Ferret includes a sophisticated built-in niching mechanism to help distribute solutions approximately evenly throughout the optimal region. In other words, this niching mechanism has the effect of mapping the entire optimal region, which then produces the family of solutions. The user can set a range of fitnesses (see Section 1.7) for which they would still consider a solution acceptable. For example, if the user wishes to find all solutions within a χ^2_ν (see Section 2.5) of 1 of the lowest fitness solution, Ferret would then try to map the "family" of solutions within the fitness range of $\chi^2_\nu = \left[\chi^2_{\nu,min}, \chi^2_{\nu,min} + 1\right]$.

Built in parallelization refers to Ferret's ability to use multiple computer cores simultaneously, without having to purchase MATLAB's parallel computing toolbox or the use of software outside of Ferret. Strategy auto-adaptation is Ferret's ability to automatically modify the mutation and crossover parameters, as well as various other internal parameters to Ferret. Pausing, stopping, and resuming runs is possible due to Ferret's production of detailed "History" files every few generations, so that no information is lost if a run is suspended by the user, and minimal information is lost if MATLAB or the computer crashes. Since the runs typically consist of four populations with two hundred and fifty individuals in each population, running for hundreds of generations, and possibly taking a number of days, the ability to mitigate the loss of data in the event of MATLAB, or computer power failure is critical. Integrated visualization allows the user to visualize the run's progress while it is ongoing, providing real time information on the number of generations completed, the fitness of the models produced, and the distribution of individual parameters within the parameter space.

1.7 GalAPAGOS

GalAPAGOS is a separately developed program that was written to take advantage of Qubist's global minimization techniques, and harness Ferret's powerful capabilities (Sec-

tion 1.6). GalAPAGOS in essence supplies the problem for Ferret (and if chosen, other Qubist components) to solve. GalAPAGOS contains all the information required for a Ferret search to be completed, such as, the parameters required, all equations necessary to build a galaxy model using the provided parameters (Section 2), the fitness function (Section 2.5), and all of the input data (Section 3) to be modelled.

Ferret and GalAPAGOS are both written in MATLAB (along with some C and Java code), which stores its code in .m files. There are many .m files from which GalAPAGOS is built, however they can be separated into four categories: pre-initialization, initialization, galaxy modelling, and visualization. The order in which these categories of files are used by GalAPAGOS, and the manner in which GalAPAGOS interacts with Ferret is shown in Fig. 5.

The models generated by GalAPAGOS are built on a 3D grid, the size of which is determined in the init.m file (see Section 1.7.1), with the brightness temperature calculated in each grid point using the equations outlined in Section 2 and then compared to the input observational data available for that galaxy via a fitness function (Eq. 2.29), as described in Section 2.5. The brightness temperature T_b is the temperature of a blackbody that would emit the same intensity as is measured from the astronomical object.

1.7.1 Pre-initialization Files

These files are used to convert the data into a format readable by MATLAB. Astronomical data such as those used in this project are typically stored in a Flexible Image Transport System (FITS) format, which conveniently also stores information about the observations and reductions performed on the data in a header file [Wells et al., 1981]. This conversion is done using the ConvertCube routine within GalAPAGOS. ConvertCube takes an input FITS file and converts it to a MATLAB .mat file format, while also allowing the user to apply a mask, which is used by the "sparse" version (Section 1.7.5) of GalAPAGOS.

The mask uses a variety of parameters and techniques (see Table 1) to determine the regions of the input data cube with signal, and the regions of the cube that only contain

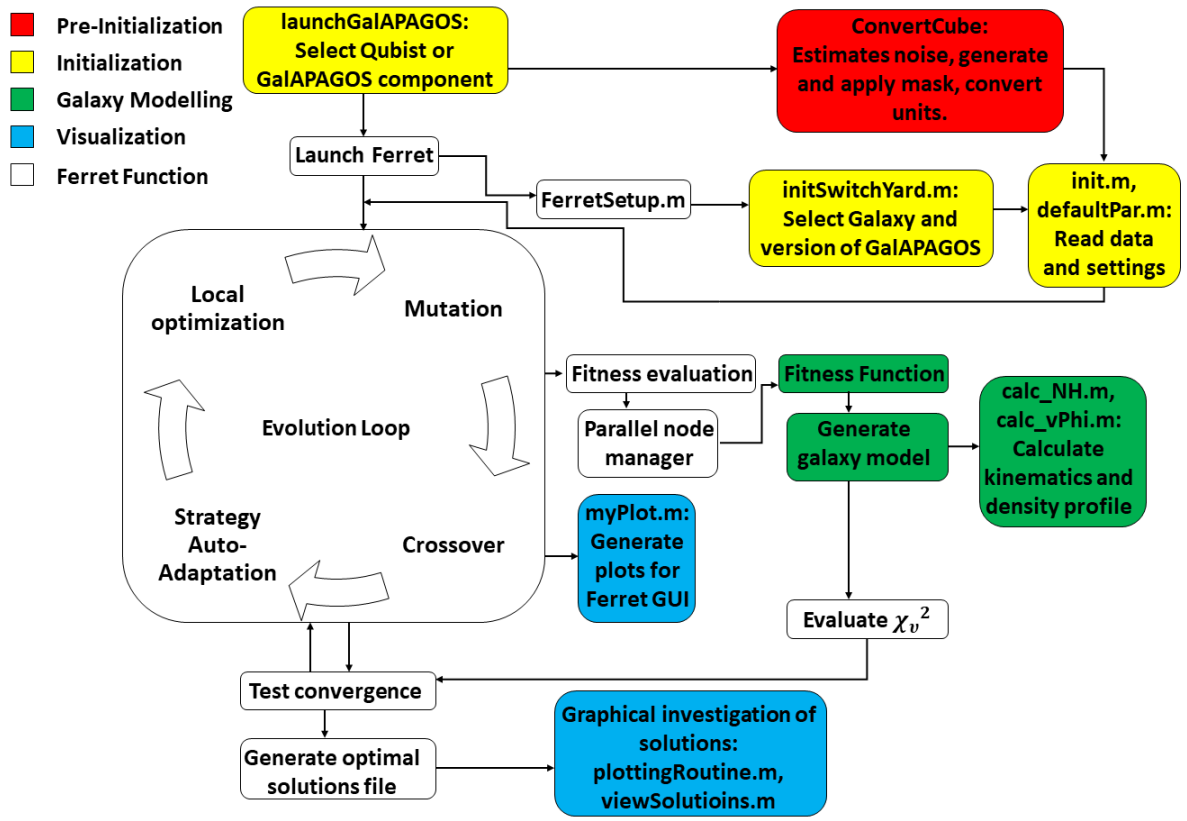

Figure 5: A flow chart for GalAPAGOS, outlining the order in which the various subroutines are called, based on [Wiegert, 2011b]. The first step is to run LaunchGalAPAGOS.m and the program is finished when the optimal solutions file has been produced after a specified number of generations. Once this is done analysis can be performed on the optimal solution set, which may include the use of some components of GalAPAGOS such as plotting routines, or analyzing the history of the run for more information on the family of models generated.

background noise. The selection of these parameters is done via a visualization tool that allows the user to see the effects of their mask on the moment maps and in each channel of the data cube (see Section 2.5). Once satisfied with their selection, the mask is applied. Additionally, the regions with data are converted from intensity units (Jansky/beam) to brightness temperature units (Kelvin) in the .mat file generated by ConvertCube. The empty regions containing only noise are set to "not a number" (NaN), so that GalAPAGOS will not use the NaN regions to determine the fitness of the model. The application of a mask also reduces the influence of the noise on the χ^2_ν, allowing the code to focus on regions containing galaxy data, rather than empty noise filled regions, resulting in a more accurate measurement of the fitness of the model to the data.

Parameter	Description
S/N edge threshold	Sets the lower limit on the desired signal to noise value, used to detect regions in the cube with signal.
voxel search radius	Sets the radius for the number of voxels searched relative to a "bright" voxel.
minimum neighbour fraction	Sets the minimum fraction for the number of nearest neighbours searched relative to a "bright" pixel.
mask buffer radius	Sets the minimum radius for the number of pixels not to be masked after a "bright" pixel is found in each velocity channel.
mask velocity buffer	Sets the minimum number of velocity channels in which a pixel is not masked after a "bright" pixel is found.

Table 1: A table of the parameters used by ConvertCube to generate a mask for the input data. A "bright" pixel is one which has a brightness temperature well above the mean value of the noise in the data.

Also done at this time is a measurement of the length of the major axis of the mask, which is then halved, and adopted as the value of the parameter measuring the outer radius of the galaxy, r_{Out}. Although previous versions of ConvertCube contained binning functionality, binning can be more conveniently accomplished using a common astronomy program (such as MIRIAD [ASP, 1995b]), to bin the data before inputting the data into ConvertCube.

ConvertCube takes the brightness temperature for each voxel and stores it within the .mat file. Once converted, the galaxy file is ready to be used for any branch of GalAPAGOS (see Section 1.7.5), with the differences between versions being outlined later in Section 1.7.5.

1.7.2 Initialization Files

Fig. 5 in Section 1.7 outlines the flow of tasks in the GalAPAGOS code. Later in Section 1.7.5, the various code branches developed in this project are outlined. The aim of this section is to introduce and define the large number of parameters used by GalAPAGOS to generate the model galaxies.

Before GalAPAGOS can be run to generate model(s), there are first a number of files that are edited to suit the characteristics of a given galaxy. For example, the user sets

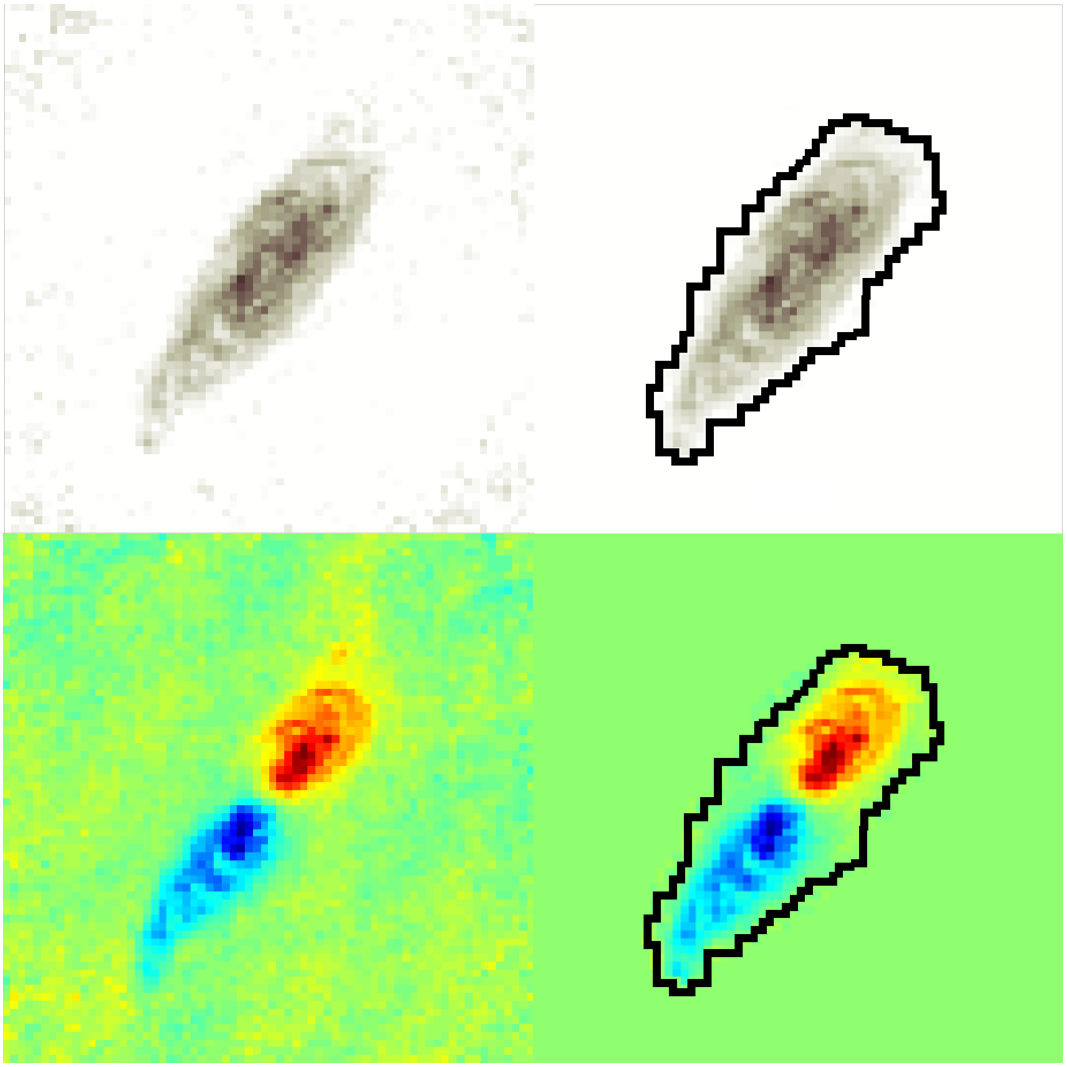

Figure 6: An example of the mask being applied to a galaxy in convertCube. The left image shows the moment 0 (top) and moment 1 (bottom) maps (see Section 2.5) of the galaxy (NGC 3198) before the mask is applied, and the right image shows the moment 0 (top) and moment 1 (top) maps of the galaxy after the mask is applied. The black outline surrounding the galaxy in the right-side images represents the mask edges.

the observational information available about the target galaxy, such as its distance, size, and the resolution of the data. Additionally, the expected values of the galaxy's kinematic parameters can be stored in the initialization files. There are between nineteen and twenty-six parameters used by GalAPAGOS to create a model of the gas in radio observations of a galaxy, depending on which code branch is used (see Section 1.7.5). Listed in Table 2 are the search parameters. These are described in more detail in Section 2 except for xShift, yShift, v_σ, v_{cm}, and TScale, which are described in Table 2. The most commonly run code branch of GalAPAGOS for HI data, which is with six SDM

Parameter	Description [unit]
r_{Out}	Outer radius of the galaxy, derived from the mask aperture[$arcsec$]
v_0	Asymptotic velocity amplitude for $a_v = 0$ [m/s]
a_v	Outer slope of the rotation curve [$unitless$]
$N_{H,0}$	Column density [$\#ofparticles/m^{-2}$]
T_s	Hydrogen spin temperature [$Kelvin$]
r_{0v}	Scaling factor to control the position of the turnover radius [$arcsec$]
H	Scale height of the galaxy [$arcsec$]
v_σ	1-D velocity dispersion [m/s]
v_{cm}	Systemic velocity of the galaxy[m/s]
dr_{Out}	Derived width of the outer fall of the surface density profile [$arcsec$]
inc	Inclination of the galaxy [Rad]
PA	Position angle of the galaxy [Rad]
$xShift$	Shifts the model galaxy's center to align the data and model [$arcsec$]
$yShift$	Shifts the galaxy's center to align the data and model[$arcsec$]
$TScale$	Scaling parameter used for dimensionless T_b [$unitless$]
$iWarp0$	Maximum (m=0) warp inclination [$radians$]
$phiWarp0$	Maximum (m=0) warp phase [$radians$]
$iWarp1$	Maximum (m=1) warp inclination [$radians$]
$phiWarp1$	Maximum (m=1) warp phase [$radians$]
$MaxTwistWarp$	Maximum warp twist at r_{Out} [$radians$]
SDM	A vector of a user chosen number of values ranging from -1 to 1, corresponding to the Surface Density Modulation values. [$unitless$]

Table 2: A table of the modelling parameters used by GalAPAGOS.

parameters and no TScale parameter, has twenty-six values that are used to generate the model galaxy.

GalAPAGOS explores the entire parameter space created by these variables using Ferret's advanced global optimization methods (Section 1.6) and finds a family of best-fit solutions using Eq. 2.29. However, for CO data, we use the optically thin (see Section 2.4) equations, meaning that we must include an additional scaling parameter $TScale$. Another consequence of these equations is that the spin temperature T_s disappears, and the intensity becomes proportional to the column density, $N_{H,0}$. The spin temperature is the temperature that would produce the observed ratio of parallel to antiparallel spins

if the HI gas were in thermal equilibrium [Abragam and Proctor, 1958]. It is defined mathematically by the Boltzmann distribution, $P_{\uparrow\uparrow}/P_{\uparrow\downarrow} = e^{-\left(E_{\uparrow\uparrow}-E_{\uparrow\downarrow}\right)/kT_s}$. Here $E_{\uparrow\uparrow}$ and $E_{\uparrow\downarrow}$ are the energies for the spin aligned and anti-aligned states respectively, and $P_{\uparrow\uparrow}$ and $P_{\uparrow\downarrow}$ are the probabilities that these states are occupied. The ratio of probabilities is also equal to the ratio of the number of atoms in each of these states. When using *TScale* to scale the intensity in the optically thin limit, there is a degeneracy between the column density and the scaling parameter. We can either combine these two into a new parameter, or fix one parameter and allow the other to vary. For convenience, we choose to fix the column density to a reasonable value for an average spiral galaxy, of $N_{H.0} = 3.0 \pm 0.8\, M_\odot\, \mathrm{pc}^{-2}$ [Martinsson et al., 2015].

A "model" is computed from a singular set of the twenty-six parameters, each with a value that is within the range we set in the initialization files. Initially, GalAPAGOS generates a number of populations of individual models. Through testing, it was found that consistent successful results could be achieved using four populations of two hundred and fifty individuals. The number of populations, number of individuals in those populations, maximum number of generations, as well as the ranges on each individual parameter are set in the FerretSetup.m file. The acceptable fitness range is also set in FerretSetup.m, that is $\chi^2_\nu = \left[\chi^2_{\nu,min}, \chi^2_{\nu,min} + X\right]$, where here X would represent the maximum deviation from the minimum χ^2_ν in the family of solutions. The expected values for each parameter, which can be found via a literature search on the galaxy and taking reasonable estimates for the non-physical (computational) parameters ($xShift$, $yShift$, $TScale$, $iWarp0$, $phiWarp0$, $iWarp1$, $phiWarp1$, $MaxTwistWarp$, and SDM parameters), as well as the input galaxy's .mat data file, are stored in the defaultPar.m file. Another initialization file is initSwitchYard, in which the user chooses their desired code branch of GalAPAGOS (see Section 1.7.5).

1.7.3 Galaxy Modelling Files

There are three main files used to calculate the brightness temperature at each individual grid point. The mathematics behind the equations is outlined in Sections 2.1, 2.2, 2.3, and 2.4. Firstly, the model galaxy is rotated to be at the correct orientation, according to its inclination, position angle, and the various twists and warp parameters (see Section 2.3) associated with the model. The position angle is the angle of the galaxy's major axis measured counter clockwise from the north celestial pole. After this follows the calculation of the kinematics using Eq. 2.2, which occurs in calc_vPhi.m. Lastly, the density profile is calculated in the calc_NH.m code, using Eq. 2.6.

Once the model galaxy is correctly oriented in the 3D grid and it has the velocity distribution and density profiles of the model, the brightness temperature at each grid point may be assessed. This calculation is described in Section 2.4. Once the brightness temperature for each grid point is found, the model galaxy fitness (χ^2_ν) is ready to be measured via the fitness function (see Section 2.5).

1.7.4 Visualization Files

Due to the unique capability of GalAPAGOS to generate a family of solutions (courtesy of Ferret), the ability to simultaneously display solutions for analysis purposes was required. This was achieved in the visualization code known as plottingRoutine.m. This tool allows the user to plot multiple rotation curves and density profiles simultaneously, while also allowing the user to choose the fitness range to display, choose whether to display only solutions with positive a_v (outer slope), and a large or small r_{0v} (turnover radius scaling parameter). This plotting routine also allows the user to display the rotation curves and density profiles of artificial galaxies. Finally, this routine also allows the user to export the galaxy model, initially contained in a .mat file, and export it to a FITS file, which is required for further analysis.

plottingRoutine.m was originally written by a MITACS summer intern, Ayan Acharyya;

however, it needed major revisions when the array structure used by Ferret was updated at the beginning of this project. The ability to export FITS files was also not originally included in this tool, and was added early on in this project.

The second visualization tool, known as viewSolutions.m, also allows the user to display rotation curves and density profiles, however only of a single model at a time. The primary difference is that viewSolutions.m allows the user to display moment 0 map (integrated intensity map) and moment 1 map (map of the velocity field) maps (see Section 2.5), in addition to the ability to step through the cube (see Section 3), while plottingRoutine.m does not. These moment 0 and 1 maps, as well as the individual channels of the galaxy model cube can be overlaid with contours representing the data, in order to examine the morphology differences between the model galaxy and the data. This is efficacious for rough assessments of the progression of the modelling run. However, due to the limited nature of these displays, viewSolutions.m also allows the user to export an individual galaxy model as a FITS file, which can then be used in other standard astronomy programs, such as KARMA [ASP, 1995a], for further analysis.

Finally, there is the myPlot.m routine, which is used during the run to generate a moment 0 map of the data, overlaid with contours of the moment 0 map of the lowest fitness model galaxy, to examine the differences in their morphologies as a method to ensure the run is going well. This is embedded in the Qubist "dashboard" (shown in Fig. 7), consisting of four plots indicative of the quality of the run. These plots also contain a display of the evolution statistics, which shows the number of optimal individuals in each population, as well as the overall minimum fitness, the optimal fitness bounds, which is simply a display of the bounds on the range of fitnesses searched as a function of the generation number, and finally a two dimensional scatter plot of the distribution of parameters within the populations, in which the user can choose which parameters they would like to view the distributions of.

1.7.5 Branches of the Code

The code can be run in several configurations, depending on the goals of the run. There is a non-sparse code branch, in which no mask is applied to the input galaxy data, as well as a sparse code branch in which one can mask out the background in order to have more efficient and accurate modelling by only using voxels with signal to build the galaxy model. Currently, the non-sparse code branch is only used for debugging, since the code itself in the non-sparse version is less complicated. However, since there is no mask applied, the non-sparse code branch is significantly (50%) slower. Within each of these, there is also the option to use Java code in order to reduce the run time for each of the previous options. Finally, there is a choice between using the non-optically thin equations or optically thin dimensionless equations (see Section 2.4). A visualization of the code branch selection process is given in Fig. 8. Unfortunately, not all changes to the code are propagated automatically through all branches. A future goal is to merge together all branches to increase simplicity in code maintenance and updating, as well as increase convenience for the user.

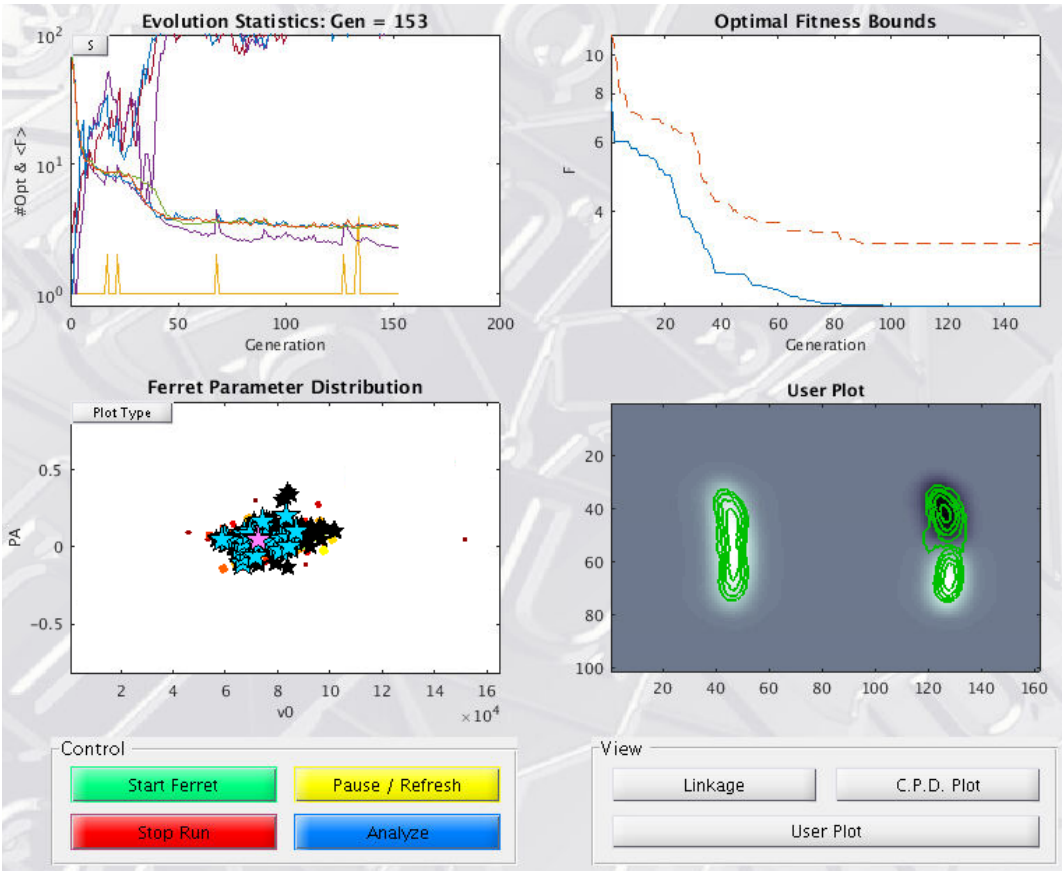

Figure 7: The Qubist dashboard after running a model in GalAPAGOS for 153 generations. In the upper left plot, we see the evolution statistics, displaying the number of optimal individuals (see Section 1.5) in each population (line starting at 0 and increasing), as well as the lowest χ^2_ν for each population (line starting in upper left corner of plot and decreasing). In the upper right plot, we see the optimal fitness bounds, showing the range of fitnesses searched as a function of the generation number. In the lower left plot, we see a 2D scatter plot of the distribution of parameters within the populations. Any two parameters can be selected. In the bottom right plot is the user defined plot, which in the case of GalAPAGOS displays contours of the input data's moment 0 map (left) and moment 1 map (right), overlaid on the best fit model's moment 0 map (left) and moment 1 map (right). See Section 2.5 for further explanation of moment maps.

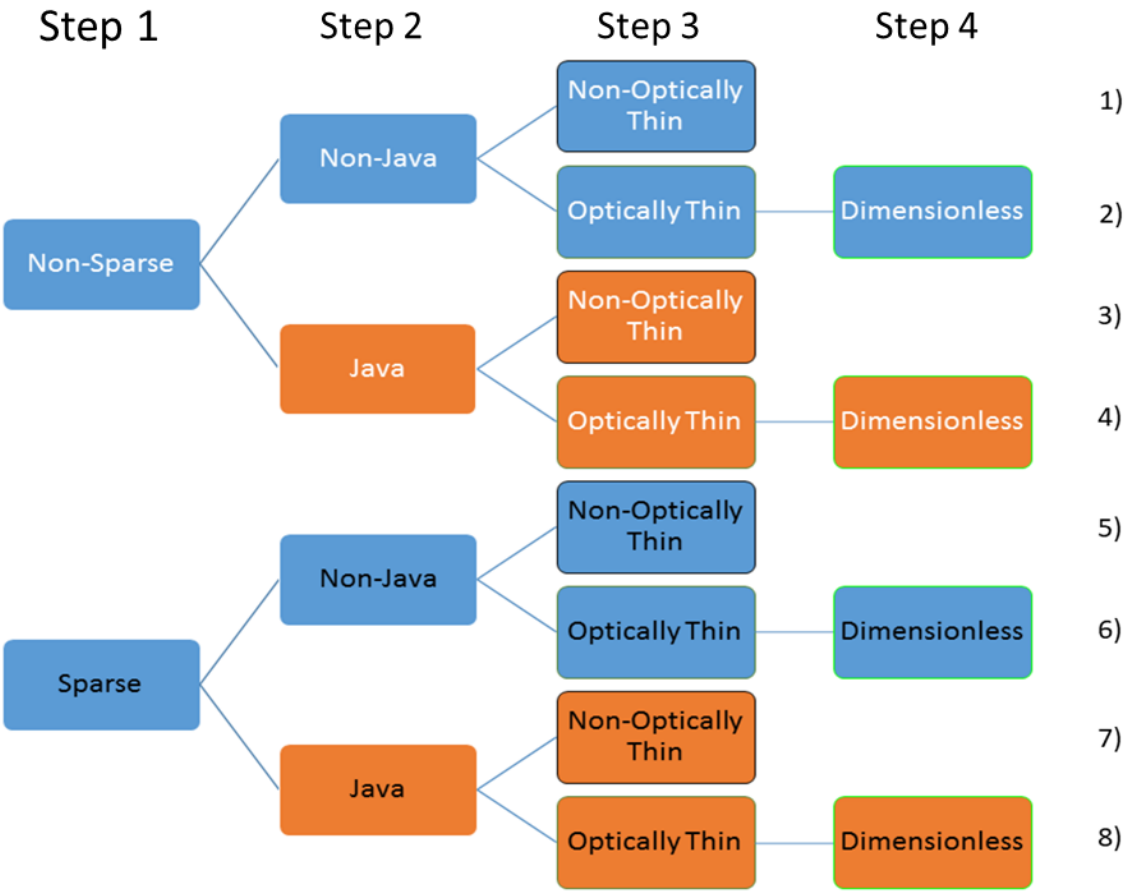

Figure 8: A tree diagram of the different branches of GalAPAGOS, and the steps taken to select between them. Step 1 is to select between non-sparse and sparse. Step 2 is to select between Java and Non-Java. Step 3 is to select between non-optically thin or optically thin and dimensionless (see Section 2.4).

2 Parametric Modelling

"*The secret of life is honesty and fair dealing. If you can fake that, you've got it made.*"

— Groucho Marx

The goal of GalAPAGOS is to generate a parametric model of a rotating galaxy that fits to observed gas data cubes in order to produce rotation curves, density profiles, and a model data cube. These model data cubes can then be used for further analysis. The theory associated with the parametric modelling is described below, along with how the parameters are associated with various galaxy characteristics relevant to galaxy evolution. Section 1.7.2 summarizes and defines the various modelling parameters, and a table summarizing the parameters is presented in Table 2.

2.1 Rotation Curves

A rotation curve is simply the distribution of the radial velocity of a galaxy as a function of the distance from the galaxy's center. Unlike position-velocity diagrams, the rotation curve is corrected for the inclination of the galaxy to the observer's line of sight. Rotation curves are a crucial component when producing DM models of galaxies, and allow us to calculate the total dynamical mass of a galaxy.

Early in the 20^{th} century galaxies were believed to have a Keplerian behaviour [Einasto, 2010]. The inner part of the galaxy would rotate as a solid disk with the radial velocity increasing, then outside of this core with solid body rotation the velocity would decrease with radius. Rotation is described mathematically by setting the gravitational acceleration per unit mass equal to the central acceleration, resulting in velocity as a function of galactocentric radius R and mass M

$$F_{Inertia} = F_{Gravity} \Rightarrow \frac{mV(R)^2}{R} = G\frac{mM(R)}{R^2} \tag{2.1a}$$

$$\Rightarrow V(R)^2 = \frac{GM(R)}{R}. \tag{2.1b}$$

Looking at the photometry of galaxies, it appears that most of the mass resides with the dense distribution of stars at the center of a galaxy. This would lead to a rotation curve that outside of the solid body like core behaviour, would decrease in velocity as the radius increased. However, in the early 1920's [Jeans, 1922], it was discovered that in order for galaxies to behave as they do, there must be much more mass than that which can accounted for by examining the visible light from the galaxy. The signature is that the rotation curves flatten, rather than decrease, after the inner rise. This discrepancy is now accounted for with DM models (see Section 1.2).

The kinematic behaviour of galaxies is currently described by galaxies being composed of a sum of three mass components along with a (typically spherical) DM halo surrounding the galaxy. The total dynamical mass in a galaxy is calculated using Eq. 2.1b with $V(R)$ being equal to the measured velocity at the furthest radius for which there is still data available. We can decompose the rotation curve into its component pieces using a technique called mass decomposition, as is shown in Fig. 9.

In the GalAPAGOS code, the equation used to model the total dynamical mass rotation curves (v_t in Fig. 9) was proposed by Dr. Jason Fiege, and is as follows:

$$v_\phi(r) = v_0 \tanh\left(\frac{r}{r_{0v}}\right)\left[1 + a_v \frac{r}{r_{Out}}\right], \tag{2.2}$$

$v_\phi(r)$ is the azimuthal rotational velocity, v_0 is the velocity amplitude of the rotation curve at infinity when a_v is zero (see Fig. 10). The parameter r_{0v} is a scaling factor that controls the position of an apparent knee in the curve, sometimes referred to as the turnover radius. The parameter a_v controls the outer slope; with $a_v = 0$ being a flat rotation curve, $a_v < 0$ being declining, and $a_v > 0$ being rising.

Initially r_{Out} was a derived outer radius, where the disk column density was assumed to drop to zero. However, the data in the outer regions have noise at a level similar to the intensities of the data, leading to r_{Out} being poorly constrained. Additionally, the gas in the outer region may change from neutral to an ionized state, in which case the density would not drop to zero. Therefore, we fixed r_{Out} by using half of the diameter

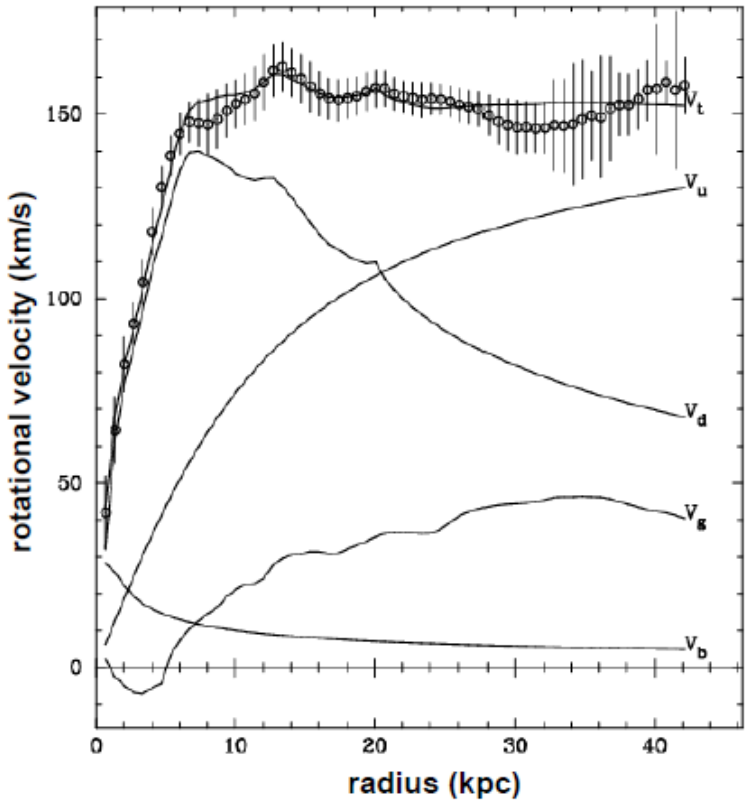

Figure 9: From T. Wiegert, 2010, P.13. "A maximum disk model of NGC 3198, with a tilted ring rotation curve measured from HI data from the THINGS survey. v_b is the bulge contribution to the rotation curve, v_g is the gas contribution (HI and He), v_d is the stellar disk contribution, v_u is the user defined halo model (here an isothermal sphere), and v_t is the total velocity."

of the major axis of the mask generated in ConvertCube (see Section 1.7.1). The mask is designed to encircle the entire galaxy, which allows r_{Out} to be at least as large as the semi-major axis of the galaxy. Note that there is no loss of generality in Eq. 2.2, since r_{Out} only enters as a_v/r_{Out}. This quantity can still take on any value by varying a_v.

Looking at Fig. 9, it is clear that the inner slope (when $r < 10$kpc in this case) is fairly well-constrained. However, if the data has less three beams across the rise of the rotation curve, then the inner slope is not well-constrained. HI data typically has less than three beams (resolution elements) across the radius of the galaxy. CO data coming from the ALMA and CARMA surveys have a much higher resolution and allow the inner slope of galactic rotation curves to be substantially constrained compared to what was attainable using HI data. Using a custom plotting routine (see Section 1.7.4), we are able to plot a number of rotation curves using equation 2.2 from the various models outputted via

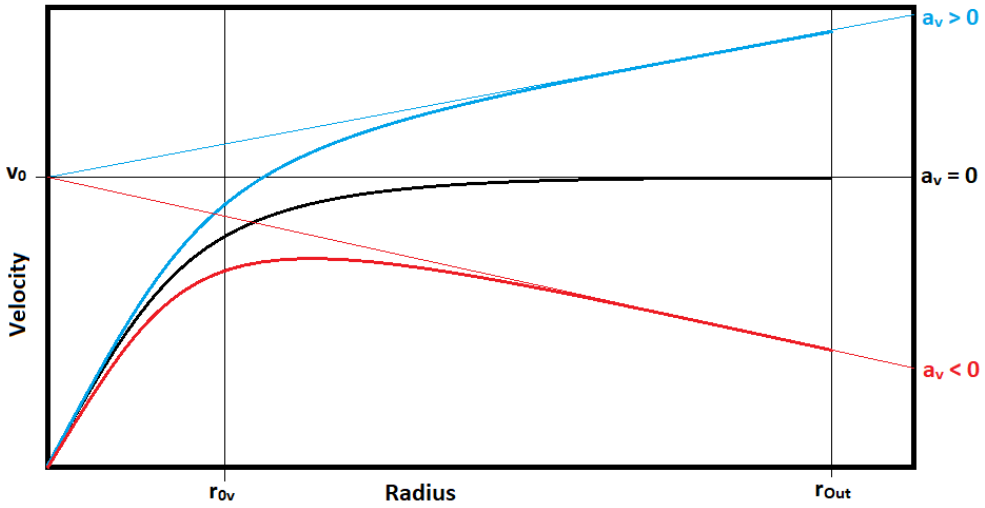

Figure 10: A representation of Eq. 2.2 with three different a_v. For $a_v \neq 0$ we can see how to find the velocity amplitude v_0, note that v_0 is not the measured velocity amplitude used to determine the dynamical mass. Also shown is that the scaling parameter r_{0v} is not exactly representative of the location of where the curve turns over. The r_{0v} and a_v parameters do not measure a physical quantity, rather they adjust the fit of the curve.

GalAPAGOS on the same plot, and examine their similarities along with their differences, as can be seen in Fig. 11.

2.2 Density Profiles

Our density profile is a plot of the column density of a galaxy as a function of its radius. A typical HI disk tends to have a fairly constant surface density distribution throughout most of the disk, with the exception of a dip in the center region where the density is lower than the surrounding disk. GalAPAGOS originally modelled the density distribution as a sigmoid function that fades at the outer radius (r_{out}) of the galaxy. A sigmoid function is a mathematical function having a characteristic "S" shaped curve, such as the error function. A secondary Surface Density Modulation (SDM) term was included to account for density profiles that are not flat throughout the disk region, and allow the density profile to rise and descend throughout the disk region, which is a more accurate portrayal of a typical galaxy. This density profile can be described mathematically as

$$N_H(r) = \frac{N_{H,0}}{2}\left[tanh\left(\frac{r_{out} - r}{dr_{out}}\right) + 1\right] \cdot SDM(r; \boldsymbol{a_i}), \tag{2.3}$$

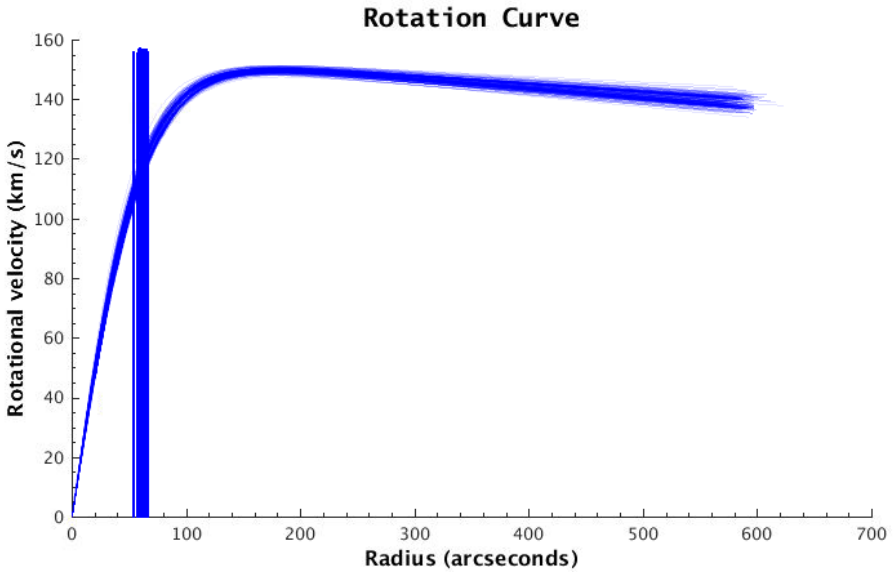

Figure 11: An example of the custom plotting routine's functionality for plotting multiple rotation curves. Here the dark blue vertical lines are positioned at r_{0V} and their heights correspond to v_0, which is the asymptotic velocity amplitude if the outer slope $\alpha = 0$.

where $N_{H,0}$ is the column density of the galaxy, and dr_{out} is a scaling factor that controls how quickly the density drops to zero (see Fig. 12). The SDMs are included by means of a numerically interpolated spline function $SDM\,(r; \boldsymbol{a_i})$ in Eq. 2.3, where $\boldsymbol{a_i} = \{a_1, a_2, \ldots, a_n\}$ is a vector representing the change in surface density above or below the primary structure at n equally spaced points between zero and $r_{out} \times 1.25$. Each a_i is set independently and range from -1 to 1, and $SDM\,(r)$ is determined by:

$$SDM(r) = \max\{0, 1 + S(r, \boldsymbol{a_i})\} \tag{2.4}$$

S is a numerically computed cubic spline curve, passing through $\{a_1, \ldots, a_n\}$, as shown in Fig. 12. Note that in the case that the spline is negative, the surface density is automatically set to zero.

We can then obtain the volume density by multiplying the surface density $N_H\,(r)$ by a normalized Gaussian function

$$n_H\,(r, z) = \frac{N_H\,(r)}{\sqrt{2\pi H^2}} \exp\left(-\frac{z^2}{2H^2}\right), \tag{2.5}$$

where H is the scale height of the disk, assuming the vertical profile away from the

midplane is fit by a Gaussian. The scale height is the vertical distance over which the density and pressure fall by a factor of 1/e

It was found during this project that the derived outer radius r_{Out} and the scaling factor dr_{out} were poorly constrained, and thus Eq. 2.3 was modified such that these parameters are no longer required. The current implementation is solely an interpolated spline function, scaled by the column density $N_{H,0}$:

$$N_H(r) = N_{H,0} \cdot SDM(r; \boldsymbol{a_i}). \tag{2.6}$$

The models presented in Section 5 all use this new formulation for the density profile.

This equation is capable of reproducing all of the typical features we expect to see, such as those seen in Fig. 12, since the SDMs are an interpolated spline function as described above.

We also normalize the SDMs such that the average SDM is zero. The $N_{H,0}$ parameter becomes associated with the average column density of the galaxy after this normalization is done. Mathematically, this condition can be written as

$$0 = \frac{\int SDM \cdot 2\pi r dr}{\pi R^2}. \tag{2.7}$$

2.3 Twists and Warps

HI disks in galaxies are well known to exhibit warps, which is the motivation behind the commonplace tilted ring models [Rogstad et al., 1974]. To create twists and warps in the galaxy, we use angles within the disk plane, $\phi_{warp,m}$, and angles out of the disk plane, $i_{warp,m}$, where m denotes the azimuthal wave number, which will be defined later in this section. Additionally, we require the full radius R'_{Cyl} of cylindrical, and R'_{Sphere} of spherical coordinate systems, since we rotate the model galaxy in and out of plane.

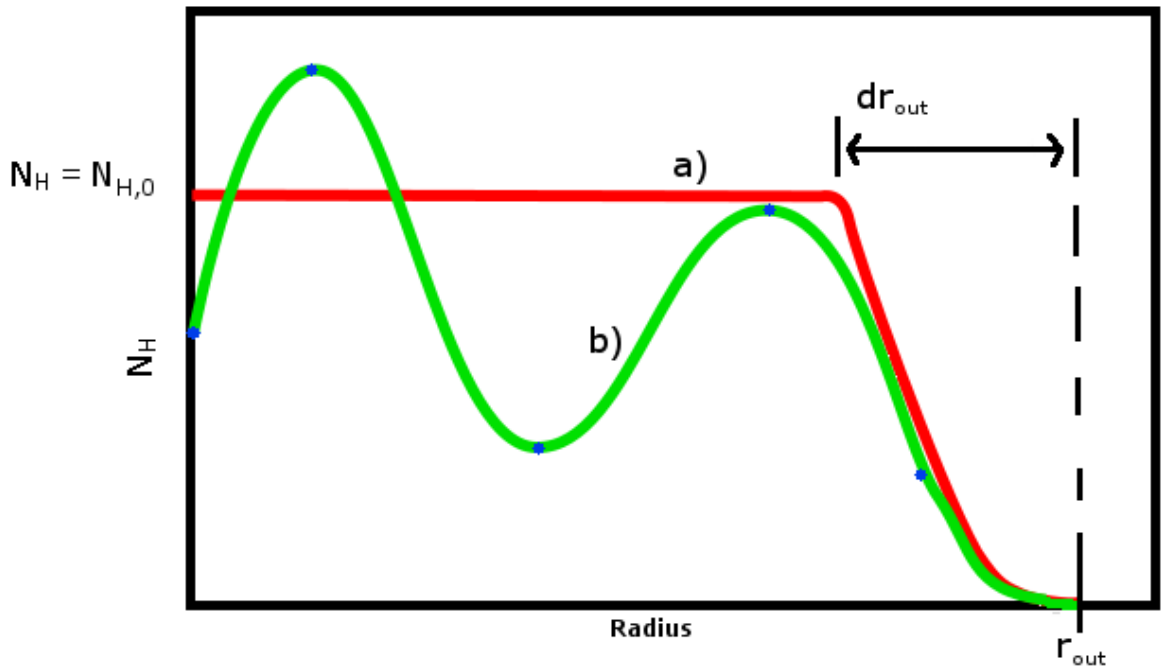

Figure 12: An example of the original (Eq. 2.3) surface density profile. This shows (a) the basic sigmoid function which provides the flat region throughout the disk along with the drop to zero before the radius is greater than r_{out}. And (b) the surface density profile after it has been modified by a spline function, described in Eq. 2.3. The SDM coefficients a_i are also indicated on the curve. Based on Wiegert [2011a].

The classical tilted ring model divides the disk into a set number of rings and treats the warp on each ring independently. This is not the approach used in GalAPAGOS, where there are no explicit rings, but rather smoothly varying tilt angles (ϕ, i), which are functions of radius and angle within the disk. The primary difference between the GalAPAGOS model and tilted ring models is that if one thinks of our model as a tilted ring model, then all the rings are linked together with their orientation varying smoothly from the inner galaxy to the outer edge.

This warp is achieved through a series of rotation matrices. First, the model galaxy is rotated in the sky plane to match the position angle and inclination angle found by

GalAPAGOS using

$$\begin{pmatrix} x' \\ y' \\ z' \end{pmatrix} = \begin{pmatrix} 1 & 0 & 0 \\ 0 & \cos(inc) & \sin(inc) \\ 0 & -\sin(inc) & \cos(inc) \end{pmatrix} \begin{pmatrix} \cos(PA) & \sin(PA) & 0 \\ -\sin(PA) & \cos(PA) & 0 \\ 0 & 0 & 1 \end{pmatrix} \begin{pmatrix} x \\ y \\ z \end{pmatrix}. \tag{2.8}$$

In the above equation, x', y', z' represent the coordinates after the rotation matrices are applied. The "PA" parameter is the "GalAPAGOS position angle", which is defined as the angle of the galaxy's major axis measured clockwise from the south celestial pole, and is searched for by GalAPAGOS. Note that this is not typically how position angle is defined, and that this discrepancy is due to some of the rotations and manipulations internal to GalAPAGOS. The "inc" parameter is the inclination angle of the galaxy, in which a galaxy with an inclination angle of 90° would be viewed completely edge-on, and a galaxy with an inclination angle of 0° would be completely face-on.

Next, the primed coordinates are used to generate a spherical radius and a cylindrical radius, with each being used when appropriate. That is the requirement for the cylindrical radius arises when we apply the twist in the plane of the galaxy, and the need for a spherical radius comes from the warp out of the plane of the galaxy. The spherical and cylindrical radii are defined as

$$R'_{Sphere} = x'^2 + y'^2 + z'^2, \tag{2.9a}$$

$$R'_{Cyl} = x'^2 + y'^2. \tag{2.9b}$$

We can then use the spherical radius R'_{Sphere} to define the angle ϕ (Eq. 2.10a), which is the angle out of plane which the galaxy will be twisted. Note that ϕ in this context does not refer to the azimuthal angle as it did in the rotation curve equation, Eq. 2.2. Therefore if $\phi = 0$, then the tilt of the galaxy at a distance x' is in the same direction as the disk inclination. Also needed is ϕ_{twist} (Eq. 2.10b), which is the amount of twist being applied to the galaxy (in the plane of the galaxy) as a function of the cylindrical

radius, and is defined as

$$\cos(\phi) = \frac{x'}{R'_{Sphere}}, \tag{2.10a}$$

$$\phi_{twist} = maxTwistWarp \cdot \left(\frac{R'_{cyl}}{r_{out}}\right), \tag{2.10b}$$

where $maxTwistWarp$ is the maximum twist, which is applied at $R'_{cyl} = r_{Out}$. We then use R'_{cyl} along with Eq. 2.10b to apply the twist in the plane of the galaxy, by

$$\begin{pmatrix} x'' \\ y'' \\ z'' \end{pmatrix} = \begin{pmatrix} \cos(\phi_{twist}) & \sin(\phi_{twist}) & 0 \\ -\sin(\phi_{twist}) & \cos(\phi_{twist}) & 0 \\ 0 & 0 & 1 \end{pmatrix} \begin{pmatrix} x' \\ y' \\ z' \end{pmatrix}. \tag{2.11}$$

Next we apply the warp, first with $m = 1$ (Eq. 2.13b), then with $m = 0$ (Eq. 2.15b) mode. The azimuthal wave number, m, controls the shape of the warp pattern applied. If $m = 0$, then the plane of the galaxy is bent up on one side and down on the other (as shown by the blue line in Fig. 13). If $m = 1$, the plane of the galaxy is bent in a "U" shape (as shown as the red line in Fig. 13) along both the major and minor axis of the galaxy. However, one bend direction will be perpendicular to the other, similar to how the brim of a cowboy hat is bent. These two modes are applied simultaneously, with the $m = 0$ warp parameters being $i_{warp,0}$ and $\phi_{warp,0}$, and the $m = 1$ warp parameters being $i_{warp,1}$ and $\phi_{warp,1}$.

We use the spherical radius, R'_{Sphere}, along with the $i_{warp,m}$ parameters to apply the warp out of the plane of the galaxy, as presented in Eq. 2.12 - Eq. 2.15b. For the $m = 1$ mode, we have

$$inc_{warp,1} = i_{warp,1}\left(\frac{R'_{Sphere}}{r_{out}}\right)\cos(\phi), \tag{2.12}$$

where ϕ is defined in Eq. 2.10a, $i_{warp,1}$ is the $m = 1$ i_{warp} parameter, and $inc_{warp,1}$ is used to determine the total warp applied out of plane for the $m = 1$ warp mode. We then define the $m = 1$ warp mode rotation matrix, $\mathbf{A}$, in order to apply the $m = 1$ mode warp

to the galaxy as follows:

$$\mathbf{A} = \begin{pmatrix} \cos(\phi_{warp,1}) & \sin(\phi_{warp,1}) & 0 \\ -\sin(\phi_{warp,1})\cos(inc_{warp,1}) & \cos(\phi_{warp,1})\cos(inc_{warp,1}) & \sin(inc_{warp,1}) \\ \sin(\phi_{warp,1})\sin(inc_{warp,1}) & -\cos(\phi_{warp,1})\sin(inc_{warp,1}) & \cos(inc_{warp,1}), \end{pmatrix} \tag{2.13a}$$

$$\begin{pmatrix} x''' \\ y''' \\ z''' \end{pmatrix} = \mathbf{A} \cdot \begin{pmatrix} x'' \\ y'' \\ z'' \end{pmatrix}, \tag{2.13b}$$

Next we define $inc_{warp,0}$, which is used to determine the total warp applied out of plane for the $m = 0$ warp mode:

$$inc_{warp,0} = i_{warp,0} \left(\frac{R'_{Sphere}}{r_{out}} \right), \tag{2.14}$$

where ϕ is defined in Eq. 2.10a, and $i_{warp,0}$ is the $m = 0$ i_{warp} parameter. Finally, we need the $m = 0$ warp mode rotation matrix, $\mathbf{B}$, in order to apply the $m = 0$ mode warp as follows:

$$\mathbf{B} = \begin{pmatrix} \cos(\phi_{warp,0}) & \sin(\phi_{warp,0}) & 0 \\ -\sin(\phi_{warp,0})\cos(inc_{warp,0}) & \cos(\phi_{warp,0})\cos(inc_{warp,0}) & \sin(inc_{warp,0}) \\ \sin(\phi_{warp,0})\sin(inc_{warp,0}) & -\cos(\phi_{warp,0})\sin(inc_{warp,0}) & \cos(inc_{warp,0}) \end{pmatrix}, \tag{2.15a}$$

$$\begin{pmatrix} X(x,y,z) \\ Y(x,y,z) \\ Z(x,y,z) \end{pmatrix} = \mathbf{B} \cdot \begin{pmatrix} x''' \\ y''' \\ z''' \end{pmatrix}, \tag{2.15b}$$

The coordinate dependent X, Y, and Z vector fields are then used to construct the galaxy model. The density profile (Section 2.2) and kinematics (Section 2.1) are generated after the X, Y, and Z vector fields have been calculated. The density and velocity structure of the galaxy model therefore inherently take the warp into account when they are calculated.

We are able to search for which mode best fits the galaxy by applying a warp with both $m = 0$ and $m = 1$. GalAPAGOS can, in principle, find a model with either set of the warp parameters ($i_{warp,m}$, $\phi_{warp,m}$) set equal to zero, therefore indicating the other warp mode has been chosen, or some combination of both modes; e.g. if $i_{warp,0} = \phi_{warp,0} = 0$, and $i_{warp,1}$, $\phi_{warp,1} > 0$, then GalAPAGOS has found that the model galaxy with the $m = 1$ mode fits better than the model galaxy with the $m = 0$ mode. Thus, we are able to search for both modes simultaneously.

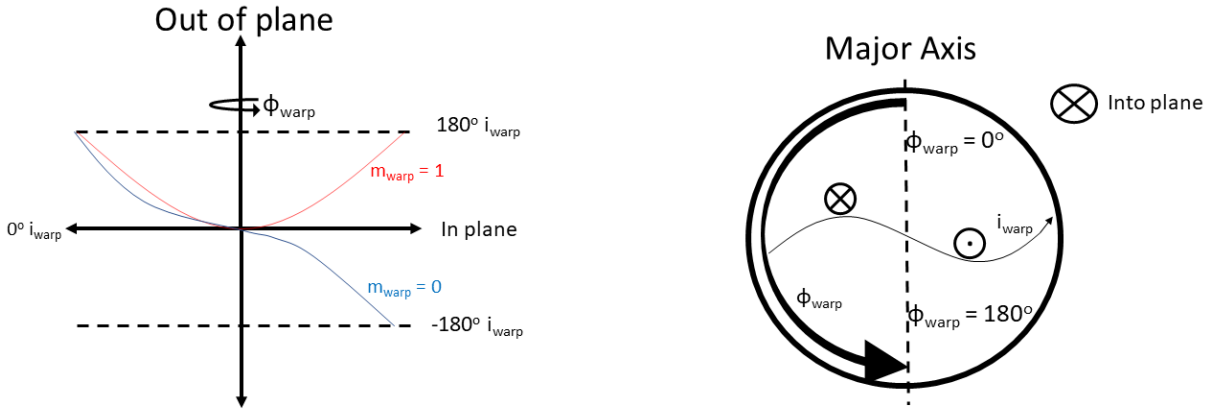

Figure 13: Warp figure. The left image represents an edge-on galaxy, with the blue line representing the $m = 0$ mode, and the red line representing the $m = 1$ mode. The right image represents a completely face-on view of a galaxy, with the $i_{warp,m}$ going into and out of the plane of the galaxy, and the $\phi_{warp,m}$ rotating the galaxy completely in the plane of the galaxy.

2.4 Radiative Transfer

Radiative transfer describes the phenomenon of energy transfer through a medium by means of electromagnetic radiation. This includes how the propagation of the radiation through the medium is affected by absorption, emission, and scattering processes. The intensity I_ν at a frequency ν is often used when discussing radiative transfer. However, due to the radio wavelengths we are working with, we will be using the brightness temperature T_b. Recall, the brightness temperature is the temperature of a blackbody that would emit the same intensity as is measured from the astronomical object. The intensity and brightness temperature are related by the Rayleigh-Jeans law (Eq. 2.17), which

approximates Planck's law (Eq. 2.16) when we have low frequencies ($h\nu << kT$) [Binney and Merrifield, 1983a]

$$I_\nu = \frac{2h\nu^3}{c^2}\frac{1}{e^{\frac{h\nu}{kT}}-1}, \tag{2.16}$$

$$T_b = \frac{c^2}{2k\nu^2}I_\nu, \tag{2.17}$$

where h is the Planck constant, c is the speed of light, and k is the Boltzmann constant. The brightness temperature T_b of a gas cloud can then be defined as (ignoring background radiation)

$$T_b = T_s\left(1-e^{-\tau_\nu}\right)[K], \tag{2.18}$$

where T_s is the spin temperature for HI, and τ_ν is the optical depth (measure of the amount of absorption that occurs when light travels through a medium) at a frequency ν. In the optically thin limit, $\tau_\nu \ll 1$, and therefore Eq. 2.18 reduces to

$$T_b \approx T_s\tau_\nu. \tag{2.19}$$

Using the definition for the optical depth

$$\tau_\nu = \frac{C}{T_s}\int \phi_v n_h dz, \tag{2.20}$$

we can write Eq. 2.19 as

$$T_b = C\int \phi_v\left(v\left(z\right)\right) n_h\left(z\right) dz, \tag{2.21}$$

where C is a constant (described below, Eq. 2.22) and ϕ_v is the line profile. The line profile defines the absorption/emission profile (assumed to be the same). We use a Gaussian function defined such that $\int \phi_v dv = 1$ and ϕ_v has units of s/m. In Eq. 2.21, n_h is the volume density profile, and has units of atoms/m^3, and dz is the infinitesimal change along the line of sight. The z dependence comes from the different velocities and column densities seen along the line of sight of the brightness temperature. For hydrogen, the

constant C can be written as

$$C = \frac{B_{12} h^2 \nu}{4} \left[\frac{m^3 K}{s} \right], \tag{2.22}$$

where B_{12} is the Einstein coefficient for photo-absorption for the J=2 to J=1 energy level transition, ν is the frequency of the light emitted by the molecule, and k_B is the Boltzmann constant. For HI, $C = 5.489 \times 10^{-20} m^3 s^{-1} K$ [Binney and Merrifield, 1983b].

For CO, we do not know this constant due to its dependence on the number densities of quantum states. In order to calculate $B_{J+1 \to J}$ for each transition, we need to calculate the number density for each energy level, which depends on contributions from each process associated with molecular transitions; primarily rotational, with additional contributions from vibrational and collisional transitions. Self-consistently solving for the level populations at high optical depth at high optical depth, in the presence of multiple scatterings, is not feasible. We therefore choose to use a scaling factor to account for this unknown constant. In the code, this scaling factor, which we call TScale, is one of the parameters that we search for, since it is not known beforehand. In practice, this scaling parameter TScale is found by making Eq. 2.21 dimensionless. This can be done by using dimensionless parameters

$$\phi_v = \phi_{v,0} \widetilde{\phi_v}, \tag{2.23a}$$

$$dz = r_0 d\tilde{z}, \tag{2.23b}$$

$$n_h = n_0 \widetilde{n_h}, \tag{2.23c}$$

$$n_0 = \frac{1}{r_0^3}, \tag{2.23d}$$

where the $\widetilde{\ }$ accent denotes a dimensionless parameter. Substituting these expressions into Eq. 2.21 leads to

$$T_b = C n_0 r_0 \phi_{v,0} \int \widetilde{\phi_v} \widetilde{n_h} \widetilde{dz}, \tag{2.24}$$

where all of the units are contained in Cn_0r_0. Rearranging Eq. 2.24 gives us

$$\widetilde{T_b} \coloneqq \frac{T_b}{Cn_0r_0\phi_{v,0}} = T_b \cdot \mathrm{TScale} = \int \widetilde{\phi_v}\widetilde{n_h}\widetilde{dz}, \tag{2.25}$$

leading to a scale factor TScale of

$$\mathrm{TScale} = \frac{1}{Cn_0r_0\phi_{v,0}}. \tag{2.26}$$

Eq. 2.18 is used in GalAPAGOS for the non-optically thin models. We implemented Eq. 2.25 to apply the simpler optically thin limit where appropriate. By construction, our model disks consist of diffuse gas, so this optically thin approximation is valid.

For molecular clouds such as those we are looking at in NGC 3665, we use Eq. 2.25. A molecular cloud is an interstellar region dense enough to self-gravitate and form molecules such as H_2 and CO, from which stars may be formed. They are the densest regions found in the interstellar medium, are highly turbulent and magnetized, and are the birth place for new stars and planets. Molecular clouds usually form on a timescale of roughly 10 million years or less, and have a large range of sizes, from 5-200 parsecs [Williams et al., 2000]. Molecular clouds are crucial to the study of stellar evolution, insterstellar medium dynamics, and galaxy evolution as a whole.

The argument for the appropriateness of the optically thin approximation in the case of molecular clouds is as follows. Firstly, instead of thinking of the gas as being optically thick or thin we think of the gas as having a "filling factor", f_v, which is equal to the total cross-sectional area of the clouds that we observe in the beam (our resolution element) over the total beam area, within a particular velocity bin, and is shown in Eq. 2.27. Therefore

$$f_v = \frac{\sum\limits_i A_i}{A_{beam}}, \tag{2.27}$$

where A_i is the area of the i^{th} cloud within the velocity channel, and A_{beam} is the total area of the beam. If we now wanted to find the average brightness temperature of the

observed cloud over a beam, we would find:

$$\langle T_b \rangle = T_s f_v, \tag{2.28}$$

where T_s is again the spin temperature. Comparing Eq. 2.28 to Eq. 2.19 shows that f_v is analagous to τ_ν for the optically thin case. Note also that the filling factor is close to unity for the optically thick case, and $f_v << 1$ for the optically thin case. However, in GalAPAGOS, we do not search explicitly for either τ_ν or f_v. Rather we derive τ_ν from Eq. 2.20, which largely depends on the density distribution. In the case of using GalAPAGOS to model CO, we still rely largely on the density distribution to find T_b (similar to the optical depth approach), and we then scale that by TScale. Although the optical depth and filling factor are typically on a similar scale numerically in the optically thin case, they are not equivalent, and thus the need for scaling arises.

It should also be noted that the increase of material through which the photon has to travel that occurs as the inclination angle increases results in the optically thin approximation no longer holding for inclinations of approximately 90° [Yang et al., 2017].

2.5 Fitness function

The fitness function is used by GalAPAGOS to determine how the fitness of the model compares the brightness temperature in each voxel of the data to the brightness temperature at each grid point of the model. Note that the model resolution is the same as the data, and that the model grid is constructed such that the number of grid points in the model is equal to the number of voxels in the input data. This function calculates the reduced χ^2_ν value by summing over the differences between the observational data, T_b^{data} at each voxel, and the artificially constructed model, T_b^{model} at each grid point (i), weighted by the noise. This means that the expected χ^2_ν for a perfect model in the presence of noise is unity, although 1 is not an absolute minimum. The quality of models becomes

poorer as the value of χ^2_ν increases. The χ^2_ν value is calculated via Eq. 2.29:

$$\chi^2_\nu = \frac{\chi^2}{DOF} = \sum_{i=1}^{N} \frac{\left(T_{b,i}^{model} - T_{b,i}^{data}\right)^2}{(N-M)\,\sigma^2\,(T_b)}, \tag{2.29}$$

where DOF is the number of degrees of freedom, $T_{b,i}$ is the brightness temperature of a voxel or grid point, N is the number of voxels or grid points to be summed over, M is the number of parameters, and $\sigma\,(T_b)$ is the root mean square (r.m.s) noise of the data cube.

The χ^2_ν statistic may not the most appropriate statistical measurement of the fitness of the model to the data. The reason for this is that when we compare the intensities of the model to the intensities of the data, we compare these intensities in every voxel (grid point) throughout the entire cube. This means that there will be regions outside of the galaxy which are simply noise, weighted equally with the regions containing significant data. One way to mitigate this effect is to apply a mask to the galaxy, such that the regions outside the galaxy with no useful data will no longer be a part of the data cube (see Section 1.7.1). Another possibility would be to modify Eq. 2.29 such that the center of the galaxy is weighted more heavily than the noise. This however was beyond the scope of this thesis, and should be further explored in the future. We also note that the method of minimizing the χ^2_ν to fit a model to data is correct [Andrae et al., 2010], although an alternative could be measuring the fitness by using a modified χ^2_ν equation.

We implemented the ability to use the zeroth and first order moment maps (described below) to calculate the fitness, rather than using each voxel in the cube. This method has the advantage of improving the signal to noise ratio, since as we sum over the cube, the noise, having both positive and negative values, tends to cancel out, while the data, having only positive values, sums with itself.

A moment map can be thought of as a projection of a data cube along an axis. For example, a data cube can be collapsed along the velocity axis to form a two-dimensional spatial map, which is accomplished using the moment analysis technique found in [Rupen, 1999]. This technique can be used to produce an integrated intensity map (zeroth moment

map), a velocity field map (first moment map), and a velocity dispersion map (second moment map). The *nth* moment of a distribution is defined as [Zombeck, 2006]

$$E(x^n) \equiv \int_{-\infty}^{+\infty} x^n f(x) dx, \tag{2.30}$$

where E represents the expectation value, and $f(x)$ is any function. The zeroth and first order moment maps, which are those used for measuring the fitness in GalAPAGOS, are then

$$M_0 = \int I dv, \tag{2.31a}$$

$$M_1 = \frac{\int vIdv}{\int Idv} = \frac{\int vIdv}{M_0}. \tag{2.31b}$$

The first moment map M_1 is the intensity-weighted velocity, which is why M_0 appears in the denominator, and can be taken as a measure for the mean velocity of the gas. The zeroth moment map is the integrated flux, and can be taken as a measure of the column density.

When using the zeroth and first order moment maps, we calculate the fitness using the following:

$$\chi^2_{\nu,0} = \sum_{i=1}^{N} \frac{\left(I_{0,i}^{model} - I_{0,i}^{data}\right)^2}{(N-M)\,\sigma^2\,(I_0)}, \tag{2.32a}$$

$$\chi^2_{\nu,1} = \sum_{i=1}^{N} \frac{\left(I_{1,i}^{model} - I_{1,i}^{data}\right)^2}{(N-M)\,\sigma^2\,(I_1)}, \tag{2.32b}$$

where here $I_{0,i}$ is the intensity of a pixel in the calculated moment 0 map, and $I_{1,i}$ is the intensity of a pixel in the calculated moment 0 map. GalAPAGOS simultaneously minimizes both $\chi^2_{\nu,0}$ and $\chi^2_{\nu,1}$. The calculations for making a model galaxy remain exactly the same, although now the fitness is only measured using pixels in the zeroth and first order moment maps, instead of measuring it for each voxel throughout the cube. The end result is still a cube, and contains all of the information that we would get from a normal run with the fitness calculated using each voxel (grid point) throughout the cube.

3 Data

"Space is big. You just won't believe how vastly, hugely, mind-bogglingly big it is. I mean, you may think it's a long way down the road to the chemist's, but that's just peanuts to space."

— Douglas Adams

In this project, we used neutral hydrogen (HI) data as well as molecular gas emission, in particular carbon monoxide (CO) gas. HI spectral line emission is generated through a change in energy state between two hyperfine levels of the 1s ground state. If the spin of the electron is parallel to that of the proton, the electron has a higher energy than when their spins are anti-parallel. When the electron transitions back to the lower energy level, a photon is emitted with a wavelength of 21 cm (1.420GHz frequency). CO produces emission primarily through rotational excitation and de-excitation [Goldsmith, 1972], however there are many transitions available for each molecule. The CO data used in this project uses the CO $J = 2 \rightarrow 1$ transition, which has a frequency of 230.5 GHz and a wavelength of 1.3 mm.

Spectral line radio data, in general, follows the same basic format, which is the data comprising a three-dimensional data cube. The x and y axes are the Right Ascension (RA) and the Declination (DEC). The z axis is frequency, which is typically converted to a heliocentric radial velocity, as is illustrated in Fig. 14. The data cube itself gives us the intensity as a function of both spatial coordinates for our object, RA and DEC, and line of sight velocity. Astronomical data is typically stored in FITS files. Although MATLAB can read FITS files, it is more convenient to convert these FITS files to .mat files using a GalAPAGOS sub-routine called convertCube (see Section 1.7). It should also be noted that when we generate the model galaxy, it is convolved with the beam in order to match the resolution of the model to that of the data.

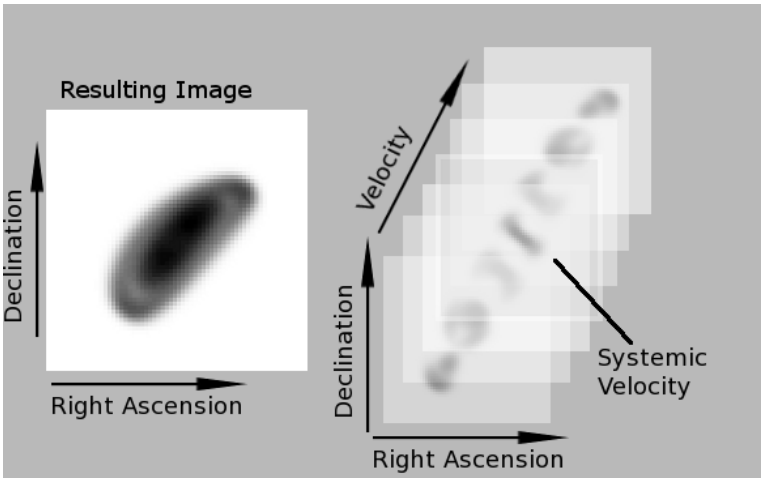

Figure 14: The left image of a galaxy, also known as a moment 0 map, is formed by combining the intensities of all of the slices in the right image, described in Section 2.5. The right image is the data cube resulting from the acquisition of data from a telescope. The three dimensions for this data cube are declination, right ascension, and velocity. As we progress through the cube, we increase in velocity as we go from image to image. As is conventional, all moment maps in this thesis have north to the top, and east to the left.

3.1 Artificial Galaxies

We chose to use artificial galaxies to test the parameter recoverability of GalAPAGOS, since when we create the artificial galaxies we know what each parameter value is, and can compare it to the value that GalAPAGOS found. Noise was added to the artificial galaxies in order to more accurately portray real data. Once GalAPAGOS was able to recover all of the input parameters successfully, it was deemed to be in working order, and we then proceeded to modelling real data.

The artificial galaxies were created using the Make Artificial Data (MAD) routine in GalAPAGOS. This routine creates an artificial galaxy with roughly the same signal-to-noise ratio and size of a galaxy of the user's choice. However, there is also the option to either use random values for each of the galaxy parameters, use the values set in the defaultPar file, or to set each value at the time of creation. Since the goal was to create realistic galaxies, the method used was to perform a literature search for a particular galaxy in our sample, set the found parameters in defaultPar, and make reasonable estimates for those (such as scale height, H) which were not available. These parameters

would then be used as the input parameters for the artificial galaxy. Using this method, the artificial galaxy would then somewhat resemble the type of observed galaxy that we intended to model. The exact values used will be given later on, in Table 3.

With these parameters set, the next set of options to choose from is whether or not to use the SDMs on the artificial galaxy. If one chooses not to use the SDMs, then the density profile of the galaxy is flat, and the values for the SDMs set in defaultPar are used. Next, the warp and twist parameters are set to "On" or "Off". If "Off" is chosen, then the warp and twist routine within the galaxy creation code of GalAPAGOS do not run, and no warp or twist are applied to the galaxy. Once the SDM and warp options are chosen, MAD generates the artificial galaxy and outputs two .fits files; one is the artificial galaxy with noise included, and one is the artificial galaxy with no noise added.

In this project, two types of noise generation for artificial galaxies were tested. In the original implementation of artificial galaxies, the average level of background noise of the particular galaxy data cube the artificial galaxy was modelled after was copied and then applied to the artificial galaxy. This method proved to be limited, in that the artificial galaxy needed to have the exact same size and resolution of the input data cube, and thus making artificial galaxies of different sizes was difficult. Therefore, the noise profile was then changed to be generated via a random Gaussian distribution of noise, applied to the entire artificial galaxy data cube. This allowed more consistency and customizability of the noise profile. The random Gaussian distribution of noise was applied by adding a Gaussian distribution with a mean of 0 and a variance equal to the standard deviation of the intensity of the artificial data cube.

For this research, NGC 3198 and NGC 2188 were chosen as the galaxies from which the artificial galaxy input parameters were based upon. The artificial galaxies were generated with both SDM and warp options being "on" and "off", in order to test how GalAPAGOS handled different density profiles and warps. The artificial galaxies were also created with a wide range of inclinations to test the ability of GalAPAGOS to model nearly edge-on or nearly face-on galaxies.

These galaxies were then tested by running GalAPAGOS with these as input galaxies, and the goal being to recover the input parameters with the various versions of the code (see Section 1.7.5), such as optically thin, and non-optically thin, etc. These results are outlined in section 4.1.

3.1.1 Artificial Galaxy Quality

We used observable characteristics (size, morphology, velocity range) of NGC 3198 and NGC 2188 as the guide for our artificial galaxies. However, there were not enough beams across the rise in the rotation curve for the artificial galaxies based on NGC 2188 to resolve the r_{0v} parameter, and the beam size was therefore decreased to 15". The beam size is 30" for artificial galaxies based on NGC 3198, as this allowed enough resolution elements across the rise to resolve the r_{0v} parameter. These beam sizes were chosen so that there were enough resolution elements across the rise of the rotation curve (i.e. before the r_{0v} parameter). We determined experimentally that three beams within r_{0v} are required in order for a galaxy's turnover to be well resolved, and approximately ten beams across the diameter of the galaxy in order to reliably model the rotation curve. This was done by binning the artificial galaxy data until the parameters r_{0v} parameter was no longer consistently recoverable, which occurred when there were less than three beams within R_{0v}. The other rotation curve parameters (a_v and v_0) were found to be not consistently recoverable when there were less than ten beams across the diameter of the galaxy. This was tested on both the NGC 3198 based artificial galaxy, and the NGC 2188 based artificial galaxy.

For the artificial galaxy based on NGC 3198, we used eighteen channels with a velocity resolution of $\Delta v = 20.67$ km/s per channel, leading to a velocity range of 372.06 km/s.

For the artificial galaxy based on NGC 2188, we used sixteen channels, with a velocity resolution of $\Delta v = 9.33$ km/s per channel, leading to a velocity range of 149.28 km/s.

3.2 HI Observational Data

Below, we present the HI observational data.

3.2.1 NGC 3198

The data used for NGC 3198 were gathered in the THINGS survey [Walter et al., 2008], and using the Very Large Array (VLA) on April 28, 2003. We produced two binned versions; a highly binned (low resolution) version used for testing the code, and a less binned (higher resolution) version to be used for modelling in GalAPAGOS.

"Low" Resolution The cube size was originally $1072 \times 1072 \times 72$, which was reduced to $61 \times 81 \times 36$ after binning and cropping. The beam size was originally 11.43" x 9.26", and after binning by a factor of ten in each spatial direction was 19.05" x 15.43", due to there originally being six pixels across each beam. After adopting a distance of 13.8 Mpc [de Blok et al., 2008], the original beam size was 764.7 pc x 619.5 pc, and after binning became 1.274 kpc x 1.032 kpc. There were three beams across the rise in the rotation curve, i.e. before the r_{0v} parameter, and thirty beams across the radius of the galaxy. The third axis (velocity) originally had seventy-two channels, and was binned by a factor of two, with a velocity resolution of $\Delta v = 10.37$ km/s per channel, leading to a velocity range of 373.32 km/s. The galaxy has a velocity amplitude of 145 km/s (as can be seen in the position-velocity diagram in Section 5.1, Fig. 26), which is well covered by the velocity range of the data. The reason for binning so extremely was to use this highly binned data to reduce the run time, so that more experimental runs could be feasible, and to quickly test that GalAPAGOS was working correctly.

"High" Resolution The cube size was originally $1072 \times 1072 \times 72$ and after binning and cropping was $121 \times 161 \times 72$. Due to limitations placed on GalAPAGOS coming from the Java heap space available in MATLAB, this is the highest resolution (i.e. least binned) version of the cube that we are currently able to model while still using the Java

code in GalAPAGOS. The default Java heap space available in MATLAB 2016b (384 Mb) is simply not large enough to store all of the information needed for cubes larger than the binned NGC 3198 data. Although the memory available could be increased, it was found that the code was still unable to successfully run with the heap space increased above the default value. This Java heap space issue is known to the MATLAB team, and currently has no solution. This issue will be addressed in future versions of GalAPAGOS, where the Java code will be rewritten in C (see Section 7.1).

The beam size was originally 11.43" x 9.26", which after adopting a distance of 13.8 Mpc [de Blok et al., 2008] is 764.7 pc x 619.5 pc, and after binning by a factor of five in each spatial direction remained the same, since there were originally six pixels across each beam. After binning, there were five beams across the rise in the rotation curve, i.e. before the r_{0v} parameter, and fifty-one beams across the radius of the galaxy. The third axis (velocity) originally had seventy-two channels, and was left unbinned, with a velocity resolution of $\Delta v = 5.18$ km/s per channel, leading to a velocity range of 373.32 km/s. The galaxy has a velocity amplitude of 145 km/s (as can be seen in Section 5.1, Fig. 26), which is well covered by the velocity range of the trimmed data cube.

The data are continuous and smooth, with no discernible gaps in any channel. The photometric centre is: R.A. 10h 19m 55.39s, Dec. 45d 32m 59.00s, and systemic velocity was previously determined to be 660 km/s [de Blok et al., 2008]. The moment zero map and the optical image of NGC 3198 are shown in Fig. 15. NGC 3198 is a gas rich SBc type galaxy. The HI content extends out to 568" or 38.0 kpc (3σ level), which is more than twice the radius of the optical disk. NGC 3198 was selected for study mostly as a test of GalAPAGOS, since it had been very well studied in de Blok et al. [2008], Begeman [1987], Sicking [1997], and Fraternali et al. [2002]. It has a distinct asymmetry in the channel maps, which is also a good test of the capability of GalAPAGOS to handle asymmetry through the application of twists and warps.

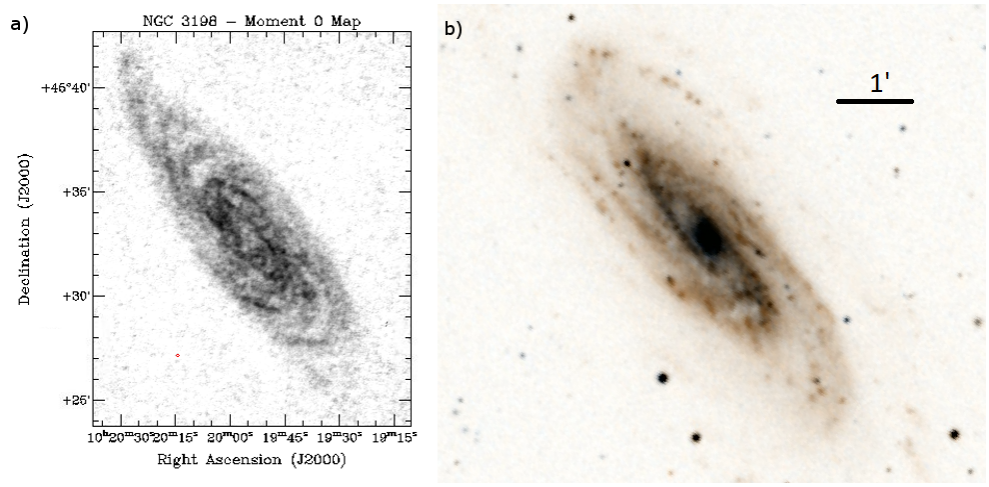

Figure 15: NGC 3198 - a) Moment 0 Map of NGC 3198 (unbinned data). The full velocity range was used, and the lower clip was set to 0.5σ. The beam size (red pixels in the lower left hand corner) was 11.43" x 9.26". We can see in this image that the HI radius of NGC 3198 is $\approx$ 7'. b) The optical (R-band) data of NGC 3198. We can see in this image that the optical radius of NGC 3198 is $\approx$ 3'. The image was taken from the HiPS survey, [Fernique et al., 2015], colorized by the Strasbourg astronomical Data Center [319, 2017].

3.2.2 NGC 2188

The HI data used for NGC 2188 came from the Local Volume HI Survey (LVHIS) [Kirby et al., 2011], and was taken using the Australia Telescope Compact Array (ATCA) on January 15, 2006. The original cube size was $512 \times 512 \times 50$ and after binning and cropping was $81 \times 101 \times 50$. The beam size was originally 47.63" x 28.33", which after adopting a distance of 7.9 Mpc [Tully, 1988] is 1.824 kpc x 1.085 kpc, and after binning by a factor of two in each spatial direction remained the same, since there were more than ten pixels across each beam. The velocity axis was left unbinned. There were two beams across the rise in the rotation curve, i.e. before the r_{0v} parameter, and five beams across the radius of the galaxy. Although these data have only two beams across the rise in the rotation curve, it is expected that the Square Kilometre Array (SKA) will have data of much higher resolution, with many beams across the rise. This is therefore an important preliminary investigation, which can be further explored with SKA data. The third axis (velocity) had fifty channels, with a velocity resolution of $\Delta v = 4$ km/s, leading to a velocity range of 200 km/s. The galaxy has a velocity amplitude of 55 km/s (as can be seen in Section 5.2, Fig. 38), which is well covered by the velocity range of the trimmed

data cube.

The data are continuous and smooth, with no discernible gaps in any channel. The photometric centre is: R.A. 6h 10m 9.90s, Dec. -34d 6m 31.97s, and the systemic velocity was previously determined to be 745 km/s [Meyers et al., 2004]. The moment zero map is shown in Fig. 16.

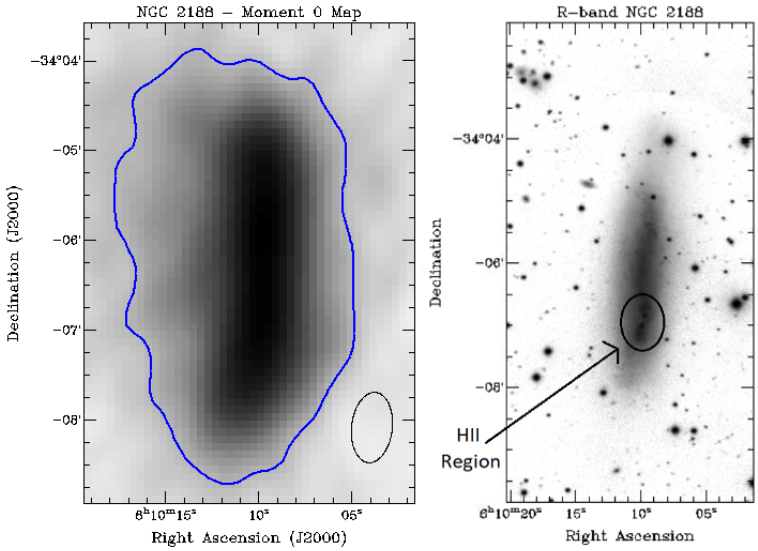

Figure 16: NGC 2188 - a) Moment 0 map of NGC 2188, with the 3σ level contour is plotted in blue, to show the extent of the HI outside of the disk. The full velocity range was used, and the lower clip was set to 0.5σ. The beam size (shown in the bottom right-hand corner) was 47.63" x 28.33". b) The optical (R-band) data of NGC 2188, with the HII region highlighted.

NGC 2188 is an edge-on ($i = 86°$) Magellanic type dwarf irregular galaxy. The north end of the optical disk is particularly gas deficient. That is, the gas along the major axis is truncated such that it aligns with the stellar disk extent. However neutral gas extends above and below the midplane over distances of more than 2 kpc. It also has a peculiar velocity field possibly arising from tidal interactions, ram pressure stripping, or blowout from the disk. These features were the primary inspiration for modelling NGC 2188 with GalAPAGOS. If a model of the normal disk rotation could be produced then we could confidently distinguish and analyze anomalous features. It has been previously studied as part of the LVHIS survey [Kirby et al., 2011], as well as in Domgorgen et al. [1996] and Eng [2010].

The optical data used to determine the extent of the stellar disk and HII region, discussed in Section 5.2, were provided by Robert Gleisinger and Dr. Jayanne English. It was an R-band CCD FITS file mosaic of three pointings along NGC 2188. Data were acquired at 2.3m telescope at the Siding Springs Observatory by Jayanne English in 2009. The mosaic produced by Gleisinger of photometrically calibrated data is shown in Fig. 16.

3.3 Molecular Gas Observational Data

Below, the CO observational data are presented. Note that many other data sets were explored, however we focus on those with successful results.

3.3.1 NGC 3665

The data for NGC 3665 were taken as part of the Atlas3D survey at the Owens Valley Radio Observatory (OVRO) on August 8, 2010, using the Combined Array for Research in Millimeter-wave Astronomy (CARMA) [Alatalo et al., 2013]. The original cube size was $513 \times 513 \times 92$ and after cropping was $90 \times 90 \times 92$, and was left unbinned. The beam size was 4.26" x 4.16", which after adopting a distance of 33.1 Mpc [Ems, 2011] is 683 pc x 668 pc. There was less than one beam across the rise in the rotation curve, i.e. the r_{0v} parameter, and three beams across the radius of the CO gas in the galaxy. The third axis (velocity) had ninety-two channels, with a velocity resolution of $\Delta v = 10$ km/s, leading to a velocity range of 920 km/s. The galaxy has a velocity amplitude of 325 km/s (as can be seen in Section 5.3, Fig. 46), which is well covered by the velocity range of the trimmed data cube.

The data are continuous and smooth, with no discernible gaps in any channel. The photometric centre is: R.A. 11h 24m 43.583s, Dec. 38d 45m 47.04s, and the systemic velocity was previously determined to be 2060 km/s [Onishi et al., 2017a]. The moment 0 map and optical image are shown in Fig. 17.

NGC 3665 is a nearby fast-rotator early-type (elliptical) galaxy. A fast-rotator is generally

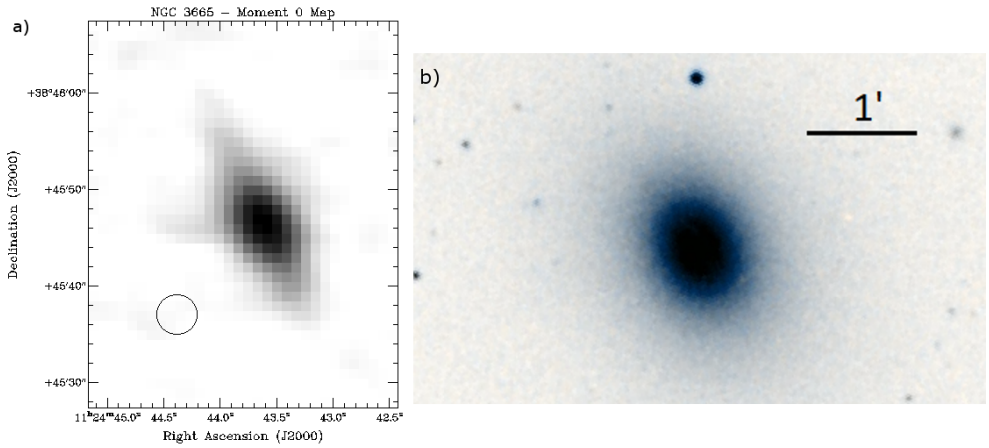

Figure 17: NGC 3665 - a) Moment 0 map of NGC 3665, the full velocity range was used, and the lower clip level was set to 0.5σ. We can see in this image that the radius of the CO disk in NGC 3665 is $\approx$ 0.2'. The beam size (4.26" x 4.16") is shown in the lower left-hand corner. b) The optical (R-band) data of NGC 3665. We can see in this image that the optical radius of NGC 3665 is $\approx$ 0.7'. The image was taken from the HiPS survey, [Fernique et al., 2015], colorized by the Strasbourg astronomical Data Center [366, 2017].

classified as an E or S0 galaxy that is fainter than a typical early-type galaxy, has a well aligned photometric and kinematic axis, and is nearly oblate, with disk-like components [IAU, 2007]. The CO data only contain the inner 12" (1.926 kpc) of the galaxy, although the gas disk extends further. The reason that the original researchers focused on the center 12" was to obtain high resolution data, and resolve the rotation of the center of the galaxy. The data were taken as part of the Atlas3D survey with the goal being to measure the mass of the supermassive black hole at the center of the galaxy, and possibly discern its characteristics in the kinematics [Onishi et al., 2017a].

This galaxy was selected for modelling in GalAPAGOS due to the high resolution of the data (relative to the HI data used), allowing us to resolve the inner kinematics and investigate the core/cusp issue (Section 1.4). Another reason for selecting this galaxy was that the CO data was contiguous, with no gaps anywhere in the data cube.

4 Analysis: Quality, Techniques, and Error Estimation

"*Outside of a dog a book is a man's best friend. Inside of a dog it's too dark to read.*"

— Groucho Marx

This section outlines the various analysis done involving GalAPAGOS. This will include the processes used to evaluate the functionality of the various versions of the code, along with the techniques used when applying GalAPAGOS to real data.

4.1 Testing GalAPAGOS Using Artificial Galaxies

GalAPAGOS was tested using the artificial galaxies described in Section 3.1.1. Since the generation of artificial galaxies used the same code as GalAPAGOS did for building models, the testing of artificial galaxies revealed a number of problems within GalAPAGOS which needed to be addressed before we could move on to modelling galaxies using CO.

The first major problem was that the structure of the data used by GalAPAGOS had been drastically changed since the time of the original code. Several components of the code then needed to be changed to use this new structure, and was the first task completed. Another challenge was that the GalAPAGOS position angle (PA) (see Section 2.3) of the galaxy model appeared to be incorrect, and required investigation. The different parameters used in the artificial galaxies for testing GalAPAGOS are outlined in Table 3. All of the above galaxies were created using the non-sparse, non-Java, non-optically thin code branch, as it was the simplest and easiest to understand code branch. The artificial galaxies were modelled after the HI data we planned to investigate; hence, the names in Table 3 reflect the galaxies that they were modelled after.

The PA problem was easiest, and was thus the first to be fixed. Previously, GalAPAGOS had a $+90^{\circ}$ offset internally to the input PA. This caused a multitude of issues due to

Galaxy Name	art3198-a	art3198-b	art3198-c	art3198-d	art2188
Parameter					
$r_{Out}\,(arcsec)$	450	450	450	450	110
$v_0\,(km/s)$	155	155	155	155	70
a_v	0.2	0.2	0.2	0.2	0.2
$N_{H,0}\,m^{-2}$	1×10^{25}	1×10^{25}	1×10^{25}	1×10^{25}	1×10^{25}
$T_s\,(K)$	100	100	100	100	100
$r_{0v}\,(arcsec)$	120	120	120	120	60
$H\,(arcsec)$	30	30	30	30	26
$v_\sigma\,(km/s)$	15	15	15	15	15
$v_{cm}\,(km/s)$	690	690	690	690	747
$dr_{Out}\,(arcsec)$	11	11	11	11	1
$inc\,(rad)$	1.26	1.26	1.26	1.26	1.52
$PA\,(rad)$	0.63	0.63	0.63	0.63	0
$xShift\,(arcsec)$	0	0	0	0	0
$yShift\,(arcsec)$	0	0	0	0	0
$iWarp0\,(rad)$	0	0	0.1745	0.1745	0.1745
$phiWarp0\,(rad)$	0	0	0.7854	0.7854	0.7854
$iWarp1\,(rad)$	0	0	0.1745	0.1745	0.1745
$phiWarp1\,(rad)$	0	0	0.7854	0.7854	0.7854
$maxTwistWarp\,(rad)$	0	0	0.5236	0.5236	0.7854
$SDM1$	1	-0.6	1	-0.6	-0.6
$SDM2$	1	0.4	1	0.4	0.4
$SDM3$	1	0	1	0	0
$SDM4$	1	-0.7	1	-0.7	-0.7
$SDM5$	1	0.1	1	0.1	0.1
$SDM6$	1	0.5	1	0.5	0.5

Table 3: The parameters used to create the various artificial galaxies. Galaxy art3198-a has the warp and the SDM parameters "turned off", which for the warp parameters means setting them to 0, and for the SDM parameters means setting them equal to 1. Galaxy art3198-b has the warp parameters off and SDM parameters on. Galaxy art3198-c has the warp parameters on and the SDM parameters off. Galaxy art3198-d has both the warp and SDM parameters on. art2188 has the warp and SDM parameters "on".

the many different areas in the code where the galaxy's axes are rotated, and the +90° offset has now been removed. This revealed some issues in the output fits writer, which were subsequently fixed.

Next there was an issue when using equation 2.17 for the conversion between intensity and brightness temperature for artificial data, specifically. This was due to an error in the beam size calculation within the artificial galaxy creation code, and was quickly solved by setting the beam size to be Beam Size = (Beam Major Axis)×(Beam Minor Axis).

Once this problem was resolved, it was initially found that although the parameter recovery, morphology, and the intensities of the model galaxies could reasonably be trusted, the density profiles could not be trusted. This was due to a bug causing the default SDM values to be used, rather than those found from the parameter search. This was fixed by changing the way the SDM values GalAPAGOS had found were applied to model the galaxy. The SDM values were initially stored in a vector under a MATLAB structure called Galaxy.SDM.values, and after the structure was updated, were stored under Galaxy.SDM1, Galaxy.SDM2, etc. The solution was to replace the default values found in the Galaxy.SDM.values vector with those from Galaxy.SDM1, Galaxy.SDM2, etc. For more information on the testing of artificial galaxies, please see Appendix A.

The sparse branch was then examined (see Fig. 8 for a diagram of the available branches of GalAPAGOS) once the tests were completed on the non-sparse branch of GalAPAGOS. This brought a number of additional problems to light. The first was that the model fit the artificial galaxy data remarkably well in the middle velocity channels, but had a poor fit in the first and last two velocity channels. This was due to a masking problem, where the major axis of the mask was offset 90° from the major axis of the galaxy. This problem was found in the convertCube code, and was fixed by addressing a programming error.

All branches in Fig. 8 have now been tested, and have successfully recovered the input artificial galaxy parameters. The success of the dimensionless branch can be seen in Fig. 18, which follows the same convention as the figures shown in Appendix A. This means

that both the sparse and non-sparse branches are capable of running the optically thin dimensionless code on CO data.

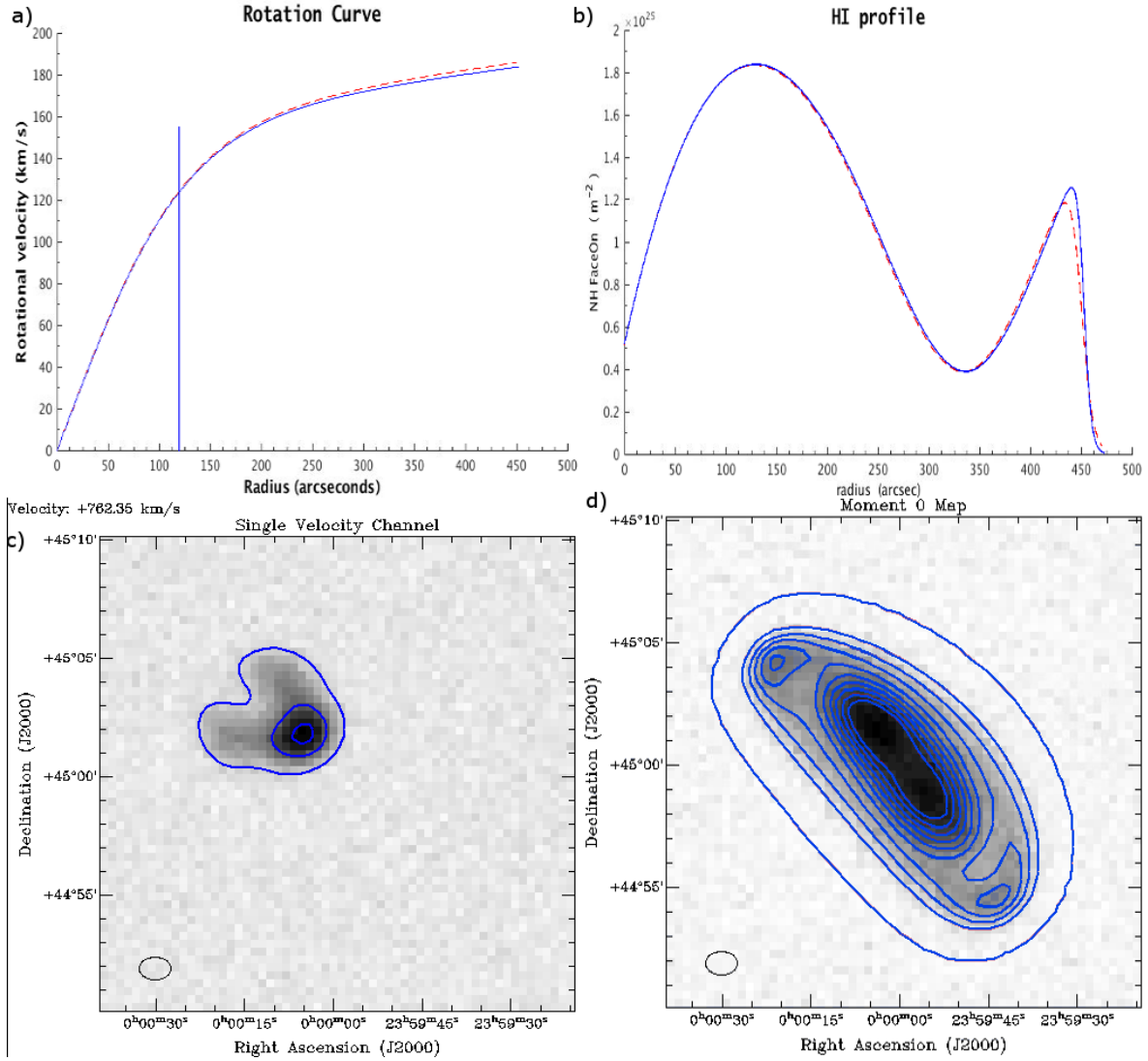

Figure 18: The input data was art3198-d (see Table 3), with noise. The best fit model (reduced $\chi^2 = 0.978$) produced after 1000 generations using the non-optically thin version of the code is shown. There were 6 SDMs searched for. Shown in a) is the input RC (red), and Model RC (blue). Note that the maximum difference in velocity is only 0.3 km/s. b) Input HI profile (red), Model HI profile, using 6 SDMs (blue). c) Single Velocity Channel Input is the greyscale data; the model is shown as the blue contour at the 3σ level. The maximum discrepancy found in the cube between the input artificial galaxy and the output model was 0.2x the beam size at the 3σ level. d) The zeroth moment map of the input and output models with the same contours as in c).

To summarize, although we further developed the optically thin version of GalAPAGOS, it is clear that these preliminary tests on artificial galaxies were successful for the sparse and non-sparse branches of the code, as well as the Java and non-Java branches. The

optically thin branches were also successful for the sparse, non-sparse, Java, and non-Java branches of the code.

4.2 Tools for Analyzing Observational Data

The primary tool for visualizing the results from the runs done on HI data were those within GalAPAGOS, such as plottingRoutine.m and viewSolutions.m (Section 1.7.4), as well as the KARMA package. The viewSolutions.m tool displays the 0 and 1st moment maps, rotation curve, and density profile of only one selected model, whereas plottingRoutine.m simultaneously displays the rotation curves and density profiles of multiple models. The tools within GalAPAGOS were used to select which model, from the large family of models generated, was the most accurate representation of the galaxy. The KARMA package was then used for detailed analysis after the model was exported as a FITS file.

Once a model is selected in GalAPAGOS, either plotting routine can be used to generate a FITS file of the model galaxy. The primary tools used within the KARMA package were "kvis" and "kpvslice". The kvis tool allows a user to view and modify data from a variety of formats, including all of those typically utilized for astronomical images. It provides a graphical user interface (GUI), which allows the user to apply contours at a chosen level, view and modify the intensity histogram, generate residuals, and perform various measurements on the data. The kpvslice tool allows the user to generate moment maps, and create position-velocity diagrams, as well as overlay images and create intensity profiles along a user specified axis.

In general, once we have the model, we remove the disk of the galaxy by using the model as a mask over the original data. This process was done in MIRIAD. This allows us to look outside of the disk for velocity anomalies which we investigate further. Removing the disk allows us to say with some certainty that the features we find are not a part of the stellar disk of the galaxy, and must be something else, such as inflow/outflow, a lagging halo, tidal interaction structures, or ram pressure stripping.

4.2.1 NGC 2188

Additional steps had to be taken before GalAPAGOS could generate a successful model of the galaxy disk, due to the peculiar structure of NGC 2188. It was found that on the first runs attempted (unmasked data), GalAPAGOS would find an unrealistically large scale height, and attempt to fit the extraplanar material found to the east of NGC 2188 as a warp, rather than simply fitting the stellar disk region. Note also that GalAPAGOS modelled NGC 2188 with a declining rotation curve $a_v \approx -0.9$, when the data were not masked out below a minimum intensity; meaning the extraplanar material had a velocity lower than the peak velocity amplitude. This could shed light on why some rotation curves at high redshift ($z \approx 0.6 - 2.6$) are observed to be declining [Genzel et al., 2017]. This means that rather than indicating an absence of DM, they could potentially be explained by inflow/outflow processes such as tidal interactions, ram pressure stripping, or a superbubble (see Section 1.3).

This problem was addressed by applying a mask to the observed data cube (see Section 3.2.2). Using MIRIAD, the masking was done by first making a smoothed cube of the NGC 2188 observational data in the spatial and velocity directions. Then at every voxel above the 5σ level of the smooth map, that voxel was taken from the original cube and placed in a new cube. All other voxels are set to zero in the new cube, and then the new cube was used as the input data to be modelled by GalAPAGOS, as presented in Section 5.2.

The 5σ level was chosen because, when examining the optical data (Fig. 19), it was found that this level (on the radio data) traced the vertical extent of the galaxy disk seen in the optical data. Note that this contour does encompass most of the vertical extent of the galaxy disk seen in the optical, and that some faint optical emission is ignored in the radial direction by applying this masking.

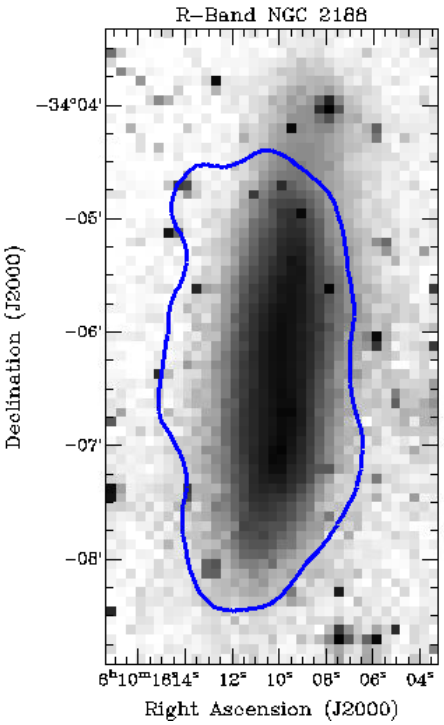

Figure 19: NGC 2188 - Optical data is presented as the greyscale, and the blue contour represents the 5σ level contour of the model. This contour was taken to be the vertical extent of the HI disk.

4.2.2 Determining the Error in Model Parameter Values

Determining the error in the modelling parameters is a relatively straightforward process, since we have a family of models produced by GalAPAGOS. First, we need to calculate the χ^2_ν value corresponding to the probability $P_\chi\left(\chi^2;\nu\right)$ of exceeding χ^2. This will allow us to determine what the change in χ^2_ν corresponding to the 1σ confidence level will be. A probability of $P_\chi\left(\chi^2;\nu\right) = 0.42$ (calculated using Eq. 4.1) corresponds to the 1σ confidence level. The probability is calculated by [Bevington and Robinson, 2003]

$$P_\chi\left(\chi^2;\nu\right) = \frac{1}{2^{\nu/2}\Gamma\left(\nu/2\right)} \int_{\chi^2}^{\infty} \left(\chi^2\right)^{(\nu-2)/2} e^{-\chi^2/2} d\left(\chi^2\right), \tag{4.1}$$

where ν is the number of degrees of freedom. For a 19-26 parameter fit ($\nu = 19, 26$), such as we use in GalAPAGOS, a change in the χ^2_ν of 1.1 corresponds to a $P_\chi\left(\chi^2;\nu\right) = 0.42$ [Bevington and Robinson, 2003]. Therefore, we take all models within 1 of the minimum χ^2_ν to be the 1σ error level. Furthermore, we can also say that a change of 0.X in the χ^2_ν corresponds to the $0.X\sigma$ error level (i.e. a change of 0.5 in the χ^2_ν corresponds to the 0.5σ

level).

After the run has finished and the family of models has been produced, we examine the distribution of parameter values relative to the χ^2_ν in order to determine the uncertainty in each parameter (see Fig. 20). To do this, we plot the modelling parameter value versus the χ^2_ν of the family of models. We then take the maximum difference between the parameter value of the best-fit model and any other model within a change in χ^2_ν of 1 as the 1σ error level in that parameter.

In regards to how many generations to run the code, at least fifty generations after the fitness has "flattened out" is usually adequate. This was determined via testing on artificial galaxies. This means that the minimum χ^2_ν found has remained constant for at least the most recent fifty generations. If one runs longer, there may still be slight improvements in the χ^2_ν, and the parameter space may continue to be further explored, possibly leading to more accurate error measurements. However, it is unlikely that once the χ^2_ν has remained constant for fifty generations that there will be any significant improvement in parameter values.

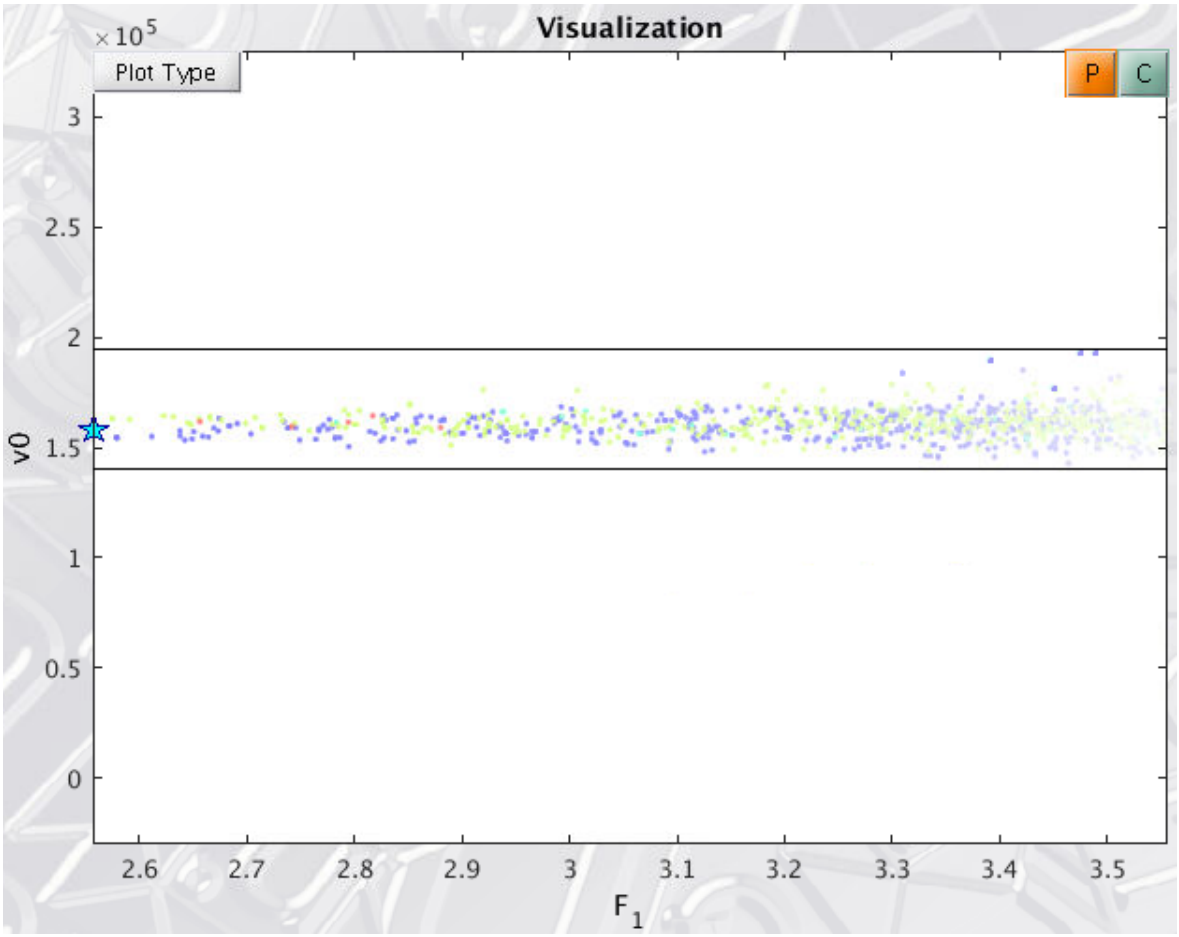

Figure 20: An example of how the error on the best-fit model parameter values were determined. The y-axis is the modelling parameter (in this case v_0) and the x-axis is the fitness (χ^2_ν). The error would then be taken as the maximum difference between the best-fit value (marked with a star) and any other value within the acceptable range of χ^2_ν. In this case, the parameter value v_0 with error was determined to be (with rounding) $v_0 = 160 \pm 30 km/s$.

5 Results

"*The true delight is in the finding out rather than in the knowing.*"

— Isaac Asimov

5.1 NGC 3198

We ran GalAPAGOS on NGC 3198 using both "low" and "high" resolution data (see Section 3.2.1). We used the "low" resolution data first as a test of GalAPAGOS, in order to verify it was in working order, as there are well known results to compare to [de Blok et al., 2008].

First, we modelled the "low" resolution data using four populations of two hundred and fifty individuals, with the run going for one hundred and twenty-eight generations. The minimum χ^2_ν found had remained constant since generation fifty-three. The run used the optically thin, sparse, Java branch of GalAPAGOS (branch 7 in schematic Fig. 8), with the warp turned on. The model used the latest version of GalAPAGOS, with the second SDM equation (Eq. 2.6), and using the mask radius found in convertCube as the outer radius r_{Out} (which was $r_{Out} = 581" = 38.9kpc$).

The best fit model had $\chi^2_\nu = 1.987$, and its parameters are listed in Table 4. There were 1,642 models found within the 1σ range. The rotation curves, density profiles, moment zero map, and position-velocity diagram figures are shown in Fig. 21, Fig. 22, Fig. 23, Fig. 25 respectively, and are shown alongside the "high" resolution results for comparison. The channel map is shown in Fig. 27 and 28.

GalAPAGOS was then run on the "high" resolution data (see Section 3.2.1), using four populations of two hundred and fifty individuals, with the run going on for one hundred and thirty-seven generations. The minimum χ^2_ν found had remained constant since generation fifty-three, although the run continued for one hundred and forty-eight generations. It was run on the optically thin, sparse, Java branch of GalAPAGOS (branch 8

in schematic Fig. 8), with the warp turned on. This modelling used the latter version of GalAPAGOS, with the second SDM equation (Eq. 2.6), and adopting the mask radius found in convertCube as the outer radius r_{Out} (which was $r_{Out} = 575" = 38.5kpc$).

The best fit model had $\chi^2_\nu = 2.989$, and its parameters are listed in Table 4. We note that the parameter set generated by GalAPAGOS for the "high" resolution data agree with the parameter set generated for the "low" resolution data. There were 2,232 models found within the 1σ range. The rotation curves, density profiles, moment zero map, and position-velocity diagram figures are shown in Fig. 21, Fig. 22, Fig. 23, Fig. 25 respectively, and are shown alongside the "low" resolution results for comparison. The channel map is shown in Fig. 29 and 30.

Between the "low" resolution and "high" resolution model, the % difference is in some cases high ($yShift$, $iWarp0$, SDM parameters), however all parameters are in agreement with each other within their error. Also note that the numerical difference between the $yShift$ and $iWarp0$ parameters is not large compared to the range of the parameters, and that the impact on models is small. In the case of a large % error for the SDM parameters, the output models are still quite similar. This is due to the degeneracies associated with the density, TScale, and SDM parameters, as well as the large error on the SDM parameters. The density profiles are observed to have a flat top due to there being many models which peak at $N_H = 10^{24}$, although at different radii. This is the upper limit of the density profile, although this can be altered by varying the $TScale$ value.

The rotation curves can then be used to find the total dynamical mass of the model. This is done by taking the velocity at the furthest radius possible (radius of the 3σ intensity level, $R = 568"$), and calculating the mass required for that velocity using Eq. 2.1b $\left(M(R) = \frac{V(R)^2 R}{G}\right)$. In the case of NGC 3198, the average velocity amplitude derived from the family of models at this radius (568") was $v_{final}(Low\,res) = 150 \pm 30$ km/s, $v_{final}(High\,res) = 150 \pm 10$ km/s. Using Eq. 2.1b, the total dynamical mass is then $M_{tot}(Low\,res)\,(R = 38.0kpc) = [4.0 \pm 0.8] \times 10^{41}$ kg, and in so-

Parameter	"Low" resolution value [unit]	"High" resolution value [unit]	% difference
v_0	$160 \pm 10[km/s]$	$155 \pm 7[km/s]$	0.3
a_v	$-0.1 \pm 0.2[unitless]$	$-0.1 \pm 0.1[unitless]$	0
$N_{H,0}$	$(3.6 \pm 0.2) \times 10^{24}[m^{-2}]$	$(3.6 \pm 0.2) \times 10^{24}[m^{-2}]$	0
r_{0v}	$60 \pm 50[arcsec]$, $4 \pm 3[kpc]$	$60 \pm 40[arcsec]$, $4 \pm 3[kpc]$	0
H	$15 \pm 10[arcsec]$, $1.0 \pm 0.6[kpc]$	$15 \pm 10[arcsec]$, $1.0 \pm 0.6[kpc]$	0
v_σ	$11 \pm 9[km/s]$	$14 \pm 5[km/s]$	24
v_{cm}	$677 \pm 7[km/s]$	$683 \pm 4[km/s]$	0.9
inc	$72 \pm 5[Deg]$	$70 \pm 2[Deg]$	2.8
PA	$143 \pm 4[Deg]$	$142 \pm 1[Deg]$	0.7
$xShift$	$-25 \pm 10[arcsec]$, $-1.7 \pm 0.6[kpc]$	$-25 \pm 10[arcsec]$, $-1.7 \pm 0.6[kpc]$	0
$yShift$	$20 \pm 10[arcsec]$, $1300 \pm 0.6[kpc]$	$17 \pm 6[arcsec]$, $1.1 \pm 0.5[pc]$	16.2
$TScale$	$0.5 \pm 0.3[unitless]$	$0.5 \pm 0.2[unitless]$	0
$iWarp0$	$2 \pm 5[Deg]$	$5 \pm 6[Deg]$	85.7
$phiWarp0$	$50 \pm 40[Deg]$	$50 \pm 40[Deg]$	0
$iWarp1$	$0 \pm 10[Deg]$	0 ± 4	0
$phiWarp1$	$50 \pm 40[Deg]$	$50 \pm 40[Deg]$	0
$MaxTwistWarp$	$20 \pm 10[Deg]$	$20 \pm 10[Deg]$	0
$SDM1$	$0 \pm 1[unitless]$	$0 \pm 1[unitless]$	0
$SDM2$	$0.1 \pm 0.9[unitless]$	$0.5 \pm 0.5[unitless]$	133
$SDM3$	$0.3 \pm 0.8[unitless]$	$0.3 \pm 0.8[unitless]$	0
$SDM4$	$-0.4 \pm 0.4[unitless]$	$-0.3 \pm 0.6[unitless]$	28.6
$SDM5$	$-0.8 \pm 0.2[unitless]$	$-0.7 \pm 0.3[unitless]$	13.3
$SDM6$	$-0.7 \pm 0.3[unitless]$	$0 \pm 1[unitless]$	200

Table 4: A table of the modelling parameters found with errors at the 1σ level (see Section 4.2) for NGC 3198 by GalAPAGOS. NGC 3198 is at a distance of 13.8 Mpc, and the results of the galaxy modelling are presented in Section 5.1.

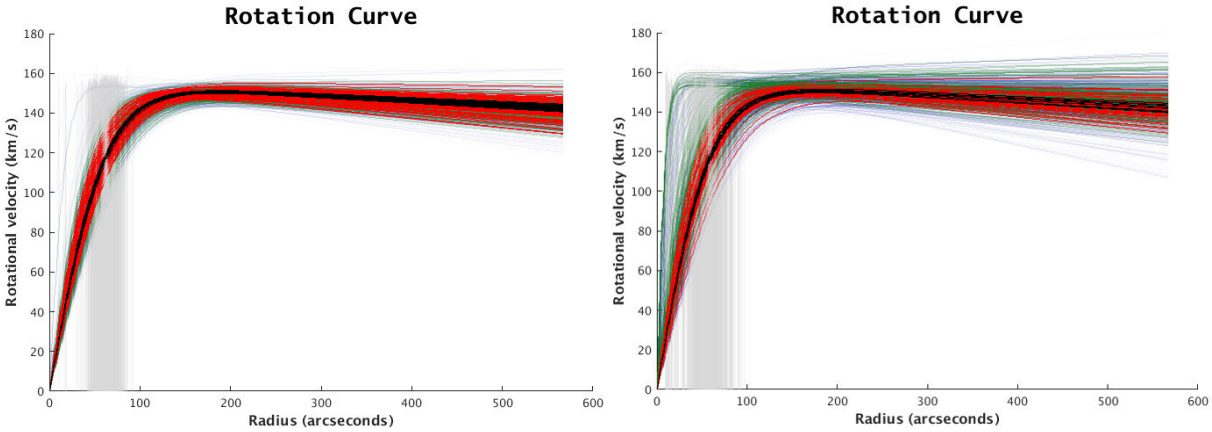

Figure 21: NGC 3198 Rotation Curves - The blue lines represent the 0.6σ to 1σ level, the green lines represent the 0.3σ to 0.6σ level, the red lines represent the 0.05σ to 0.3σ level, and the black lines represent the 0 to 0.05σ level. Left image: The rotation curves of the family of 2,232 best fit models for the "high" resolution data (beam size = 11.43" x 9.26") are shown. They are plotted out to the radius at which the data's intensity drops below 3σ of the noise (568" = 38.0 kpc). Right image: The rotation curves of the family of 1,642 best fit models for the "low" resolution data (beam size = 19.05" x 15.03") are shown. They are plotted out to the radius at which the data's intensity drops below 3σ of the noise (568" = 38.0 kpc). See Section 5.1.

lar masses, $M_{tot}(Low\,res)\,(R = 38.0kpc) = [2.0 \pm 0.4] \times 10^{10}\,\mathrm{M}_{\odot}$. For the high resolution data, $M_{tot}(High\,res)\,(R = 38.0kpc) = [4.0 \pm 0.2] \times 10^{41}\,\mathrm{kg}$, and in solar masses, $M_{tot}(High\,res)\,(R = 38.0kpc) = [2.0 \pm 0.1] \times 10^{11}\,\mathrm{M}_{\odot}$. These estimates are consistent with each other.

Fig. 26 illustrates that the higher resolution model more accurately traces the spatial position of data, which is expected. Additional comparions are given in Fig. 24 and Fig. 31. However, the "low" resolution model is still useful, as it only took ≈1 day to run, whereas the higher resolution model took ≈1 week to run using the "Champion" computer, described in Appendix B. The "low" resolution run still resulted in an accurate, although more loosely constrained, estimate of the total dynamical mass, as well as generating a reliable, albeit less accurate, trace of the morphological characteristics of NGC 3198.

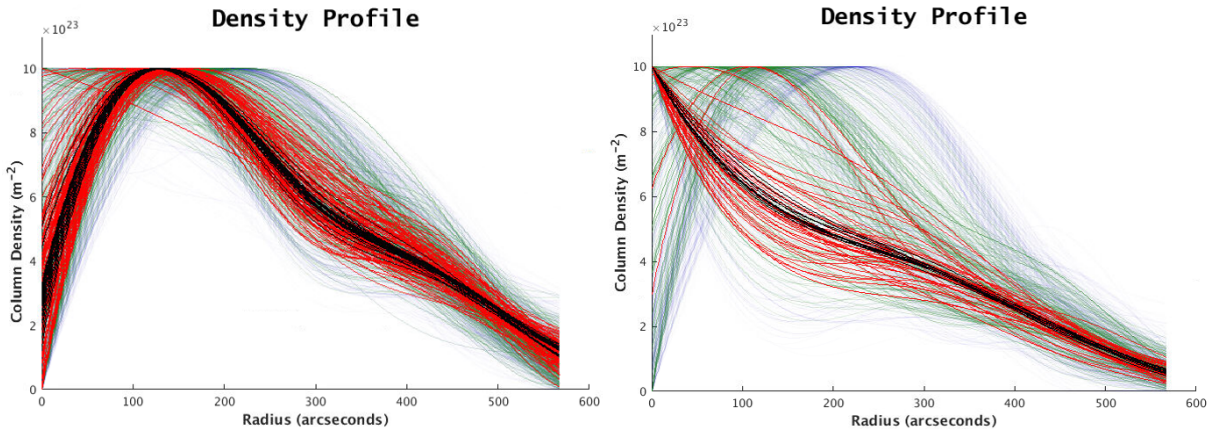

Figure 22: NGC 3198 Density Profiles- Left image: The blue lines represent the 0.6σ to 1σ level, the green lines represent the 0.3σ to 0.6σ level, the red lines represent the 0.05σ to 0.3σ level, and the black lines represent the 0 to 0.05σ level. The density profiles of the family of 2,232 best fit models for the "high" resolution data (beam size = 11.43" x 9.26") are shown. They are plotted out to the radius at which the data's intensity drops below 3σ of the noise (568" = 38.0 kpc). Right image: The color scheme is the same as in the left image. The density profiles of the family of 1,642 best fit models for the "low" resolution data (beam size = 19.05" x 15.03") are shown. They are plotted out to the radius at which the data's intensity drops below 3σ of the noise (568" = 38.0 kpc). See Section 5.1.

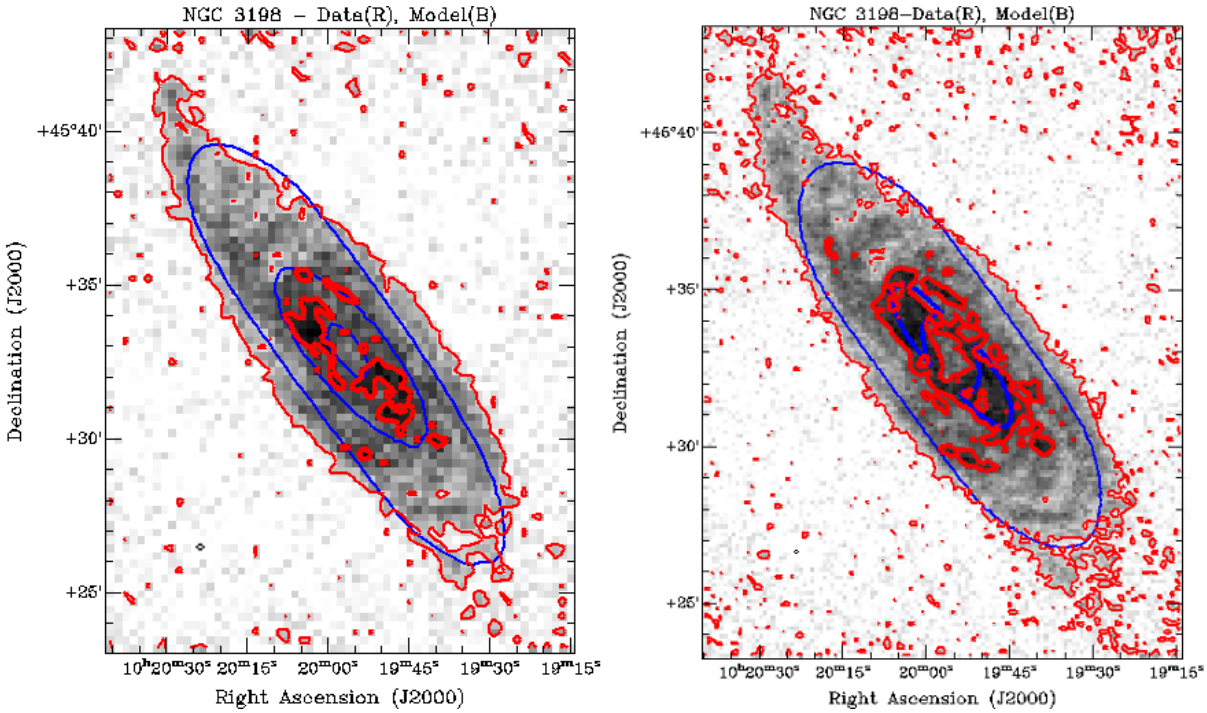

Figure 23: NGC 3198 Moment 0 Maps - In the left image, the "low" (10x bin) observational HI data is presented as the greyscale, with the red contours being a contour of the data at the 3σ and 10σ levels. The blue contours overlaid are the "low" resolution model contours, at the same levels as the data contours. In the right image the same contours are presented, however now with the "high" resolution (5x bins) observational data as the greyscale, and the "high" resolution model contours overlaid. The beam size for each ("low" resolution = 19.05" x 15.03", "high" resolution = 11.43" x 9.26") is shown in the bottom left hand corner of each image. For both moment maps, the full velocity range was used, and the lower clip was set to 0.5σ.

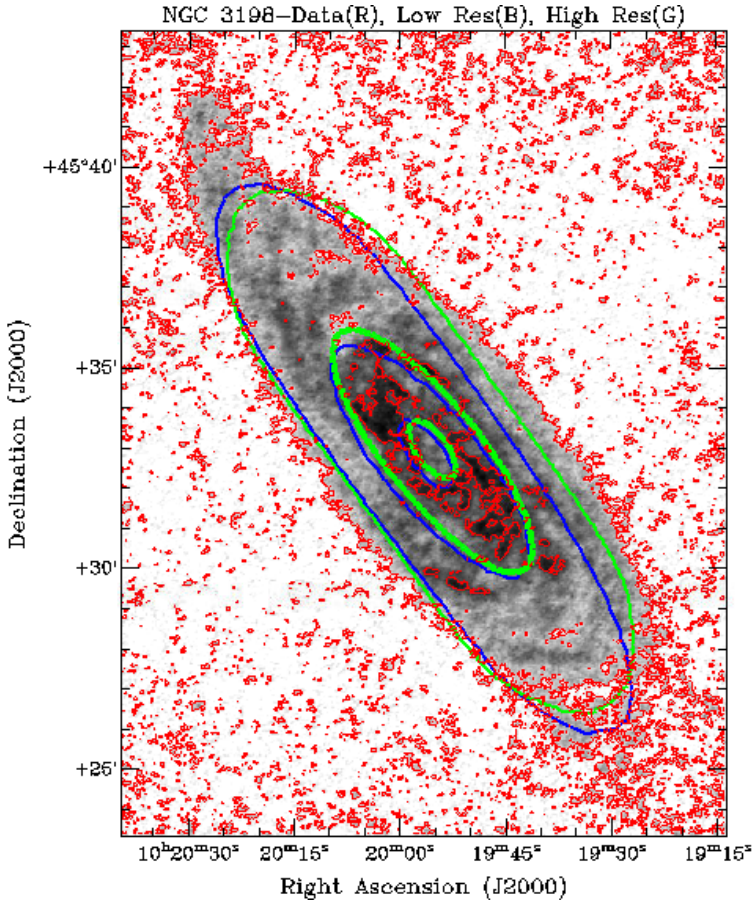

Figure 24: NGC 3198 Moment 0 Maps Comparing Two Models - The unbinned observational HI data is presented as the greyscale, with the red contours being a contour of the data at the 3σ and 10σ levels. The blue contours overlaid are the "low" (10x binned) model contours, at the same levels as the data contours. The green contours overlaid are the "high" (5x binned) model contours, at the same levels as the data contours. For all moment maps, the full velocity range was used, and the lower clip level was set to 0.5σ.

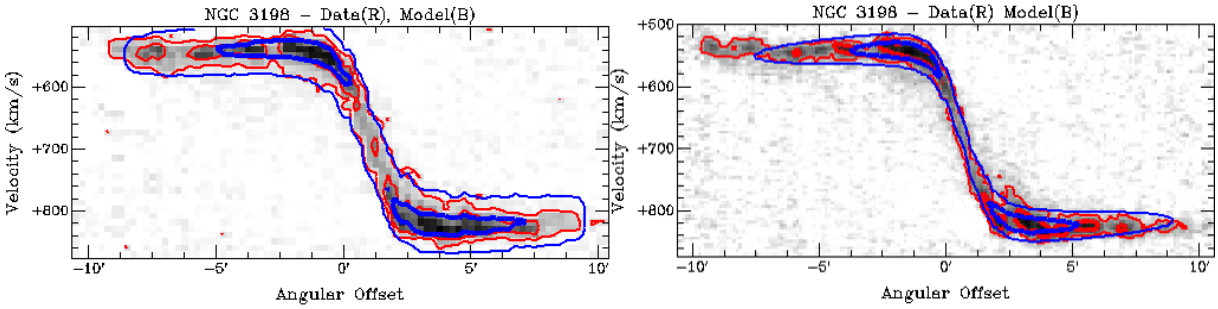

Figure 25: NGC 3198 Position-Velocity Diagram - In the left image, the "low" (10x bin) observational HI data is presented as the greyscale, with the red contours being a contour of the data at the 3σ and 10σ levels. The blue contours overlaid are the "low" resolution model contours, at the same levels as the data contours. In the right image the same contours are presented, however now with the "high" resolution (5x bins) observational data as the greyscale, and the "high" resolution model contours overlaid.

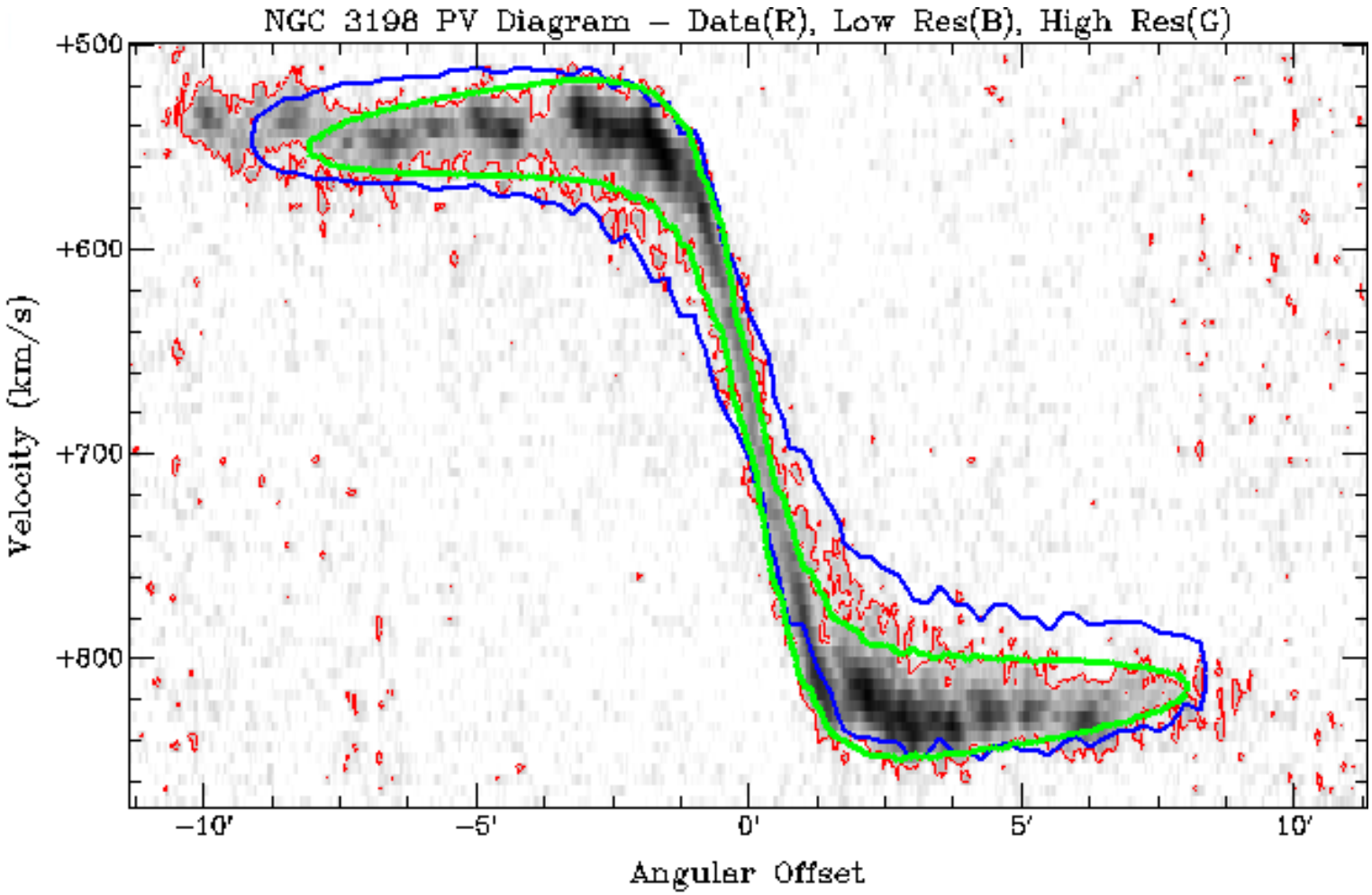

Figure 26: NGC 3198 Position-Velocity Diagram Comparing Two Models - The unbinned observational HI data is presented as the greyscale, with the red contour being a contour of the data at the 3σ level. The blue contour overlaid is the "low" (10x binned) model contour, at the same level as the data contour. The green contour overlaid is the "high" (5x binned) model contour, at the same level as the data contour.

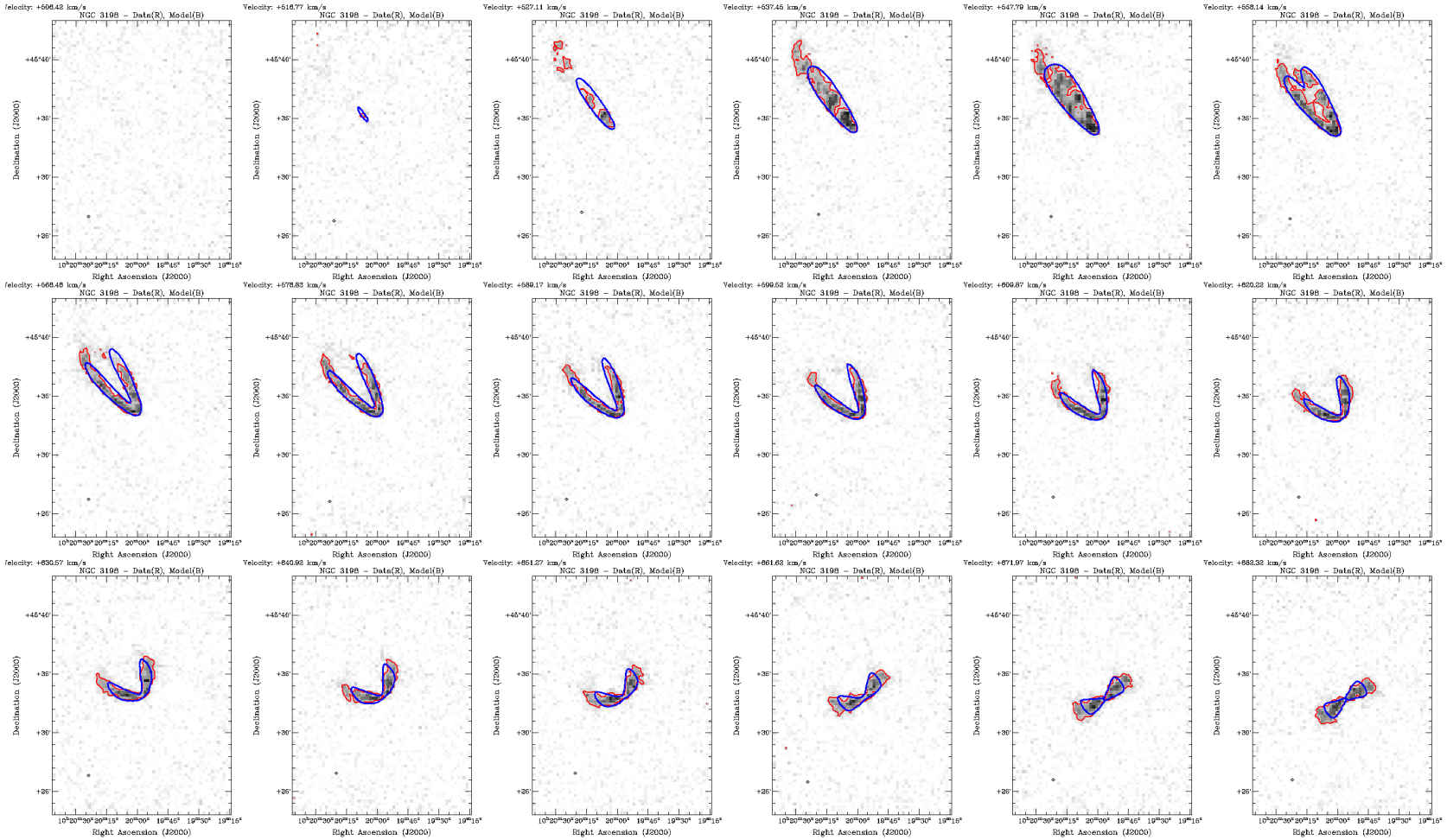

Figure 27: NGC 3198 "Low" Resolution Channel Map 1/2 - The first 18 channels of the "low" resolution NGC 3198 channel map are shown, with the other 18 shown in Fig. 28. The binned (10x) observational HI data is presented as the greyscale, with the red contour being a contour of the data at the 3σ level. The blue contour overlaid is the model contour, at the same level as the data contour. All channels with data present had a discrepancy between the data and the model which was at least the size of a beam, with the largest being 11x the beam size (19.05" x 15.43"), shown in the bottom left-hand corner of each channel, in the third channel.

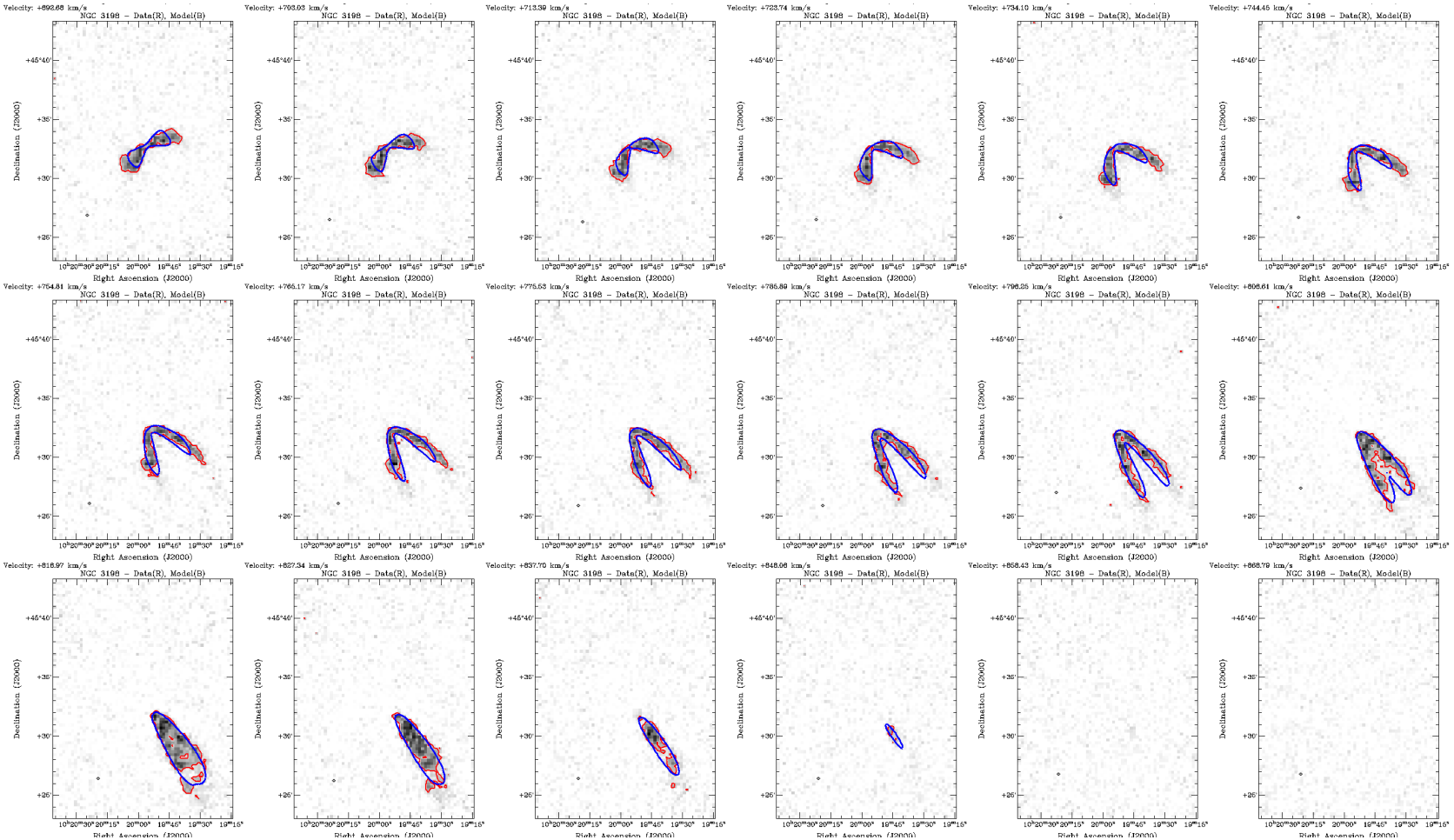

Figure 28: NGC 3198 "Low" Resolution Channel Map 2/2 - The last 18 channels of the "low" resolution NGC 3198 channel map are shown, with the other 18 shown in Fig. 27. The binned (10x) observational HI data is presented as the greyscale, with the red contour being a contour of the data at the 3σ level. The blue contour overlaid is the model contour, at the same level as the data contour. All channels with data present had a discrepancy between the data and the model which was at least the size of a beam, with the largest being 11x the beam size (19.05" x 15.43"), shown in the bottom left-hand corner of each channel, in the third channel, shown in Fig. 27.

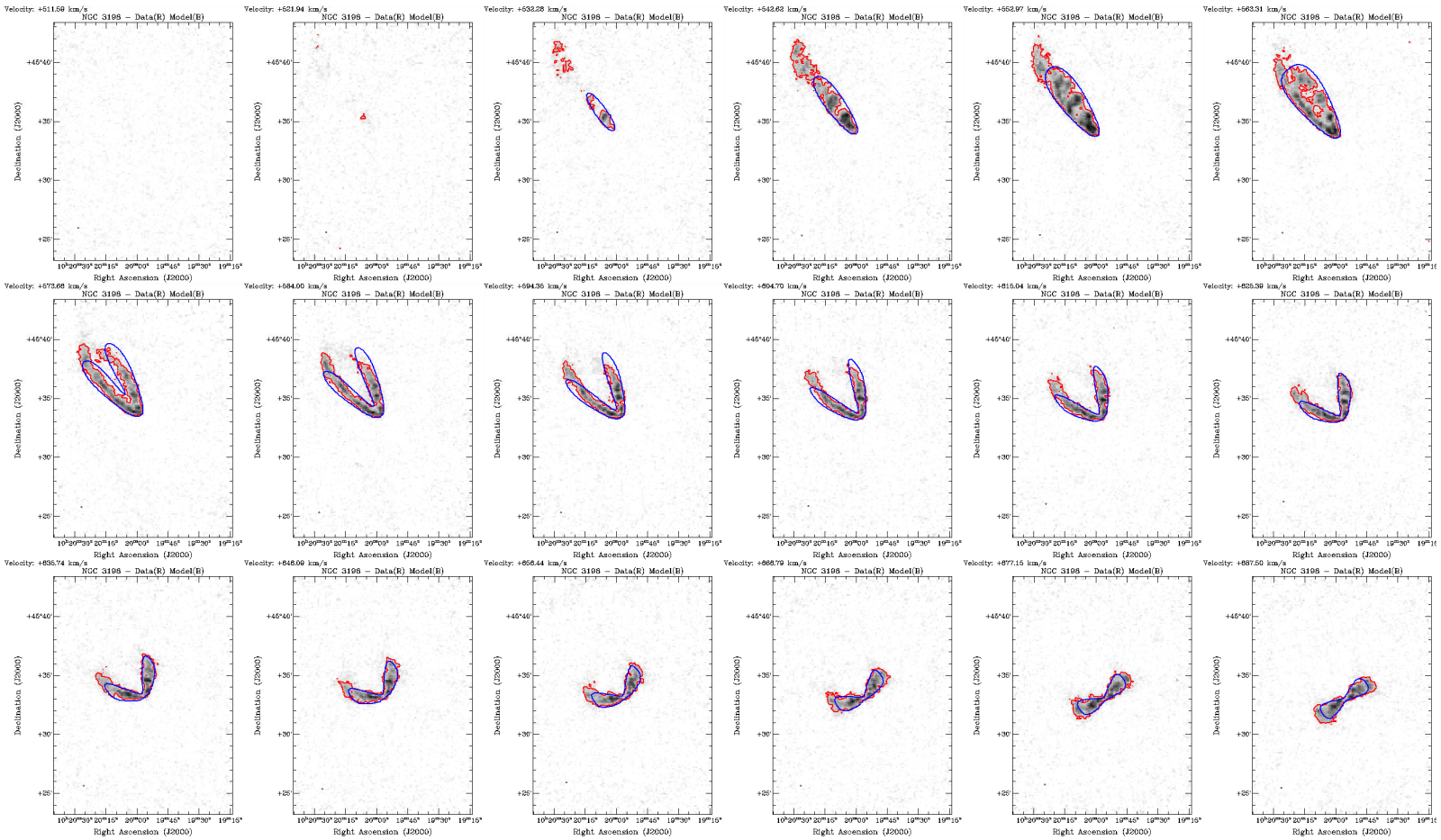

Figure 29: NGC 3198 "High" Resolution Channel Map 1/2 - The first 18 channels of the "high" resolution NGC 3198 channel map are shown, with the other 18 shown in Fig. 30. The binned (5x) observational HI data is presented as the greyscale, with the red contour being a contour of the data at the 3σ level. The blue contour overlaid is the model contour, at the same level as the data contour. All channels with data present had a discrepancy between the data and the model which was at least the size of a beam, with the largest being 20x the beam size (11.43" x 9.26"), shown in the bottom left-hand corner of each channel, in channel 7. Note that the data were binned by two in this image, simply for display purposes.

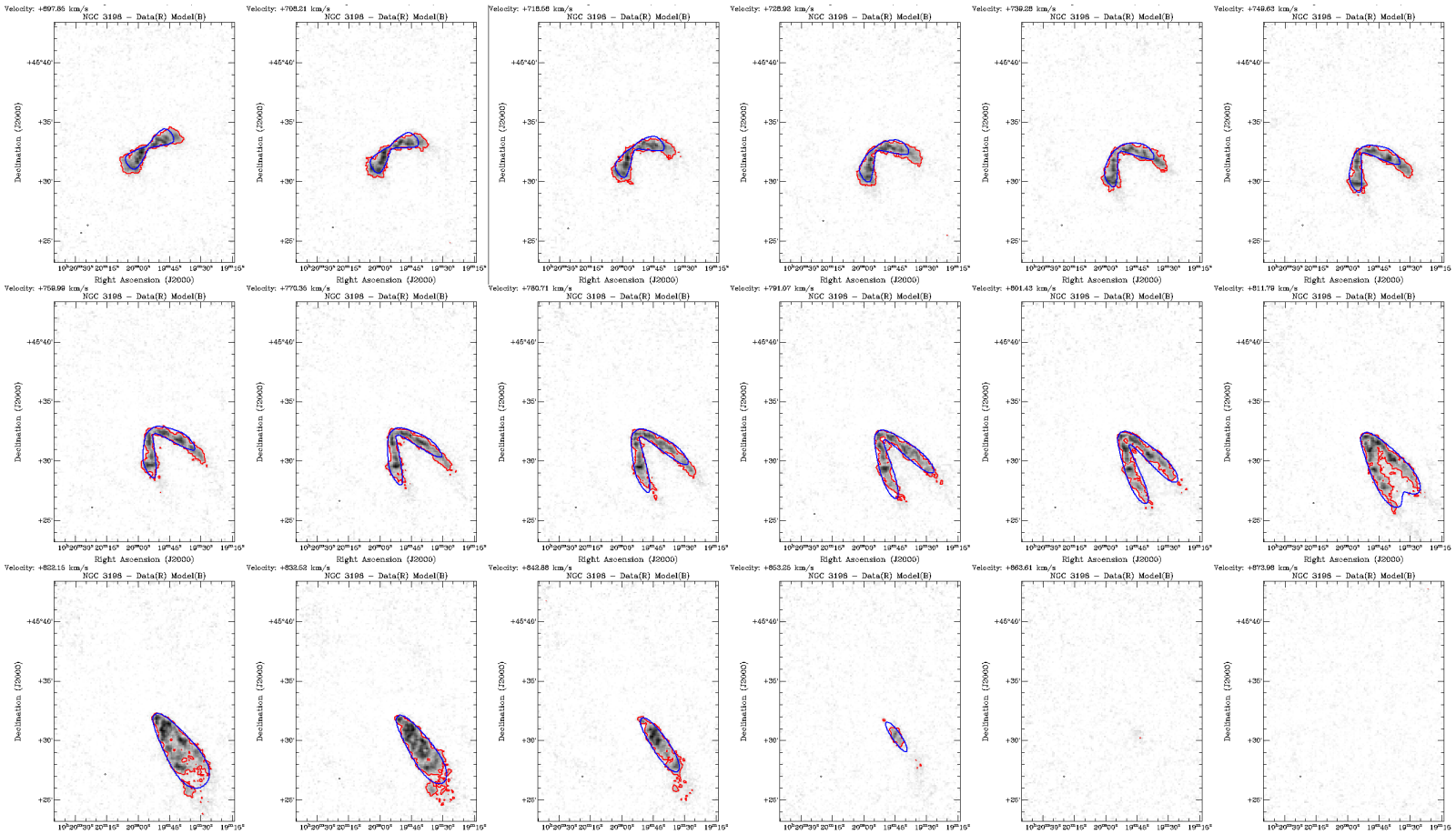

Figure 30: NGC 3198 “High” Resolution Channel Map 2/2 - The last 18 channels of the “high” resolution NGC 3198 channel map are shown, with the other 18 shown in Fig. 29. The binned (5x) observational HI data is presented as the greyscale, with the red contour being a contour of the data at the 3σ level. The blue contour overlaid is the model contour, at the same level as the data contour. All channels with data present had a discrepancy between the data and the model which was at least the size of a beam, with the largest being 20x the beam size (11.43” x 9.26”), shown in the bottom left-hand corner of each channel, in channel 7, in Fig. 29. Note that the data were binned by two in this image, simply for display purposes.

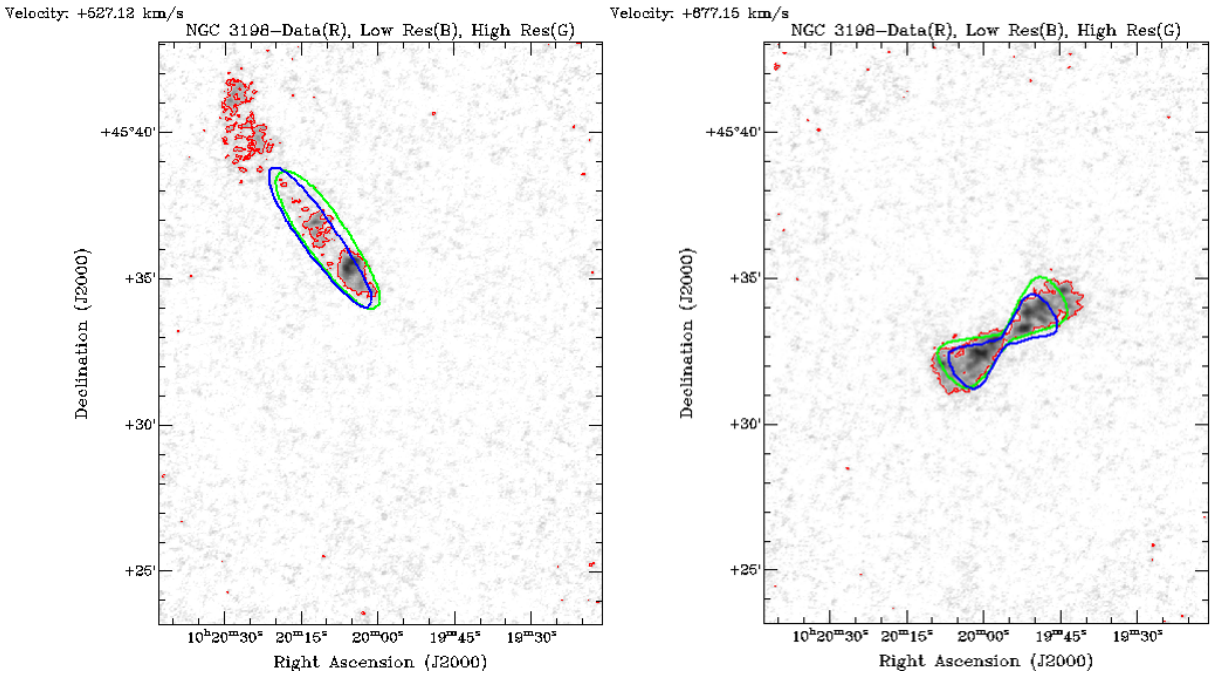

Figure 31: NGC 3198 Comparing Spatial Extents of Models - In the left image, the channel with the largest spatial discrepancy is presented. The unbinned observational HI data is presented as the greyscale, with the red contours being a contour of the data at the 3σ level. The blue contour overlaid is the "low" resolution model contour, at the same level as the data contour, and the green contour overlaid is the "high" resolution model contour, at the same level as the data contour. In the right image the same contours are presented, however the channel with the lowest discrepancy is shown.

5.2 NGC 2188

We ran GalAPAGOS on NGC 2188 (binned, cropped, and masked data, see Sections 3.2.2 and 4.2.1) using four populations of two hundred and fifty individuals, with the run going for two hundred and twelve generations. The minimum χ^2_ν found had remained constant since generation one hundred and fifty. It was run on the non-optically thin, sparse, Java branch of GalAPAGOS (branch 7 in schematic Fig. 8), with the warp turned on. The model presented here was generated using the latter version of GalAPAGOS, with the second SDM equation (Eq. 2.6), and using the mask radius found in convertCube as the outer radius r_{Out} (which was $r_{Out} = 171.6" = 6.57kpc$).

The best fit model had $\chi^2_\nu = 2.073$, and its parameters are listed in Table 5. There were 1,745 models found within the 1σ range. The rotation curves, density profiles, moment map, and position-velocity diagram figures are shown in Fig. 32, Fig. 33, Fig. 37, and Fig. 38, respectively. The channel map is shown in and Fig. 34, Fig. 35, and Fig. 35.

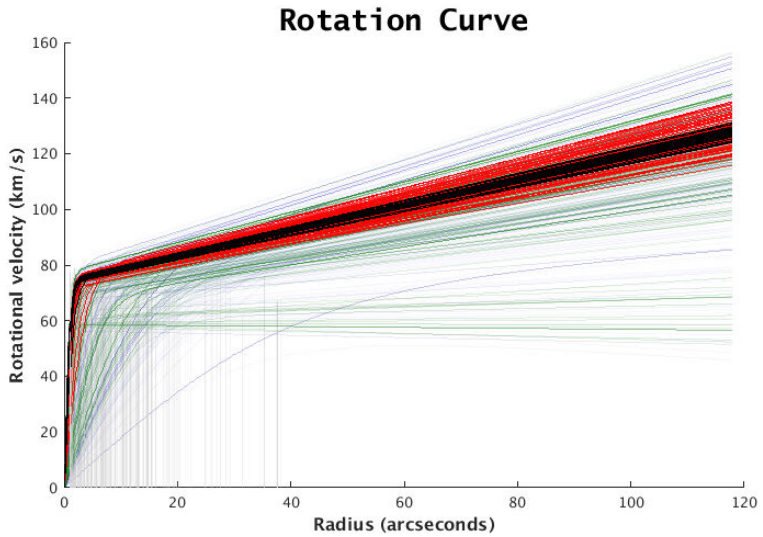

Figure 32: NGC 2188 Rotation Curves - The rotation curves of the family of 2,738 best fit models. The blue lines represent the 0.6σ to 1σ level, the green lines represent the 0.3σ to 0.6σ level, the red lines represent the 0.05σ to 0.3σ level, and the black lines represent the 0 to 0.05σ level. They are plotted out to the radius at which the data's intensity drops below 5σ of the noise (118" = 4.52 kpc), which represents the edge of the disk. See Section 5.2.

We recall that the intensities remaining in the masked data are associated with the

Parameter	Description [unit]
v_0	$70 \pm 10[km/s]$
a_v	$0.4 \pm 0.5[unitless]$
$N_{H,0}$	$(3.6 \pm 0.2) \times 10^{24}[m^{-2}]$
r_{0v}	$30 \pm 20[arcsec]$, $2300 \pm 1500[pc]$
H	$9 \pm 8[arcsec]$, $600 \pm 400[pc]$
v_σ	$24 \pm 6[km/s]$
v_{cm}	$754 \pm 3[m/s]$
inc	$89 \pm 8[Deg]$
PA	$0 \pm 10[Deg]$
$xShift$	$20 \pm 5[arcsec]$, $800 \pm 200[pc]$
$yShift$	$26 \pm 4[arcsec]$, $1000 \pm 200[pc]$
$TScale$	$6 \pm 3[unitless]$
$iWarp0$	$10 \pm 20[Deg]$
$phiWarp0$	$50 \pm 40[Deg]$
$iWarp1$	$0 \pm 20[Deg]$
$phiWarp1$	$50 \pm 40[Deg]$
$MaxTwistWarp$	$50 \pm 40[Deg]$
$SDM1$	$0 \pm 1[unitless]$
$SDM2$	$0.4 \pm 0.7[unitless]$
$SDM3$	$0.6 \pm 0.5[unitless]$
$SDM4$	$-0.4 \pm 0.7[unitless]$
$SDM5$	$0 \pm 1[unitless]$
$SDM6$	$0 \pm 1[unitless]$

Table 5: A table of the modelling parameters with errors (see Section 4.2) found for NGC 2188 by GalAPAGOS. NGC 2188 is at a distance of 7.9 Mpc, and the results of the galaxy modelling are presented in Section 5.2.

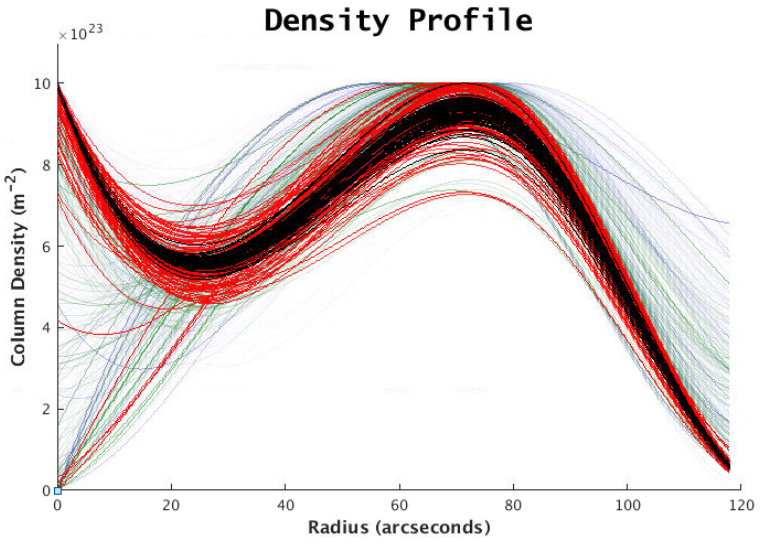

Figure 33: NGC 2188 Density Profiles - The density profiles of the family of 2,738 best fit models. The blue lines represent the 0.6σ to 1σ level, the green lines represent the 0.3σ to 0.6σ level, the red lines represent the 0.05σ to 0.3σ level, and the black lines represent the 0 to 0.05σ level. They are plotted out to the radius at which the data's intensity drops below 5σ of the noise (118" = 4.52 kpc), which represents the edge of the disk. See Section 5.2.

galaxy's disk region and excludes extraplanar material. The rotation curve can then be used to find the total dynamical mass of the model (since it is rising). This is done by taking the velocity at the furthest radii possible (radius of the 5σ intensity level, $R =$ 118"), and calculating the mass required for that velocity. In the case of NGC 2188, the velocity derived from the family of models at a radius of 118" (4.52 kpc) was 90 ± 40 km/s. Using Eq. 2.1b, the total dynamical mass is then $M_{tot}\,(R = 4.52kpc) = [1.7\pm0.8]\times10^{40}$kg, and in solar masses, $M_{tot}\,(R = 4.52kpc) = [8 \pm 4] \times 10^{9}\mathrm{M}_{\odot}$.

The model was then used as a guideline for where the galaxy disk is on the original HI unmasked data. The inclination of NGC 2188 is high ($\approx 89°$) and the goal of masking was to decouple disk emission from extraplanar features. We took the outer extent of the model to be where the intensity of the model went below 5σ. The choice to use the 5σ level was due to analysis on the extent of the galaxy disk using the optical data (see Section 4.2.1 for more information). We used the vertical extent of the model away from the major axis to represent the minor axis of the disk of NGC 2188. Therefore, anything in the observed cube outside of the model extent would then be a feature separate from the disk and considered to be above the plane. There was one such feature found to the

east of the disk.

This feature, seen in Fig. 39, is comprised of a central peak at a higher velocity, surrounded by lower velocities to the north and south. Shown in Fig. 39 is a renzogram image. This is a plot of the same single intensity iso-contour (with the intensity contour level set by the user) from multiple velocity channels. These contours are typically overlaid on a single channel or moment map. Each velocity channel has a different colour (chosen by the user) assigned to the contour. This allows the user to examine the velocity distribution of a particular feature throughout selected velocity ranges in the galaxy. All of these features are above the plane of the galaxy disk, defined by our model. This feature is discussed further in Section 6.2.

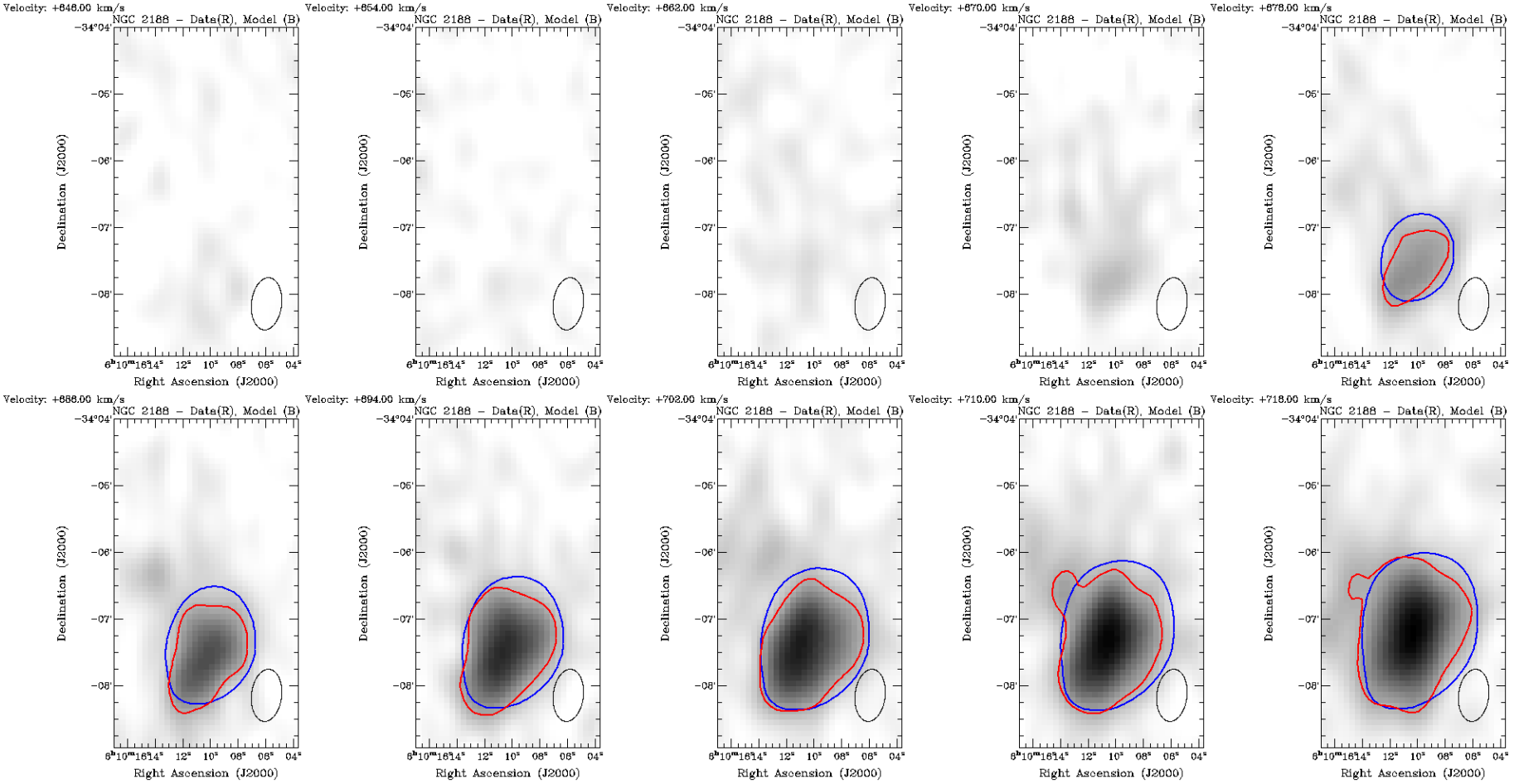

Figure 34: NGC 2188 Channel Map 1/3 - The first 10 channels of the NGC 2188 channel map are shown, with the other 20 shown in Fig. 35 and 36. The observational HI data is presented as the greyscale, with the red contour being a contour of the data at the 5σ level. The blue contour overlaid is the model contour, at the same level as the data contour. There is a total of two channels where the discrepancy between the data and the model was at least the size of a beam, with the largest being 1.1x the beam size (47.63" x 28.33"), which is shown in the bottom right-hand corner. The largest discrepancy is in the 11th velocity channel, with the other discrepancy being in the 15th channel.

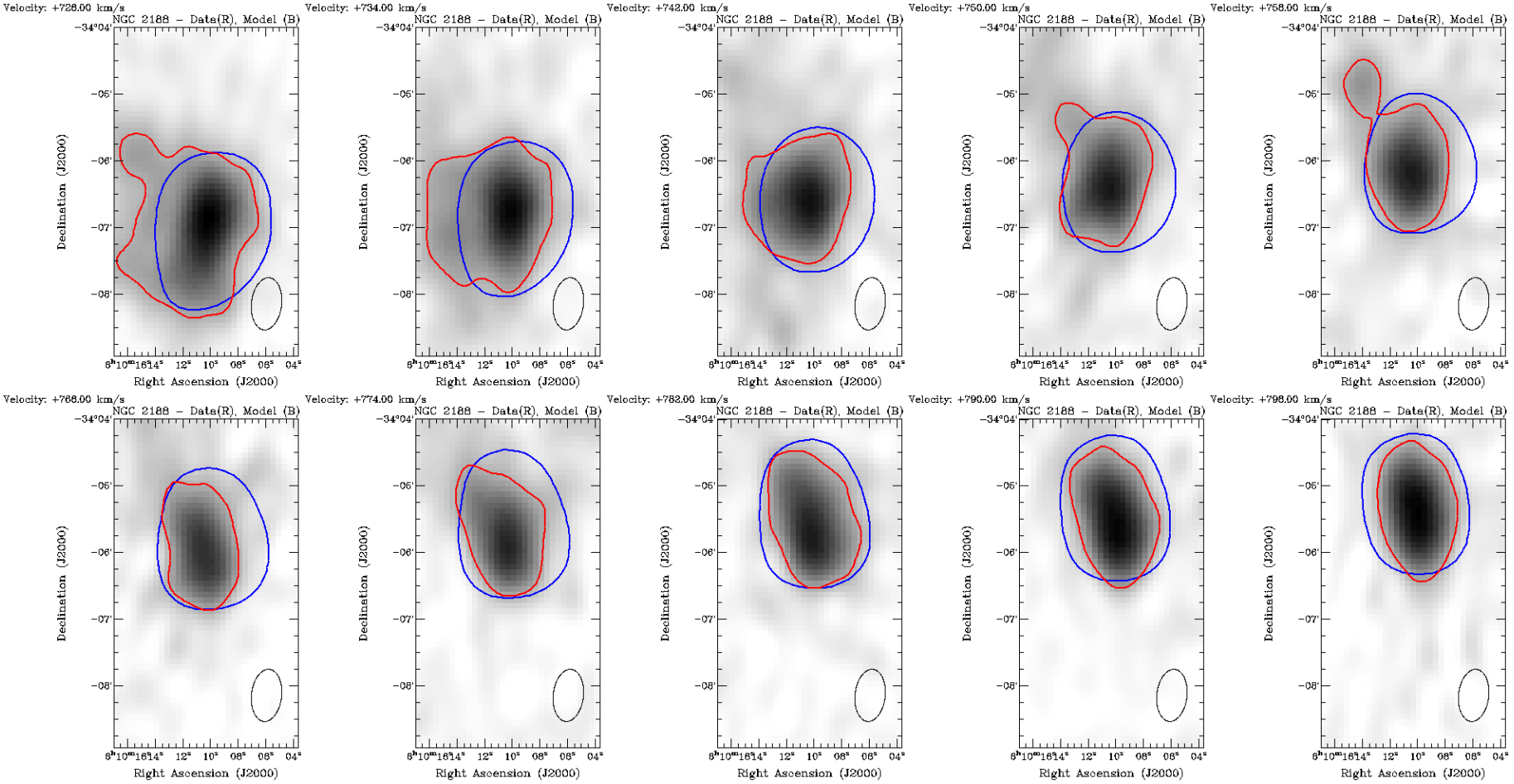

Figure 35: NGC 2188 Channel Map 2/3 - The middle 10 channels of the NGC 2188 channel map are shown, with the other 20 shown in Fig. 34 and 36. The observational HI data is presented as the greyscale, with the red contour being a contour of the data at the 5σ level. The blue contour overlaid is the model contour, at the same level as the data contour. There is a total of two channels where the discrepancy between the data and the model was at least the size of a beam, with the largest being 1.1x the beam size (47.63" x 28.33"), which is shown in the bottom right-hand corner. The largest discrepancy is in the 11th velocity channel, with the other discrepancy being in the 15th channel.

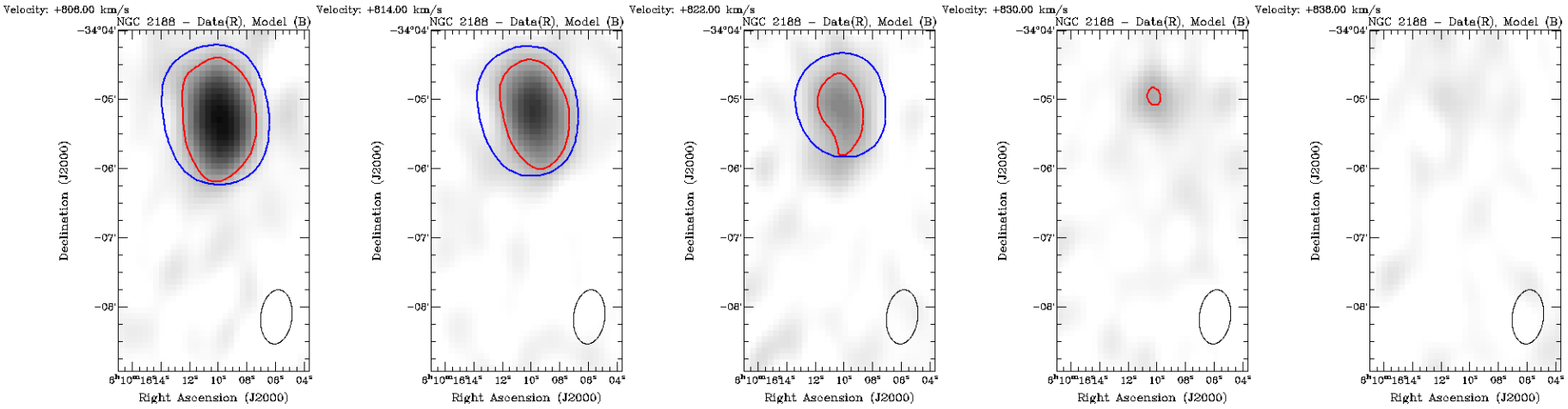

Figure 36: NGC 2188 Channel Map 3/3 - The last 10 channels of the NGC 2188 channel map are shown, with the other 20 shown in Fig. 34 and 35. The observational HI data is presented as the greyscale, with the red contour being a contour of the data at the 5σ level. The blue contour overlaid is the model contour, at the same level as the data contour. There is a total of two channels where the discrepancy between the data and the model was at least the size of a beam, with the largest being 1.1x the beam size (47.63" x 28.33"), which is shown in the bottom right-hand corner. The largest discrepancy is in the 11th velocity channel, with the other discrepancy being in the 15th channel.

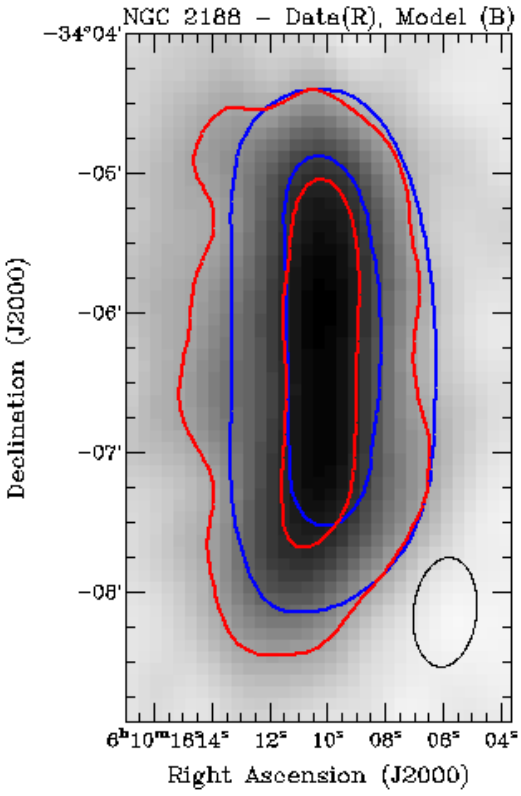

Figure 37: NGC 2188 Moment 0 Map - The observational HI data is presented as the greyscale, with the red contours being a contour of the data at the 5σ and 15σ levels. The blue contours overlaid are the model contours, at the same levels as the data contours. The beam is shown in the bottom right-hand corner. For both moment maps, the full velocity range was used, and the lower clip level was set to 0.5σ.

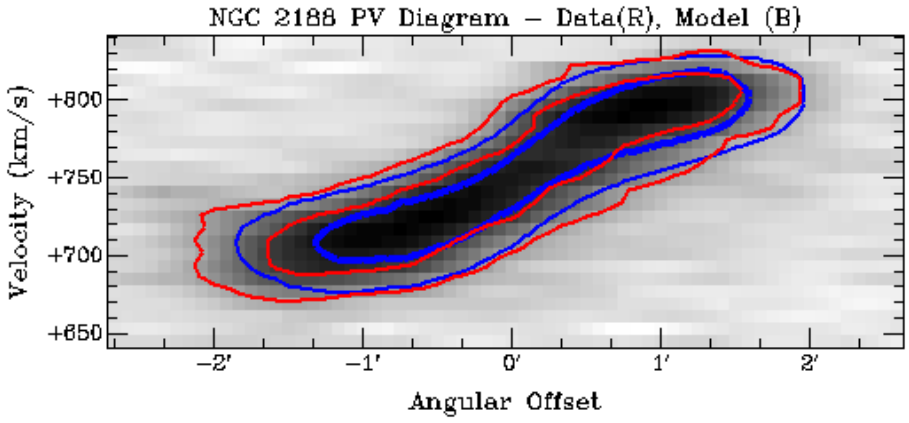

Figure 38: NGC 2188 Position-Velocity Diagram - The observational HI data is presented as the greyscale, with the red contours being a contour of the data at the 5σ and 15σ levels. The blue contour overlaid is the model contour, at the same levels as the data contours.

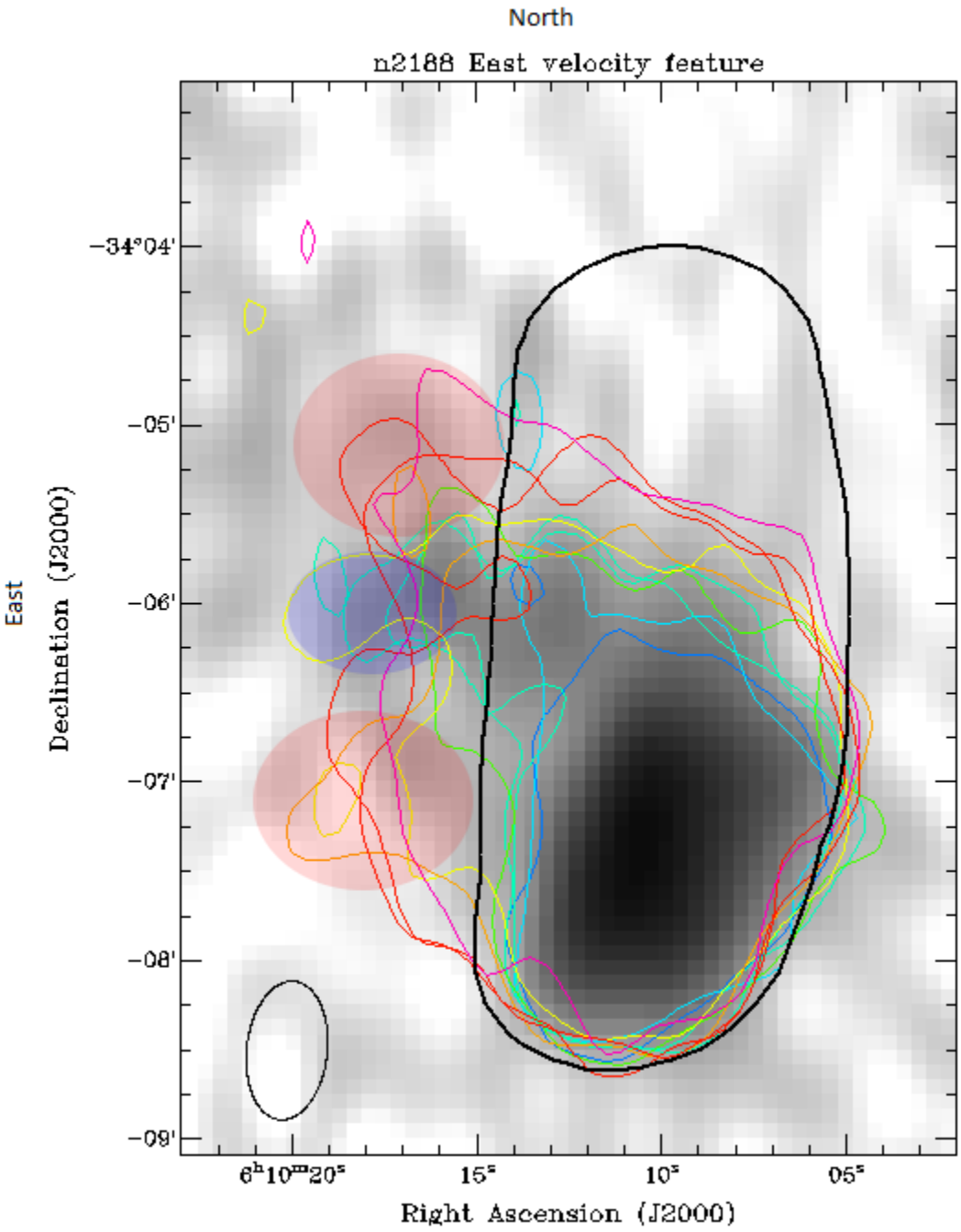

Figure 39: NGC 2188 Renzogram Figure - The greyscale background is the unbinned NGC 2188 data (Section 3.2.2), and the coloured renzogram contours are at the 4σ level of the data. That is, the same contour level is assigned a different colour per channel. Here we only plot channels 10-21. The black ring represents the extent of the model, which is taken to indicate the vertical extent of the HI disk of the galaxy. The feature to the east of this disk is highlighted via the blue and red ellipses along with the renzogram contours. It can be observed in the renzogram contours that there is a lower velocity (red) feature to the north and south of the higher velocity (blue) feature. The beam is shown in the bottom left-hand corner.

5.3 NGC 3665

We ran GalAPAGOS on NGC 3665 using four populations of two hundred and fifty individuals, with the run going on for six hundred and thirty generations. The minimum χ^2_ν found had remained constant since generation one hundred and eighty. It was run on the sparse, non-Java, optically thin, dimensionless branch of GalAPAGOS, with the warp functionality turned off, which corresponds to branch 6 in Fig. 8. The best fit model had $\chi^2_\nu = 0.9973$, and its parameters are listed in Table 6. There were 1,895 models found within the 1σ range. The model used the later version of GalAPAGOS with the second SDM equation (Eq. 2.6) , and used the mask radius found in ConvertCube as the outer radius r_{Out} (which was $r_{Out} = 32.6" = 5.23\,kpc$).

The best fit model was found to have parameters in agreement with measurements of the observed data [Onishi et al., 2017a] and general expectations of CO disks in the centers of early type galaxies. Also, the model channel maps that were well-matched morphologically to the data (see Fig. 42 - Fig. 44), and therefore the best fit model was used as the primary model for analysis. The moment 0 map, and position-velocity diagram of the best fit model are presented in Fig. 45, and Fig. 46, respectively. The channel map is shown in Fig. 42, Fig. 43, and Fig. 44.

Onishi et al. [2017a] use higher resolution data to generate a model via the Jeans Anistropic modelling (JAM) approach [Cappellari, 2012]. This approach uses Multi-Gaussian Expansion (MGE) Emsellem et al. [1994] to parametrize the observed galaxy's surface brightness. This detailed MGE is then used to reproduce the galaxy's velocity ellipsoid, and then extract information about the galaxy's kinematics.

The model adopted by Onishi et al. [2017a] does not use the same parametrization as GalAPAGOS. However, the parameters that appear in both models are shown in Table 7. We find that all values are in agreement with those found in Onishi et al. [2017a], except for the position angle parameter. This is simply because of differing conventions used (see Section 2.3 for GalAPAGOS PA). However, taking into account those differing

Parameter	Value [unit]
v_0	$350 \pm 50[km/s]$
a_v	$-0.2 \pm 0.8[unitless]$
$N_{H,0}$	$(3.6 \pm 0.2) \times 10^{24}[m^{-2}]$
r_{0v}	$6 \pm 5[arcsec]$, $1000 \pm 800[pc]$
H	$3 \pm 2[arcsec]$, $500 \pm 300[parsec]$
v_σ	$50 \pm 40[km/s]$
v_{cm}	$2,060 \pm 60[km/s]$
inc	$70 \pm 20[Deg]$
PA	$150 \pm 30[Deg]$
$xShift$	$1 \pm 2[arcsec]$, $200 \pm 300[pc]$
$yShift$	$1 \pm 2[arcsec]$, $200 \pm 300[pc]$
$TScale$	$5 \pm 3[unitless]$
$SDM1$	$0 \pm 1[unitless]$
$SDM2$	$0 \pm 1[unitless]$
$SDM3$	$-0.8 \pm 0.2[unitless]$
$SDM4$	$0 \pm 1[unitless]$
$SDM5$	$0 \pm 1[unitless]$
$SDM6$	$0 \pm 1[unitless]$

Table 6: A table of the modelling parameters found with errors at the 1σ level (see Section 4.2) for NGC 3665 by GalAPAGOS. NGC 3665 is at a distance of 33.1 Mpc, and the results of the galaxy modelling are presented in Section 5.3.

conventions, they do agree. The formula used to relate the two conventions is

$$P.A._{Onishi} = 180^\circ - P.A._{GalAPAGOS}. \tag{5.1}$$

The rotation curves and density profiles found for the models are presented in Figures 40 and 41.

The rotation curve was used to find the total dynamical mass of the model. We took the velocity at the furthest radius possible, and calculated the mass required for that velocity. In the case of NGC 3665, the average velocity derived from the "family" of models at a radius of 12", 1.93 kpc (radius of the 3σ intensity level), was 350 ± 150 km/s. Using Eq. 2.1b, the total dynamical mass is given by $M_{tot}\,(R = 1.93kpc) = [1.1 \pm 0.4] \times 10^{41}$kg, and in solar masses, $M_{tot}\,(R = 1.93kpc) = [6 \pm 2] \times 10^{10}\mathrm{M}_\odot$. The best-fit rotation curve generated by GalAPAGOS match well with the very high-resolution rotation curves found in Onishi et al. [2017b]. In both cases, the rotation curves begin to turn over at ≈ 1", and

Physical Parameter	GalAPAGOS Value	WISDOM Value
Distance	33.1 [Mpc]	34.7 [Mpc]
Spatial Galaxy Centre	RA=11:24:43.62, Dec=38:45:46.28	RA=11:24:43.62, Dec=38:45:46.28
Modelling Parameter	GalAPAGOS Value	WISDOM Value
v_σ	$50 \pm 40[km/s]$	$12.53 \pm 0.74[km/s]$
v_{cm}	$2,060 \pm 60[km/s]$	2,069 [km/s]
inc	$70 \pm 20[Deg]$	$69.90 \pm 0.20[Deg]$
PA	$150 \pm 10[Deg]$	26 [Deg]

Table 7: A comparison table between the parameters found by GalAPAGOS for NGC 3665 and those found by Onishi, K., et al, 2017. The physical parameters consist of the measurable quantities of distance to the galaxy, and the spatial galaxy centre. The common modelling parameters between models consist of the velocity dispersion, v_σ, the systemic velocity, v_{cm}, the inclination, and the position angle.

flatten out at ≈ 4". Therefore, our model is sufficiently successful in order to perform the following analysis.

Since the motivation for modelling NGC 3665 using the high resolution CARMA data was to constrain the inner rise of the rotation curve, as described in Section 2.1, we follow the method of de Blok et al. [1996] in order to measure the slope of the inner rotation curve. The "inner" part of the rotation curve can be defined a number of different ways. The first definition defines the inner rotation curve to be within $r = R_e/8$ [Cappellari et al., 2013b], where R_e is the effective radius of the galaxy. The effective radius of a galaxy is defined as the radius at which half of the total light of the system is emitted. For NGC 3665, $R_e = 4.94kpc$ [Davis et al., 2013], which resides outside of the gas disk. This is not a universal definition and there is much discussion in the literature over the definition of the "inner" distance. We add three definitions based on out investigations. One definition defines it to be within $r = r_{0v}$, which is the scaling factor to control the position of the turnover radius. Lastly, since the final measured data point at the 3σ level is at 1.93 kpc, which is within R_e for NGC 3665, we also use this "furthest" data point to define the inner rotation curve.

In log space, the "inner" slope of the rotation curve is defined as

$$slope = \frac{d\log V}{d\log R}. \tag{5.2}$$

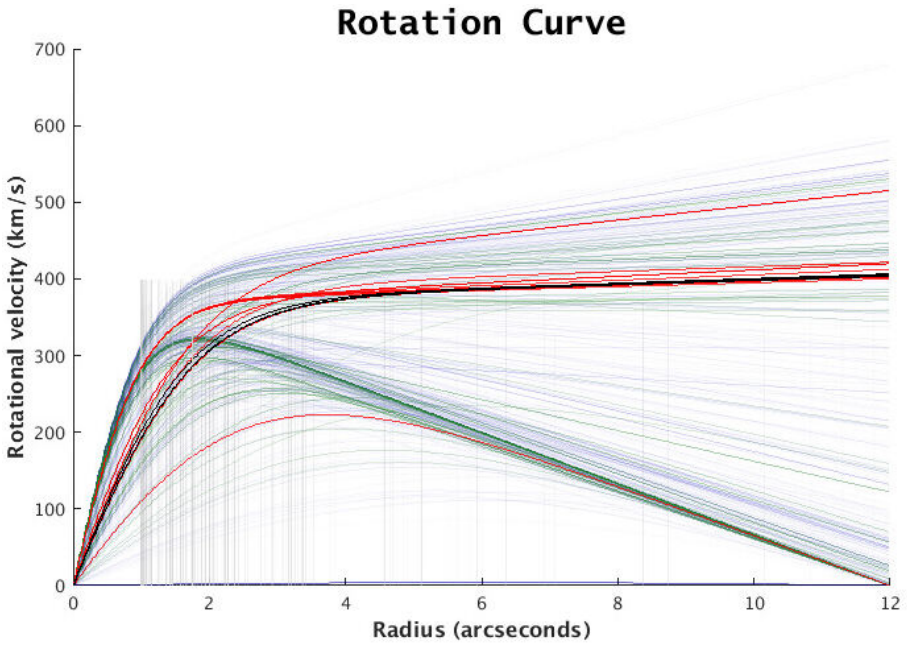

Figure 40: NGC 3665 Rotation Curves - The rotation curves of the family of 1,895 best fit models. The blue lines represent the 0.6σ to 1σ level, the green lines represent the 0.3σ to 0.6σ level, the red lines represent the 0.05σ to 0.3σ level, and the black lines represent the 0 to 0.05σ level. They are plotted out to the radius at which the data's intensity drops below 3σ of the noise (12" = 1.93 kpc). See Section 5.3

We then use this slope to look for a core ($slope = 1$), or a cusp ($slope = 0.5$) (see Section 1.4).

Looking at Fig. 47, we can see that most of the curves in log space would be poorly fit by a single linear fit. In fact, doing a single linear fit to the logarithmic rotation curve would leave non-random residuals, meaning that it would be inappropriate to use a single linear fit. Instead, we use two linear fits; one fit to find the slope of the rise, and another fit to find the slope after apparent turnover in the curve. We then take the slope of the rise to be the slope of the logarithmic rotation curve.

The inner linear fit was fit using $f_1(x) = M_1 x$, where M_1 is the slope of the rise. The second fit (after the turnover), was fit using $f_2(x) = M_2 x + c$, where M_2 is the slope of the curve after the turnover, and c would be the y-intercept of the fit. In Table 8 we include the slope of $f_2(x)$, M_2, but omit the values of the y-intercept c since they are not relevant to our discussion of the core/cusp issue.

The fit for each of the 1,895 models was a weighted linear fit, weighted by the inverse-

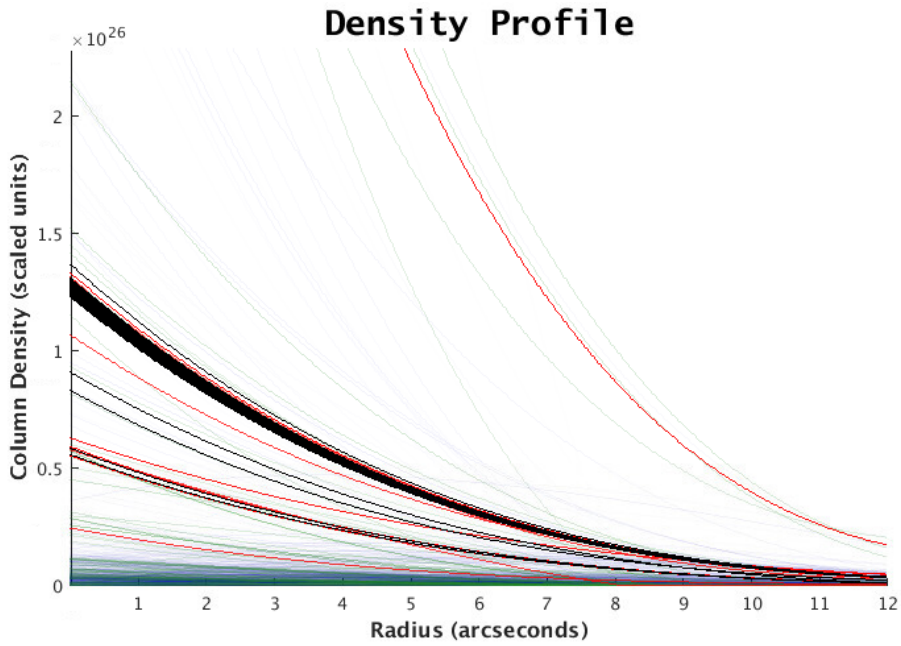

Figure 41: NGC 3665 Density Profiles - The density profiles of the family of 1,895 best fit models. The blue lines represent the 0.6σ to 1σ level, the green lines represent the 0.3σ to 0.6σ level, the red lines represent the 0.05σ to 0.3σ level, and the black lines represent the 0 to 0.05σ level. They are plotted out to the radius at which the data's intensity drops below 3σ of the noise (12" = 1.93 kpc). In this figure, Eq. 2.6 is multiplied by the $TScale$ parameter in order to condense the curves for visualization purposes. See Section 5.3.

squared error in the least squares fit. The final slope and error are determined by first calculating the average value of the slope for all fits, and then calculating the standard deviation. This analysis is used in Section 6.3 to discuss its implications in the core/cusp problem (see Section 1.4).

Slope with a given radius	Slope within $R = r_{mask}$ (5.23 kpc)	Slope within $R = r_{0v,best-fit}$ (280pc)	Slope within $R = r_{LastPoint}$ (1.93 kpc)	Slope within $R_e/8 = 620pc$
M_1	1.0 ± 0.2	1.0 ± 0.2	1.0 ± 0.2	1.0 ± 0.3
M_2	-1 ± 2	0.3 ± 0.1	0.0 ± 0.2	0.7 ± 0.1

Table 8: Fit parameters to a linear fit of log(V)/log(R). The slope is defined as a linear fit to log(V)/log(R). A slope (M_1) of 1 would indicate that the rotation curve rises linearly within the radius, and a slope of 0.5 would indicate that the rotation curve rises as the square root of the radius. The slope M_2 is the slope after the apparent turnover in the curve. The average was found from the family of 1,895 models, and the error was determined by their standard deviation. Column 2 has the slope within the model's mask radius $r_{mask} = 32.6$" (5.23 kpc). Column 3 has the slope within the best-fit model's "turnover" radius, $r_{0v} = 1.75$" , which was 280pc. Note that this corresponds to the value of the best-fit model. Column 4 has the slope within the furthest measurable data point at the 3σ level (1.93 kpc), since this is within the effective radius $R_e = 4.9kpc$. Column 5 has the slope within $R_e/8$, since in Atlas3D paper XX [Cappellari et al., 2013b] this is how the "central" region was defined.

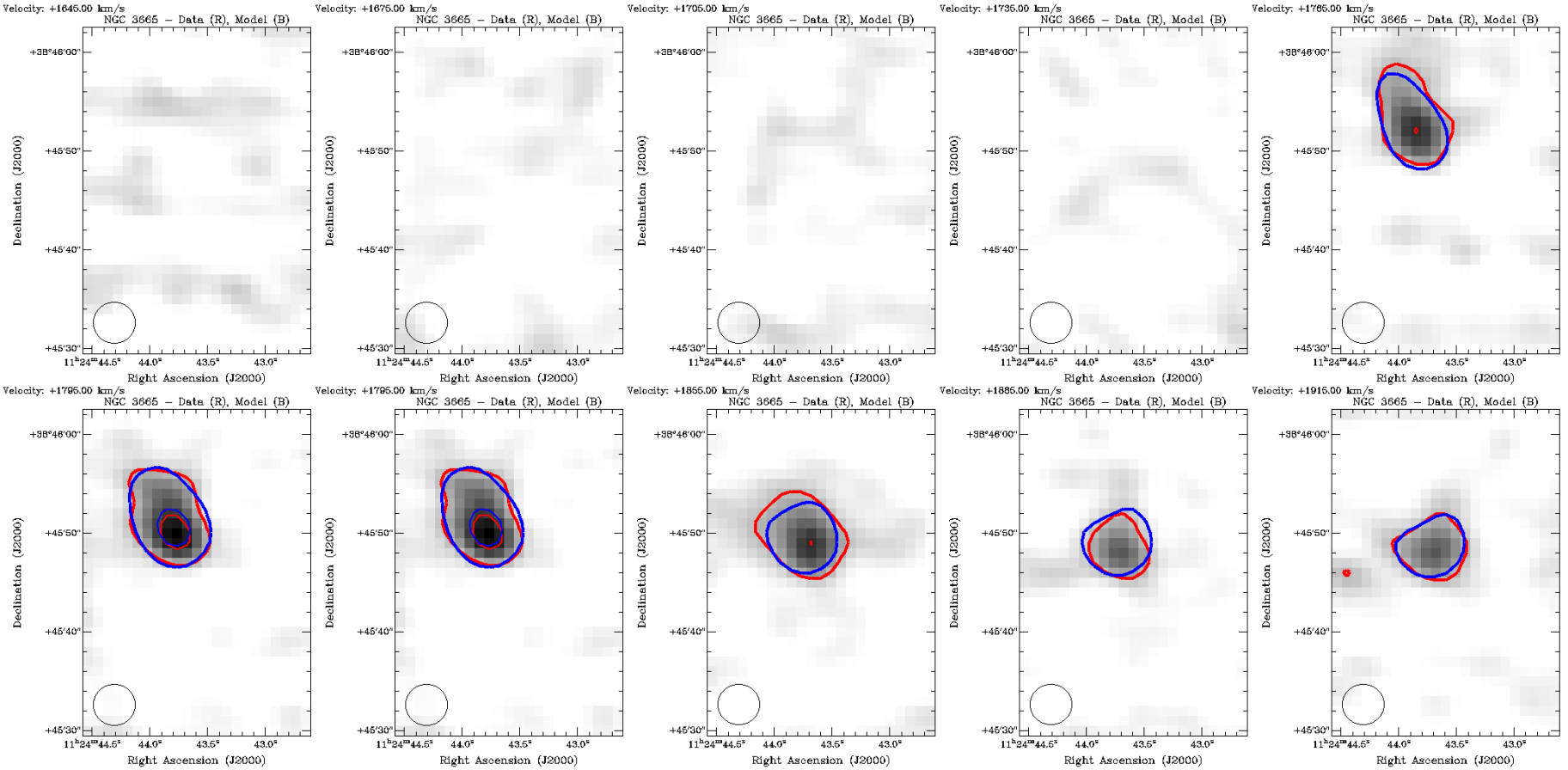

Figure 42: NGC 3665 Channel Map 1/3 - The first 12 channels of the NGC 3665 channel map are shown, with the other 24 shown in Fig. 43 and Fig. 44. The observational CO data is presented as the greyscale, with the red contours being a contour of the data at the 3σ, and 10σ levels. The blue contours overlaid are the best fit model contours, at the same levels as the data contours. The data in this image has been binned by a factor of 3 in velocity, simply for display purposes. The beam (4.26" x 4.16") is shown in the bottom left-hand corner of each channel.

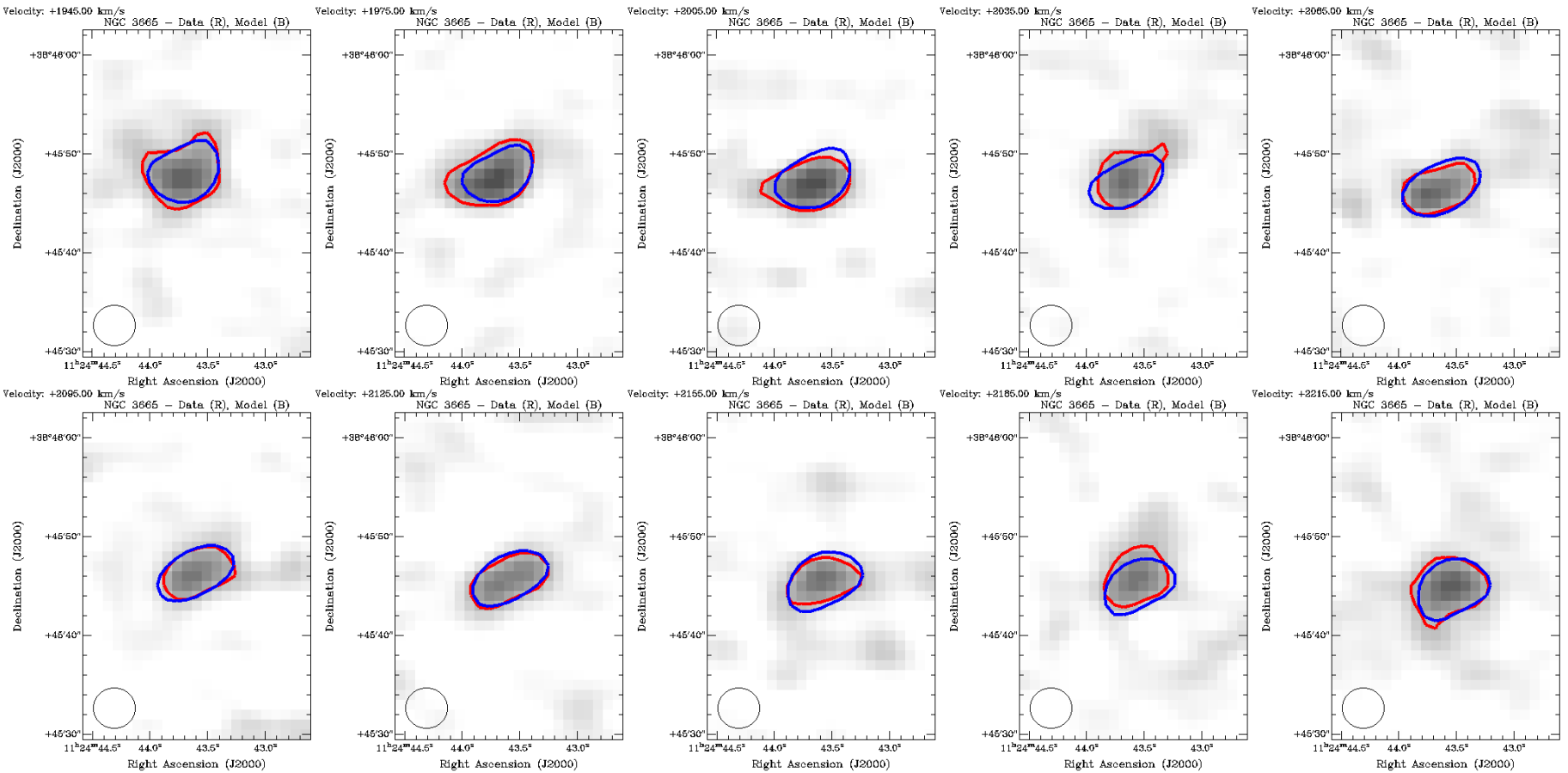

Figure 43: NGC 3665 Channel Map 2/3 - The middle 12 channels of the NGC 3665 channel map are shown, with the other 24 shown in Fig. 42 and Fig. 44. The observational CO data is presented as the greyscale, with the red contours being a contour of the data at the 3σ, and 10σ levels. The blue contours overlaid are the best fit model contours, at the same levels as the data contours. The data in this image has been binned by a factor of 3 in velocity, simply for display purposes. The beam (4.26" x 4.16") is shown in the bottom left-hand corner of each channel.

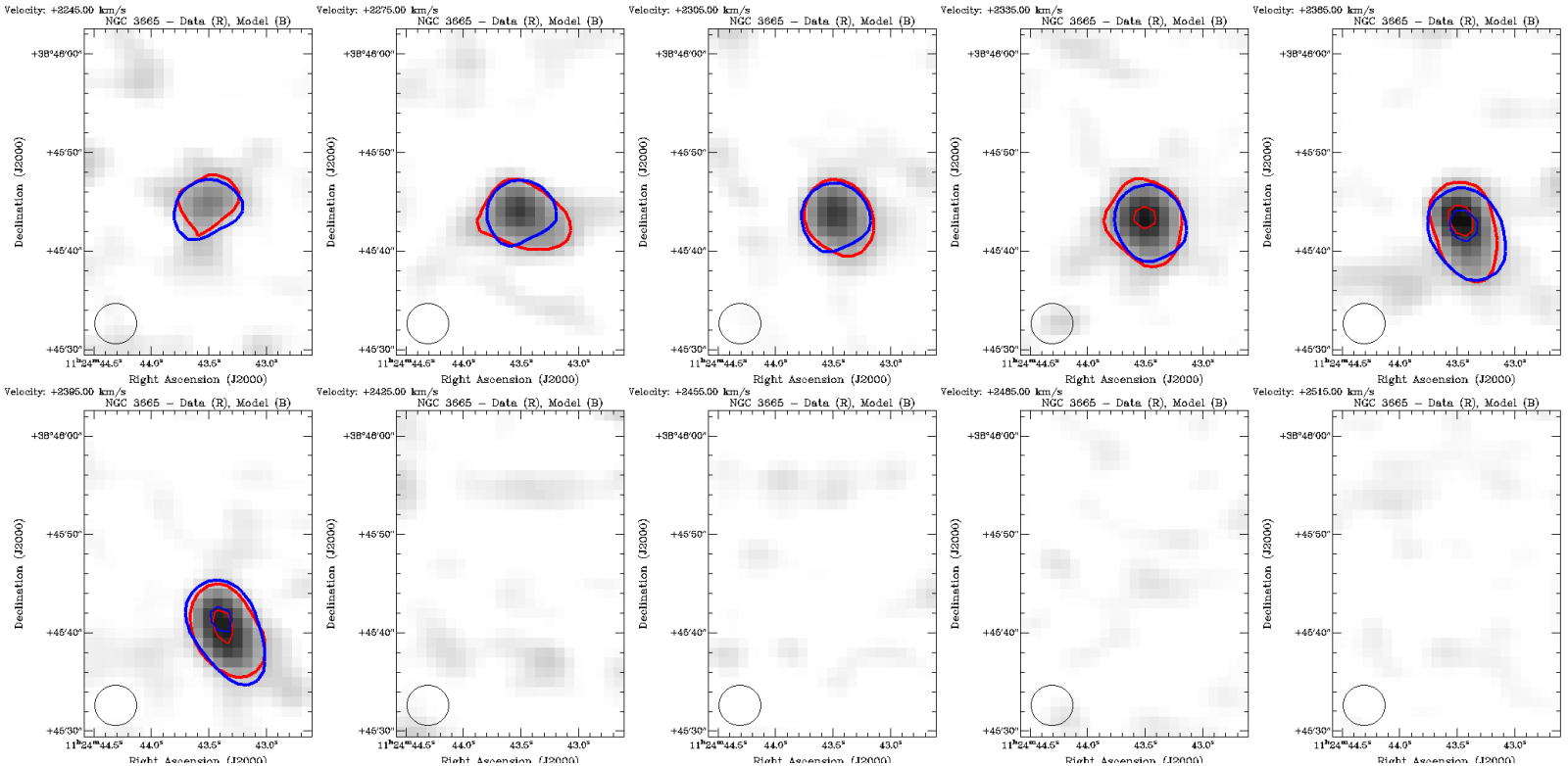

Figure 44: NGC 3665 Channel Map - The last 12 channels of the NGC 3665 channel map are shown, with the other 24 shown in Fig. 42 and Fig. 43. The observational CO data is presented as the greyscale, with the red contours being a contour of the data at the 3σ, and 10σ levels. The blue contours overlaid are the best fit model contours, at the same levels as the data contours. The data in this image has been binned by a factor of 3 in velocity, simply for display purposes. The beam (4.26" x 4.16") is shown in the bottom left-hand corner of each channel.

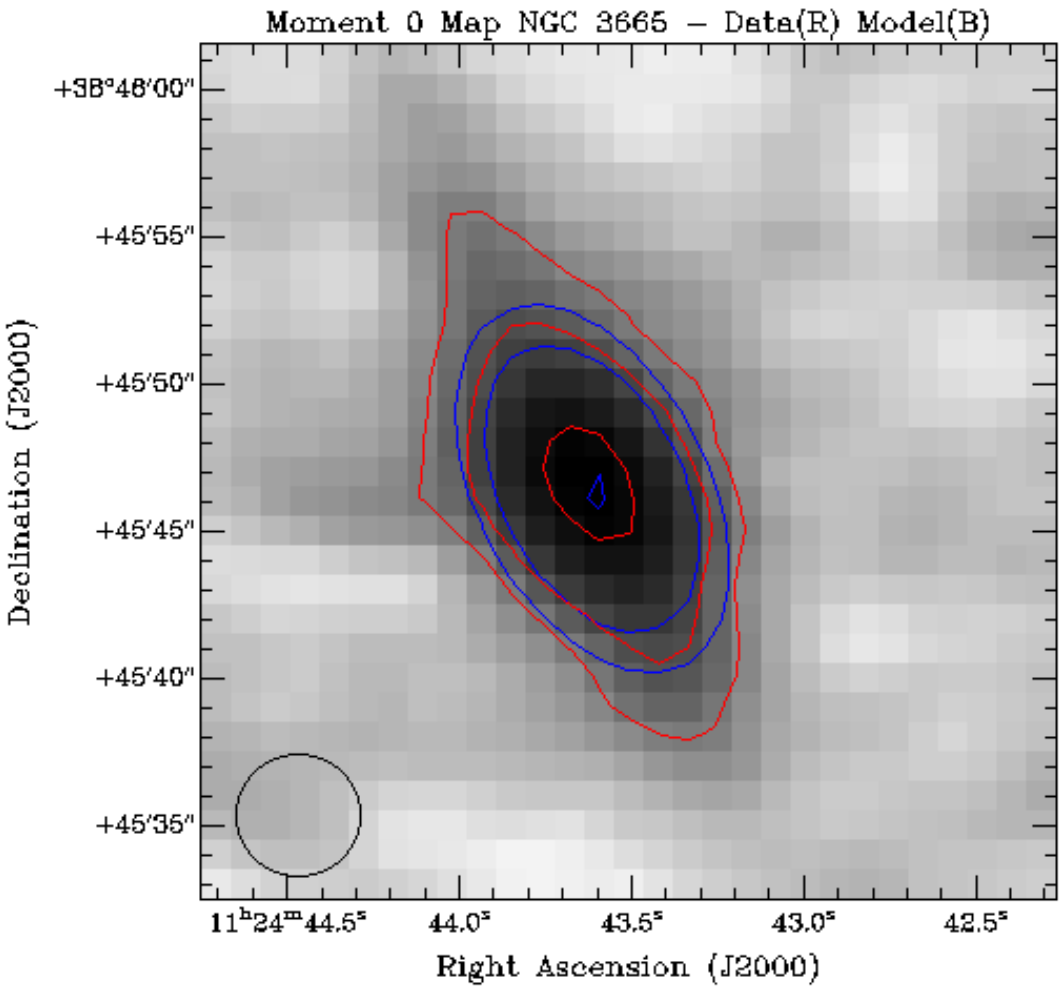

Figure 45: NGC 3665 Moment 0 Map - The observational CO data is presented as the greyscale, with the red contours being a contour of the data at the 2σ, 3σ, and 6σ levels. The blue contours overlaid are the best fit model contours, at the same levels as the data contours. For both moment maps, the full velocity range was used, and the lower clip level was set to 0.5σ. The beam (4.26" x 4.16") is shown in the bottom left-hand corner of each channel.

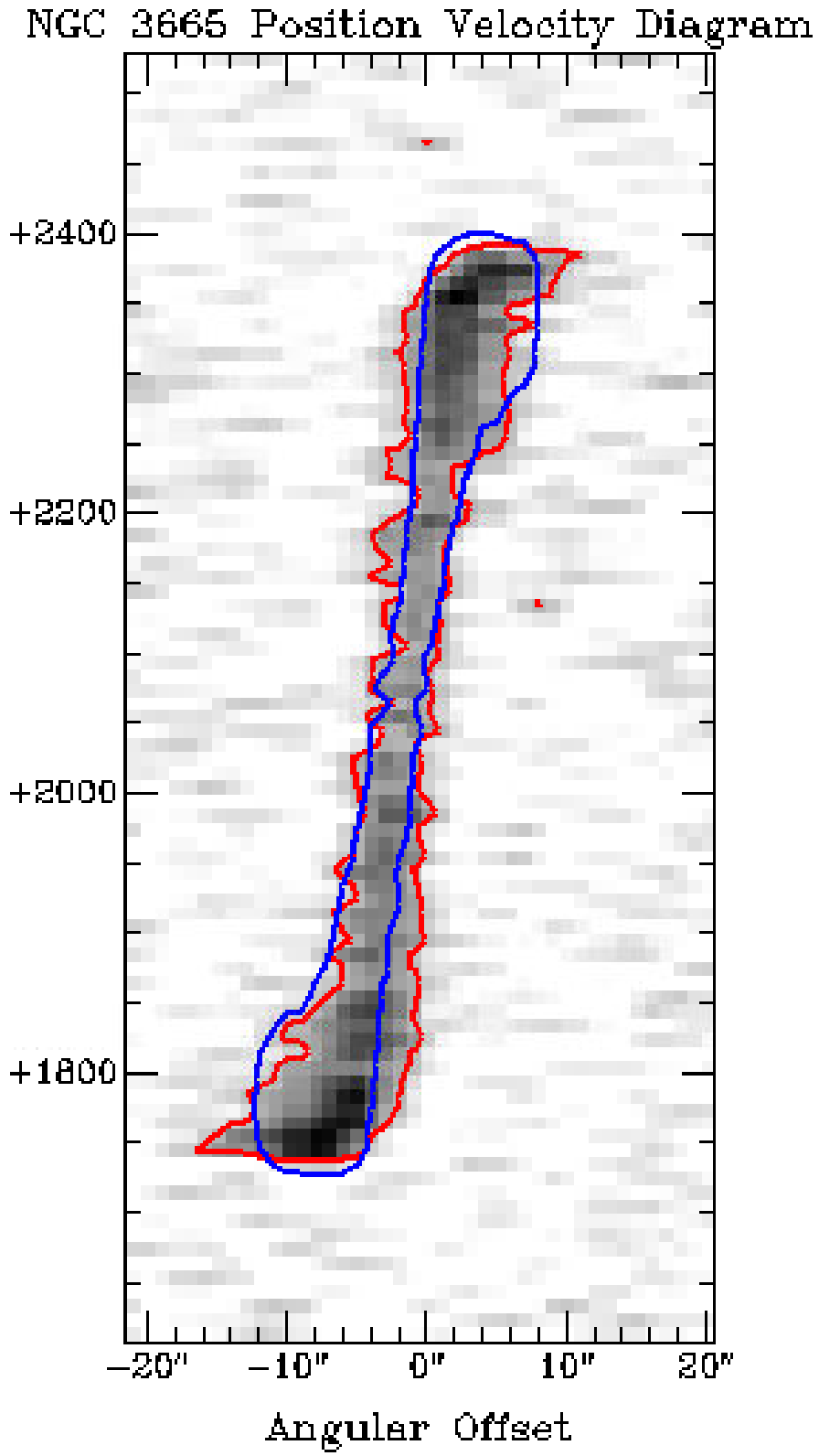

Figure 46: NGC 3665 Position-Velocity Diagram - The observational CO data is presented as the greyscale, with the red contour being a contour of the data at the 3σ level. The blue contour overlaid is the best fit model contour, at the same level as the data contour.

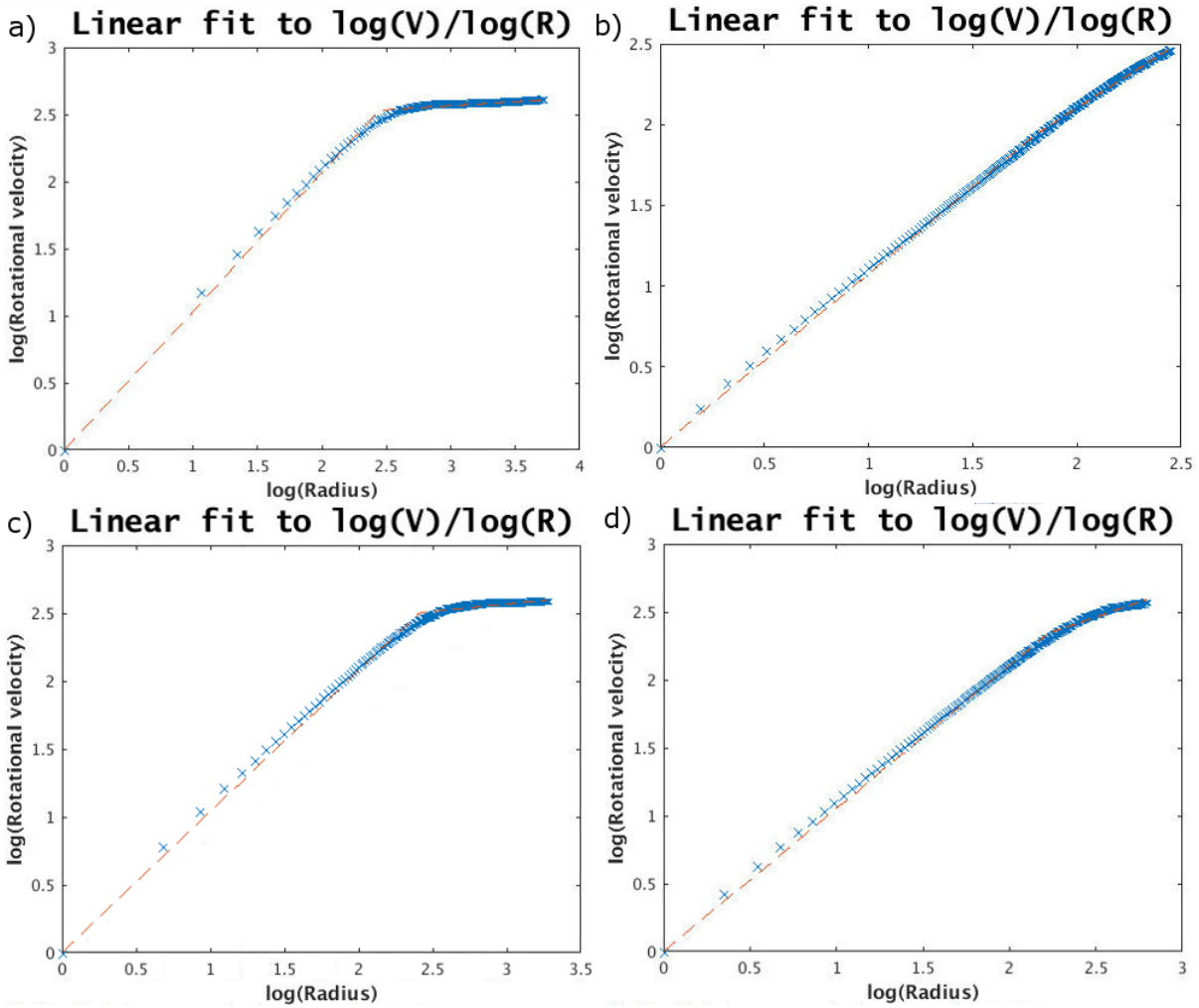

Figure 47: NGC 3665 curve fitting example. Both the radius (x-axis) and velocity (y-axis) are the logarithmic values. The "x" marks represent the data values, and the "-" represents the fit. The best-fit model was used for this example. Panel a) shows the log-log plot with $R = r_{mask}$. Panel b) shows the log-log plot with $R = r_{0v,best-fit}$. Panel c) shows the log-log plot with $R = r_{LastPoint}$. Panel d) shows the log-log plot with $R = R_e/8$. The fit values are found in Table 8, with M_1 being the slope of the inner rise, and M_2 being the slope after the apparent turnover in the curve.

6 Discussion

"*What's right is what's left if you do everything else wrong.*"

— Robin Williams

6.1 NGC 3198

The best-fit family of models produced by GalAPAGOS (see Section 1.6) were deemed to be moderately successful for NGC 3198 on "low" resolution and more successful "high" resolution data. This success is based on their low χ^2_ν, as well as their well-fitting position-velocity diagrams and moment 0 maps. The reason for initially modelling highly binned data for testing GalAPAGOS (see Section 3.2.1) was to test GalAPAGOS, in order to ensure that it was working properly. This test was successfully demonstrated that GalAPAGOS was in working order, and resulted in rotation curves, density plots, and position-velocity plots which were well matched with general expectations, and therefore the "high" resolution data could then be modelled.

Neither the "low" resolution nor "high" resolution models were successful in accurately reproducing the channel maps, in that the spatial discrepancy between the data and the model were larger than the beam size in a number of channels with data. We recall that the beam is the resolution element, and the largest spatial discrepancies were 11x the beam size for the "low" resolution model, and 20x the beam size for the "high" resolution model at the 3σ level. The general shape and morphology fit reasonably well on the large scale by the "high" resolution model, and less so by the "low" resolution model, despite the large discrepancies in the channel maps. This can be seen in the position-velocity diagram in Fig. 26 and spatially in channels in Fig. 31. The best-fit model ($\chi^2_\nu(Low\,res) = 1.987$, $\chi^2_\nu(High\,res) = 3.602$) was the model which was best matched morphologically to the data.

We compared the family of best-fit rotation curves to previous results [de Blok et al., 2008], and the results are shown in Fig. 48. The family of best-fit rotation curves were

exported using the GalAPAGOS visualization tools (see Section 1.7.4), and overlaid with previous results, de Blok et al. [2008], in order to directly compare the two.

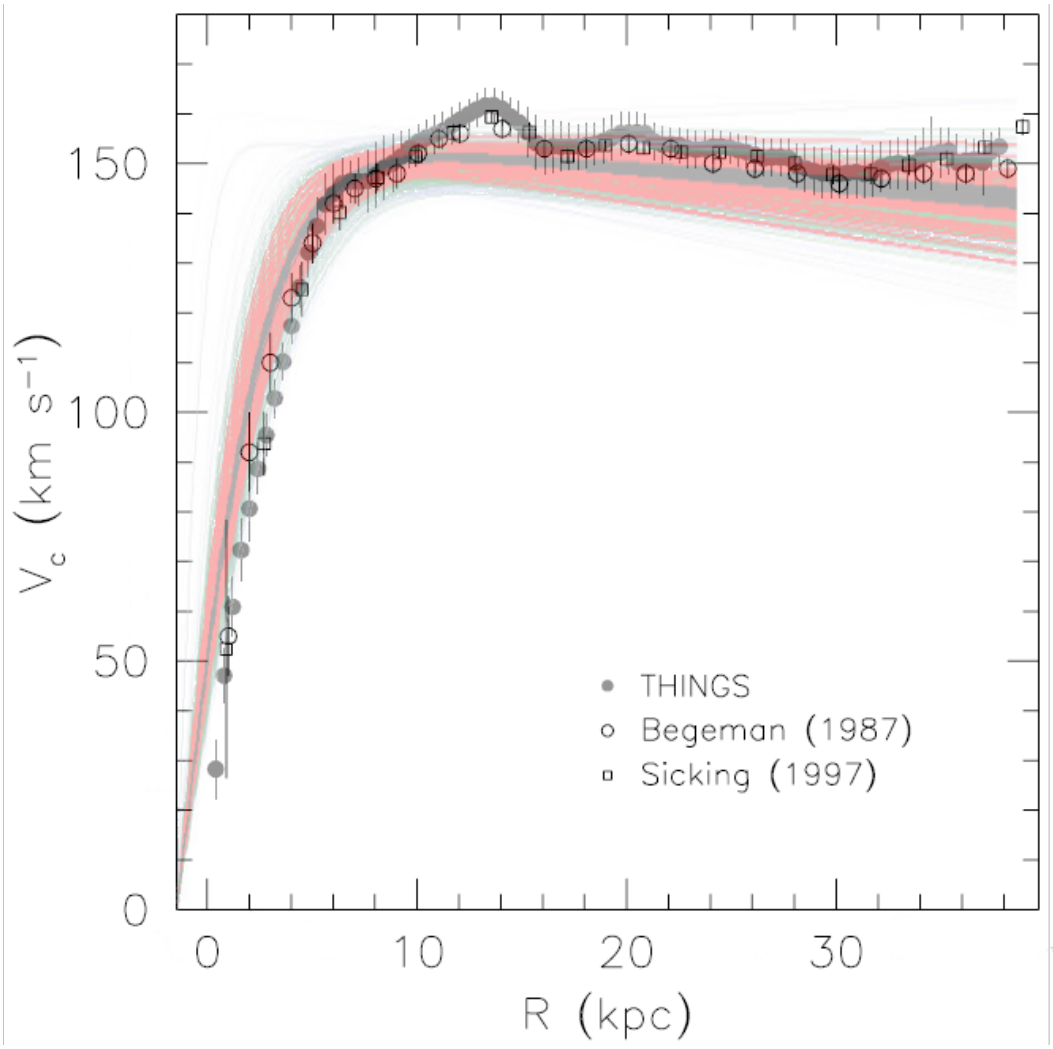

Figure 48: NGC 3198 Rotation Curve Comparison - The best-fit family of rotation curves produced by GalAPAGOS (dark gray (0 to 0.05σ level), red (0.05σ to 0.3σ level), green (0.3σ to 0.6σ level), and faint gray (0.6σ to 1σ level) solid line), see Section 5.1, is compared to that found by de Blok et al. [2008] (gray solid circles), Begeman [1987] (black open circles), and Sicking [1997] (black open squares).

Looking at Fig. 48, we can see that the best-fit family of rotation curves produced by GalAPAGOS using the "high" resolution data with the least binning match extremely well in the inner 10 kpc. However, they did not trace the hump occurring at 13 kpc. The velocity amplitude of our model ($v_{Gal}(R = 38.0) = 150 \pm 10$) and that found in Fig. 48 ($v_{literature}(R = 38.0) = 153 \pm 5$), do agree with each other within the error. Note that the lower resolution model has a velocity amplitude of $v_{Gal}(R = 38.0) = 140 \pm 20 km/s$

at a radius of 38.0 kpc, also agrees with the literature result. The rotation curves from GalAPAGOS flatten out at approximately 11 kpc, whereas those from the literature presented in Fig. 48 flatten at approximately 15.75 kpc, due to the presence of the hump at 13.5 kpc.

Note that our goal is not to reproduce each "bump and valley" in the data set, but rather to model a smooth disk; presuming galaxies have underlying diffuse gas disks. We then use the smooth model as a mask, allowing us to investigate the bumps and valleys that may be anomalies. In this case, the binned input and small number of SDMs resulted in us not tracing the hump, and also slightly underestimating the velocity. The model generated by GalAPAGOS for NGC 3198 is therefore a successful demonstration of GalAPAGOS' ability to find reasonable parameters within a broad parameter space.

The data cube for the "high" resolution data was twice the size of the "low" resolution data, and was also modelled using the same computer, named *Champion* (described in Appendix B), both using ten cores, leading to an opportunity to compare the length of time GalAPAGOS will use for a given data set size. The "low" resolution comprised of a data cube of size 61x81x36, which is 177,876 voxels, it went on for 128 generations, and took a total of 1.2 days. The "high" resolution run comprised of a data cube of size 121x161x72, which is 1,576,872 voxels, it went on for 148 generations, and took 8.0 days. From the dynamical mass calculation (Section 5.1), we can see that a user would be able to attain a rough estimate of the dynamical mass in approximately one day, however if more accurate results (particularly more accurate channel maps and rotation curves) are needed, the run time will increase to times greater than a week, in the current iteration of GalAPAGOS.

6.2 NGC 2188

The galaxy disk model produced by GalAPAGOS was generated using cropped, binned, and masked data (see Section 3.2.2 & 4.2.1). The data were masked after it was found that GalAPAGOS would attempt to model the extraplanar, (i.e. above the disk), gas to the east of NGC 2188 using an unrealistically large scale height. This gas is observed to be extraplanar in ionized H data in Domgorgen et al. [1996]. Using the masked data led to us only modelling the disk of the galaxy, although since there was less data to model, it also had the effect of reducing the computational time needed. However, since there were less data, there were also fewer resolution elements. After the masking, there were only four resolution elements across the galaxy. This led to large errors on the r_{0v} and SDM parameters.

We note that when the data were not masked, GalAPAGOS modelled NGC 2188 with a declining rotation curve $a_v \approx -0.9$ for the best fit model, meaning that the extraneous material had a velocity lower than the peak velocity amplitude. This could shed light on why some rotation curves for high redshift galaxies are observed to be declining [Genzel et al., 2017]. This means that rather than indicating an absence of DM, they could potentially be explained by inflow/outflow processes such as tidal interactions, ram pressure stripping, or a superbubble (see Section 1.3).

The galaxy disk model produced by GalAPAGOS was still reasonably successful, via the χ^2_ν criterion, with a χ^2_ν of 1.7143. In the channel maps (shown in Section 5.2), the maximum discrepancy in extent was minimal at the 3σ level. There is a total of only two channels where the discrepancy between the data and the model was at least the size of a beam, with the largest being 1.1x the beam size (47.63" x 28.33"). There is no discrepancy larger than the size of the beam in the moment zero map and the position velocity diagram.

NGC 2188 is challenging to model due to the extraplanar gas (shown in Fig. 49), which is not a component of the galaxy disk, and is found to the east of the galaxy disk. This extraneous gas caused problems, such as GalAPAGOS attempting to fit the extraneous

gas through a large scale height. The data were masked, allowing GalAPAGOS to only model the disk of the galaxy.

The model was then used as a spatial mask on the data, with anything outside of the mask taken to be an HI feature separate from the disk and considered extraplanar. The feature to the east of NGC 2188 was investigated with the disk emission decoupled. There have been two previously proposed causes for the extraplanar gas; tidal interactions, and ram pressure stripping (see Section 1.3). Tidal interactions have been suggested, for example, in Kirby et al. [2011]. However, this was solely due to the existence of material to the east of NGC 2188, and was proposed to have been due to interactions with AM0605-341 and ESO 364-G029 since they are nearby galaxies.

The strongest evidence for ram pressure stripping comes from the truncation of the HI gas radius [Kouwenhoven et al., 2007]. Typically, the HI disk extends approximately 1.5x the optical disk's radius, but in this case the stellar and gas disk radii are roughly equal to each other (see Section 4.2.1). Although this truncation might imply ram pressure stripping, there are no existing observations of X-ray gas currently available. Thus, hot gas streaming in to provide the source for ram pressure stripping in the group of galaxies surrounding NGC 2188 cannot be confirmed. The case for ram pressure stripping is also weakened by the kinematic behaviour of the eastern feature. Therefore, for the moment, we disregard ram pressure stripping as the source of this feature.

We propose that the east side feature seen in Section 5.2, is at least in part the result of an expanding shell (shown in Fig. 49 and in Fig. 50 an an expanding cylinder). These shells (see Section 1.3) are sometimes referred to as chimneys [Heiles, 1979], since broken shells can act as conduits for gas and radiation to escape from the disk into the halo (see Section 1.3). Looking at the renzogram contours of gas in the velocity range 718 - 806 km/s, we can see that there is a peak in the centre, highlighted in blue in Fig. 39, surrounded to the north and south by lower velocity features, highlighted in red. This higher velocity peak surrounded by lower velocity features is highly indicative of expansion as it would appear in a chimney, as shown in Fig. 50.

We recall from Section 1.3, that a chimney is the collimated structure formed by a superbubble bursting out from the galaxy disk. In observing a bursting superbubble, we are not observing the true velocity of each face of the bubble, as those are approximately equal. Rather we are seeing the projection of the velocity of each face onto our line of sight. That is the face travelling along the observer's line-of-sight has the highest velocity, with the velocity decreasing as we travel outward along the bubble, due to the angle between the velocity of that face relative to our line-of-sight increasing, until eventually we reach the face perpendicular to the observer's line-of-sight, which is observed to have no velocity along the observer's line-of-sight.

There is also the existence of an HII region, roughly centered on the higher velocity peak of this chimney feature, at R.A. 6h 10m 10s , Dec. -34d 07m 2s, as seen in Fig. 16. The combination of these two pieces of evidence leads to a strong case for this being an internal blowout feature.

We note that it is still possible that these effects contribute in some form to the overall morphology of NGC 2188, although it is unlikely to be primarily caused by tidal interactions and ram pressure stripping.

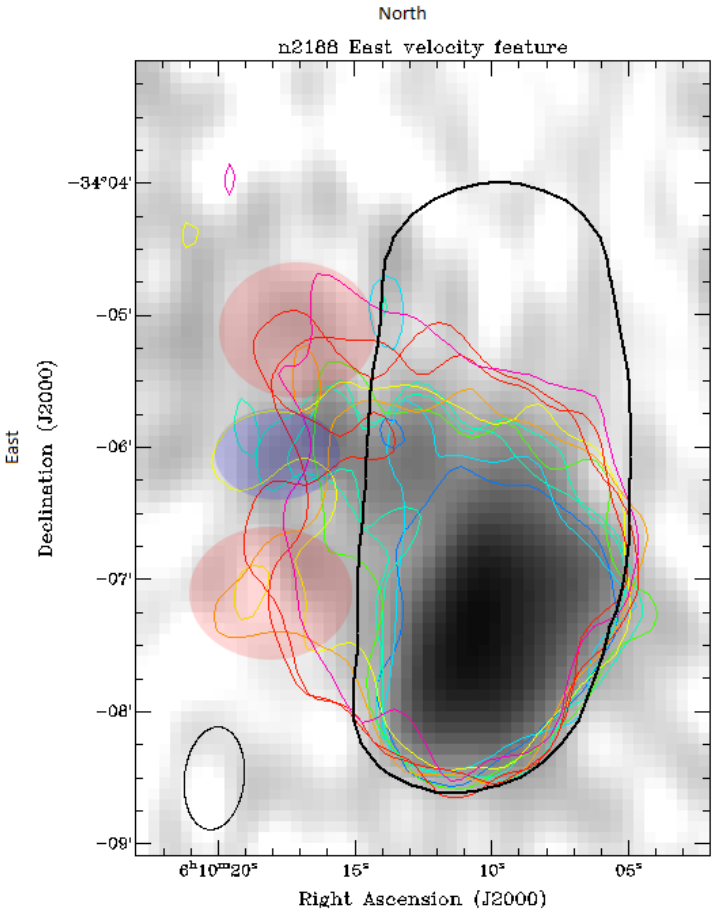

Figure 49: NGC 2188 Renzogram Figure - The greyscale background is the unbinned NGC 2188 data (Section 3.2.2), and the coloured renzogram (described in Section 5.2) contours are at the 4σ level of the data. Here we only plot channels 10-21. The black ring represents the extent of the model, which is taken to be the extent of the HI disk of the galaxy. The feature to the east of this disk is highlighted via the blue and red ellipses along with the renzogram contours. It can be observed in the renzogram contours that there is a lower velocity (red) feature to the north and south of the higher velocity (blue) feature.

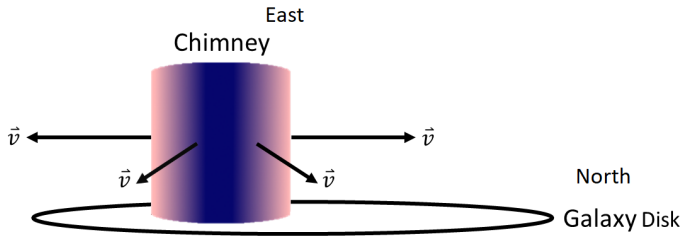

Figure 50: A schematic representation of the chimney found in NGC 2188. This is representative of a nearly edge on view of NGC 2188, with the chimney protruding to the east, from the southern face of the galaxy. The blue indicates that the velocity from the expanding bubble is aligned with the observer's line-of-sight, with the light red at the edges indicating that the velocity from the expanding bubble is perpendicular to the observer's line of sight. The blue in the center of the chimney roughly corresponds to the blue highlighted region in Fig. 49, as well as the red on the edges of the chimney roughly corresponding to the red highlighted regions in Fig. 49.

6.3 NGC 3665

Quantitatively, we can say that the morphology of the best-fit model matched very well to that of the galaxy in the channel maps, with the spatial difference between the data and the model being less than the beam size (4.26" x 4.16") everywhere (see Fig. 42 - Fig. 44). The position-velocity diagram produced from the model also matched well with the data, with the difference in position again being less than the size of the beam everywhere. The statistical measurement of how well the model fit the data was also excellent, with a χ^2_ν of 0.9973. Therefore, by all of the metrics we have to measure the quality of a model, the model for the early-type galaxy NGC 3665 was excellent.

We use the results from doing the linear fit to the so-called logarithmic rotation curve, (results listed in Table 8), in an attempt to determine whether the DM distribution consists of a core or a cusp (see Section 5.3). We note that when this is done, it implies that the rotation curve, which is due to the total matter, consists of luminous and DM in the inner disk. These results therefore do not represent a decomposition of the rotation curve into its different components (such as the gas disk, stellar distribution, and then the inner region of the DM halo), and then performing the analysis on solely the DM component. It should also be noted that with a beam size of approximately 700 pc, we are measuring outside the black hole's sphere of influence, which is approximately 30 pc, or 0.2" [Onishi et al., 2017a].

Other models (such as presented in Onishi et al. [2017a]) assume that all of the kinematics in the inner disk describe only the luminous matter along with the central black hole. We instead assume the kinematics mainly trace the DM halo. Obviously, there is luminous matter; however, this exercise sets a constraint on the DM halo's kinematic profile, in regard to the core/cusp problem (see Section 1.4). This is a valid exploration since this is a recently revitalized field, driven by new technology giving us high resolution data. There does not currently exist a widely accepted technique for decomposing mass components in the inner disk of early-type galaxies, which would allow the tracing of only the DM halo. It should also be noted that there is no consensus on the radius in which the "inner"

disk of the galaxy is confined to, and this work is therefore highly relevant to the current discussion on this subject. The limiting factor in terms of determining the inner radius of NGC 3665 is the relatively small ($r = 1.926$kpc) extent of the CO data.

The CARMA data used in Onishi et al. [2017a] was made available for this project, and had a much higher resolution (beam size $\approx$ 0.6") than the data used to generate the models presented. However, the data were not sufficiently contiguous, and GalAPAGOS could not successfully generate a reasonable model. We ran GalAPAGOS using the updated SDM equation (Eq. 2.6), and using both the regular fitness function, and using the moment map fitness function; both were unsuccessful.

From Table 8, we can see that the slope found for the inner rise of the logarithmic rotation curve is 1.0 ± 0.2. A slope of 1 indicates that the velocity rise in the inner part of the rotation curve is linear with the radius, as occurs with a core, and a slope of 0.5 indicates that the rise in the rotation curve goes as the square root of the radius, as occurs with a cusp. These results therefore indicate that, if we are tracing the DM distribution in NGC 3665, has a core, rather than a cusp.

The total dynamical mass inside a radius of 1.926 kpc was found to be $M_{tot}\,(R = 1.93kpc) = [6 \pm 2] \times 10^{10}\mathrm{M}_{\odot}$. The WISDOM paper [Onishi et al., 2017a] investigating the black hole in NGC 3665 estimates that $5.8 \times 10^{8} M_{\odot}$ is associated with the black hole, and assumed that the remaining $5.9 \times 10^{10} M_{\odot}$ is associated with stars.

6.4 NGC 1097

NGC 1097 has not been included in the data or results section, since GalAPAGOS was unsuccessful in producing a useable model. The model generated was unable to reproduce the majority of morphological features, such as the ring surrounding the inner data (see Fig. 51). The data used for NGC 1097 was HCN molecular gas data, taken as part of the Atlas3D survey. It has a high resolution, with a beam size of 2.2" x 1.58". The data was not limited by its resolution; however, it was not contiguous, (as shown in Fig. 51),

which is the primary reason GalAPAGOS could not generate a successful model, as with the high resolution CARMA data of NGC 3665.

Initially, GalAPAGOS was run using 6 SDM parameters, and eventually GalAPAGOS was run with 8 SDM parameters. This was done in an attempt to use the additional SDM parameters to fit the gaps in the HCN data. It was determined that the data were not sufficiently contiguous for GalAPAGOS to generate a reasonable model after a number of other attempts with various configurations of GalAPAGOS. A solution could possibly be to use moment maps for the fitness, as described in Section 2.5. This approach has been unsuccessful as of the time of writing this thesis.

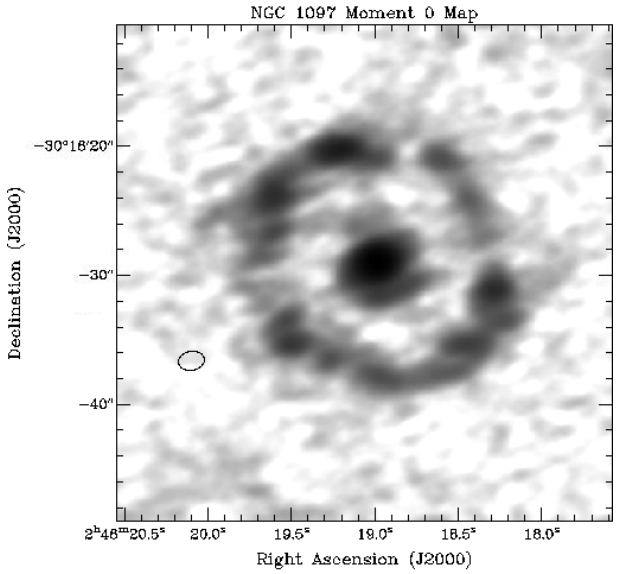

Figure 51: Moment 0 Map of NGC 1097. It is clear that there is a gap in the data between the outer and the inner rings, where there is only noise. The full velocity range was used, and the lower clip level was set to 0.5σ.

7 Conclusion

"I seldom end up where I wanted to go, but almost always end up where I need to be."

— Douglas Adams

The goal of modelling the kinematics of cold gas in galaxies using GalAPAGOS was achieved through a number of avenues. The robustness of the modelling capabilities was tested using artificial galaxies. There were successful models produced for NGC 2188 (Peculiar galaxy), as well as NGC 3198 (Spiral galaxy), and NGC 3665 (Elliptical galaxy). GalAPAGOS was unsuccessful in producing a useable model of NGC 1097 due to the data being noncontiguous. The results of the analysis performed on these models are presented in Section 7.2.

7.1 State of GalAPAGOS

It has been shown that GalAPAGOS has been very successful at modelling artificial galaxies. It was also successful at modelling the carbon monoxide data cube of NGC 3665, and to a lesser degree, the HI spectral line data cubes of NGC 2188 and NGC 3198. Note that in all cases, the initial parameter values had no impact on the success of a run, since they are randomly distributed throughout the search range of the parameter. Although there has been much progress made in terms of fixing and improving the code, there are still a number of issues to address, such as:

- Weighting of the fitness function in the center of the galaxy (see Section 2.5);
- Using the moment 0 and moment 1 maps to measure the fitness, rather than comparing the intensities throughout the cube;
- Fixing the visualization issues within GalAPAGOS, with the main issue being how the model is overlaid on the data in viewSolutions;
- Rewriting the Java section of the code using C to fix the Java heap space issue, as

well as improve efficiency.

The first item may help with the discrepancy of a poor morphological fit of a model to data when there is a good χ^2_ν value. Weighting the fitness function such that the center of the galaxy is weighted more heavily than the outer regions, which are mainly noise, is one proposal to mitigate the impact of measuring χ^2_ν in many noisy pixels, and potentially improve the fitness of the model in the central regions of the galaxy. Using the moment 0 and moment 1 maps to measure the fitness (see Section 2.5) would be another way to mitigate the noise, since the noise has both positive and negative values, which tend to cancel out with each other as we sum over the cube, while the target voxels, having only positive values, sums with itself. Using the moment 0 and 1 maps could also possibly be a way for GalAPAGOS to handle non-contiguous data, such as the HCN cubes in Section 6.4 more easily. The visualization problems are a coding issue, which can be solved by fixing the visualization codes. The primary issue is that the model has a 90° offset to the data when the model is overlaid on the data in vieweSolutions. Lastly, the Java heap space issue can be addressed by rewriting the Java sections in C. C is also more efficient than Java, which would further reduce run times. Python would be another option, as it is widespread in the astronomy community, although C is still faster.

7.2 Science Results

The branch of GalAPAGOS used to model NGC 3198 was the optically thin, sparse, non-Java code (branch 6 in Fig. 8). GalAPAGOS was moderately successful at modelling the data. The "low" resolution channel maps of NGC 3198 were not well-matched, although there was an improvement with the "high" resolution channel maps. Despite this improvement, the channel maps were still unsuccessful, considering that all channels with data present had a discrepancy between the data and the model which was at least the size of a beam, with the largest being 20x the beam size (11.43" x 9.26"). The rotation curves generated by the GalAPAGOS models matched extremely well with those previously found in de Blok et al. [2008], Begeman [1987], and Sicking [1997] inside 10 kpc, and

again improved when $r > 15.5kpc$, However, by design, did not find the spike in velocity which occurs at 13 kpc. GalAPAGOS found a velocity amplitude of $150 \pm 10km/s$ at 38.0 kpc, compared to $153 \pm 5km/s$ at a radius of 38.0 kpc from de Blok et al. [2008]. Using the rotation curve, shown in Fig. 21, the total dynamical mass inside a radius of 38.0 kpc was found to be $M_{tot}(Gal)\,(R = 38.0kpc) = [2.0 \pm 0.1] \times 10^{11}\,\mathrm{M}_{\odot}$, compared to that found in de Blok et al. [2008] of $M_{tot}(THINGS)\,(R = 38.0kpc) = [2.07 \pm 0.06] \times 10^{11}\,\mathrm{M}_{\odot}$.

The branch of GalAPAGOS used to model NGC 2188 was the non-optically thin, sparse, Java code (branch 7 in Fig. 8). GalAPAGOS used unbinned data masked below the 5σ level of the data noise to model the disk of NGC 2188. The data were masked (see Section 4.2.1) due to GalAPAGOS modelling the extraplanar, non-disk material to the east of NGC 2188 using an unrealistically large scale height. GalAPAGOS was moderately successful at modelling the HI disk of NGC 2188, and the lowest χ^2_ν model was then used as a guideline to indicate the vertical extent of the disk of NGC 2188. This permitted the investigation of the anomalous gas outside of the galaxy disk, which does not have the same velocities as the rotating disk.

The previously proposed solutions for the extraplanar gas was tidal stretching due to gravitational interaction between NGC 2188, AM0605-341, and ESO 364-G029 [Kirby et al., 2011], and ram pressure stripping [Kouwenhoven et al., 2007]. This solution was discussed in Section 6.2, and these processes do not dominate due to the kinematic behaviour of this particular extraplanar material. The velocity structure shown in Fig. 39 is consistent with an expanding shell, or "chimney" (see Section 1.3 and Section 6.2). We note that this outflow could be occurring along with some tidal interaction and ram pressure stripping throughout the galaxy. However, our conclusion of an expanding shell could provide further explanation of features usually associated with tidal interaction and ram pressure stripping.

Another use for the model is to measure the dynamical mass within the disk. The total dynamical mass inside a radius of 4.52 kpc (disk radius) was found to be $M_{tot}\,(R = 4.52kpc) = [8 \pm 4] \times 10^9 \mathrm{M}_{\odot}$ using the rotation curves shown in Fig. 32.

GalAPAGOS was remarkably successful at modelling the CO disk in the center of the early-type galaxy NGC 3665, with an excellent χ^2_ν of 0.9973. We set a constraint on the cuspiness of the DM distribution in the nucleus of NGC 3665, although performing a mass decomposition on the modelled rotation curve is beyond the scope of this thesis. This exploration was worth doing since there is no standard procedure nor agreement on the definition of the "inner" radius of a galaxy.

We found that the slope of the logarithmic rotation curve was 1.0 ± 0.2, indicating the presence of a flat core, rather than a cusp, for the total mass distribution. If we assume that this distribution traces the DM distribution, then the halo centre would also not be cuspy. The total dynamical mass inside a radius of 1.926 kpc was found to be $M_{tot}\,(R = 1.93kpc) = [6 \pm 2] \times 10^{10}\mathrm{M}_\odot$. For comparison, the WISDOM paper [Onishi et al., 2017a] investigating the black hole in NGC 3665 estimates that $5.8 \times 10^8 M_\odot$ is associated with the black hole, and assume the remaining $5.9 \times 10^{10} M_\odot$ is associated with stars.

7.3 Future Work

For NGC 3198, future work could include following the technique used for analysis on NGC 2188; that is using the model as a mask and looking for anomalies. Other work could include modelling the unbinned NGC 3198 data, after the code has been rewritten using C rather than Java, as the unbinned data are too large to be run using Java, due to the Java heap space available in MATLAB (see Section 3.2.1).

NGC 2188 has a clear path for future work, which would include using higher resolution data (possibly from SKA) as it becomes available to better analyze the extraplanar gas found to the east of the galaxy's disk. This would provide more information allowing us to further disentangle the effects of cold inflow along the large scale structure, tidal components, ram pressure stripping, along with those found from the expanding shell (chimney).

Future work for NGC 3665 should include performing a mass decomposition, which would require the stellar component in order to then isolate the DM halo. This would then allow us to apply the fitting procedures performed in Section 5.3 on the DM halo component, and thus allow for a more accurate study of the core/cusp investigation. Other work would include attempting to model the higher resolution CARMA data after the aforementioned improvements to GalAPAGOS have been completed.

Other future work could include applying GalAPAGOS to more galaxies which have both HI and CO data available for their inner regions and dynamical stellar component studies, to further investigate the core/cusp problem in DM haloes alone. Another avenue would include studies of spiral galaxies using CO data in conjunction with HI to construct a model with highly constrained inner kinematics due to the CO, and accurately modelled outer kinematics as a result of the HI. This combination of CO and HI data would be the epitome of GalAPAGOS' capabilities, and would lead to highly accurate rotation curves and kinematics, resulting in the opportunity to find intriguing kinematic anomalies in galaxies. This could lead to insights in terms of galaxy formation and evolution; such as measuring the DM halo properties to constrain cosmological models (galaxy formation), and investigating anomalous gas in galaxies to highlight inflow and outflow processes (galaxy evolution).

A Testing of Artificial Galaxies

Listed in Tables 9, 10 are some of the results found indicating that the parameters were recovered extremely well for a number of artificial galaxies. The intensities of the model galaxies are trustworthy, since the discrepancy between the intensity of the input artificial galaxy and the output model were negligible as can be seen in Table 12. The morphology is believed to be accurate as demonstrated by the contour plots. The contours shown on the artificial galaxies by the models are indistinguishable. Some examples are shown in Figures 52 through 57.

The following figures (Fig. 52 through Fig. 57) are composite images of four different measurements of the extent to which the modelling was successful for the searches done with a varying number of SDMs. The top-left panel, panel a), is the rotation curve for the input artificial galaxy, which is shown in as the dashed line in red, along with the model's rotation curve, which is shown as the solid blue line. The vertical line is representative of the asymptotic velocity v_0, at the location of r_{0v}, which is the scaling factor to control the position of the turnover radius. The top-right panel, panel b), is the HI density profile for the input artificial galaxy, shown as the red dashed line, and for the model, which is shown as the solid blue line. The bottom-left panel, panel c), displays the velocity channel, in which there was the largest discrepancy between the input artificial galaxy, which is displayed as the greyscale data, and the model, which is shown as the red contour. The lowest contour starts at 3σ estimated from the noise of the input cube, and is taken at the same level when there is no noise. The contours then increase by 20% of the maximum intensity in each step. The beam can also be seen in the bottom left of the image, and has a size of 30 arcseconds. The bottom-right panel, panel d), shows a moment 0 map of the input artificial galaxy as the greyscale data, with the model moment 0 map shown as the red contours on top of the greyscale. The contours again begin at 3σ of the estimated noise and increase by 20% of the maximum intensity in each step.

art3198-b			
Parameter	Artificial Galaxy Value	Recovered Model Value	Percent Error
Fitness	N/A	8.81×10^{-12}	N/A
$r_{Out}\,(arcsec)$	450	450.0036	0.0008
$v_0\,(km/s)$	155	155.0000079	5.097×10^{-6}
a_v	0.2	0.2	0
$N_{H,0}\,m^{-2}$	1×10^{25}	1×10^{25}	0
$T_s\,(K)$	100	99.9999	0.0001
$r_{0v}\,(arcsec)$	120	120.0009	0.00075
$H\,(arcsec)$	30	30.0003	0.001
$v_\sigma\,(km/s)$	15	15.0000192	0.000128
$v_{cm}\,(km/s)$	690	689.9999999	1.45×10^{-8}
$dr_{Out}\,(arcsec)$	11	11.0003	0.0027
$inc\,(rad)$	1.26	1.2566	0.0029
$PA\,(rad)$	0.63	0.62832	0.00023
$xShift\,(arcsec)$	0	0	0
$yShift\,(arcsec)$	0	0	0
$iWarp0\,(rad)$	N/A	N/A	N/A
$phiWarp0\,(rad)$	N/A	N/A	N/A
$iWarp1\,(rad)$	N/A	N/A	N/A
$phiWarp1\,(rad)$	N/A	N/A	N/A
$maxTwistWarp\,(rad)$	N/A	N/A	N/A
$SDM1$	-0.6	-0.40477	32.54
$SDM2$	0.4	0.747	86.8
$SDM3$	0	-0.434	N/A
$SDM4$	-0.7	0.44	162.9
$SDM5$	0.1	0.66	563
$SDM6$	0.5	0.739	47.8
		Average Error	7.2×10^{-4}

Table 9: The parameters used to create the artificial galaxy is shown under "Artificial Galaxy Value", and the parameter values used for the model are shown in "Recovered Model Value". The beam size for this artificial galaxy was 30 arcseconds. These results were for an artificial galaxy with the parameters being based off of the best guess values for NGC 3198 with the warp off, and SDMs on. GalAPAGOS was run on the non-optically thin version, with 11 CPU cores. The average error was calculated ignoring the SDMs, since they are not expected to be recovered.

art2188			
Parameter	Artificial Galaxy Value	Recovered Model Value	Percent Error
Fitness	N/A	4.66×10^{-6}	N/A
$r_{Out}\,(arcsec)$	110	109.97	0.025
$v_0\,(km/s)$	70	69.9927	0.01
a_v	0.2	0.20286	1.43
$N_{H,0}\,m^{-2}$	1×10^{25}	1×10^{25}	0
$T_s\,(K)$	100	99.4086	0.5914
$r_{0v}\,(arcsec)$	60	59.8668	0.222
$H\,(arcsec)$	26	25.9971	0.0112
$v_\sigma\,(km/s)$	15	14.995	0.0301
$v_{cm}\,(km/s)$	747	746.999	1.82×10^{-4}
$dr_{Out}\,(arcsec)$	1	1.2003	20.03
$inc\,(rad)$	1.52	1.5281	0.6364
$PA\,(rad)$	0	0.0014721	N/A
$xShift\,(arcsec)$	0	-0.0035	N/A
$yShift\,(arcsec)$	0	-0.0135	N/A
$iWarp0\,(rad)$	0.17	0.18052	3.43
$phiWarp0\,(rad)$	0.79	0.84325	7.37
$iWarp1\,(rad)$	0.17	0.17464	2.73
$phiWarp1\,(rad)$	0.79	1.0068	27.443
$maxTwistWarp\,(rad)$	0.79	0.5236	33.722
$SDM1$	-0.6	0.20365	133.94
$SDM2$	0.4	0.98533	146.33
$SDM3$	0	-0.858	N/A
$SDM4$	-0.7	-0.95522	36.46
$SDM5$	0.1	0.186	85.58
$SDM6$	0.5	0.03	93.96
		Average Error	6.1

Table 10: The parameters used to create the artificial galaxy is shown under "Artificial Galaxy Value", and the parameter values used for the model are shown in "Recovered Model Value". The beam size for this artificial galaxy was 30 arcseconds. These results were for an artificial galaxy with the parameters being based off of the best guess values for NGC 2188 with the warp on, and SDMs on. GalAPAGOS was run on the non-optically thin version, with 11 CPU cores. The average error was calculated ignoring the SDMs, since they are not expected to be recovered.

art3198-c			
Parameter	Artificial Galaxy Value	Recovered Model Value	Percent Error
Fitness	N/A	8.61×10^{-7}	N/A
$r_{Out}\,(arcsec)$	450	450.1555	0.0346
$v_0\,(km/s)$	155	155.0323	0.021
a_v	0.2	0.19851	0.745
$N_{H,0}\,m^{-2}$	1×10^{25}	3.33×10^{23}	96.673
$T_s\,(K)$	100	3.367	96.633
$r_{0v}\,(arcsec)$	120	120.6147	0.512
$H\,(arcsec)$	30	29.9797	0.0677
$v_\sigma\,(km/s)$	15	15.0187	0.125
$v_{cm}\,(km/s)$	690	690.088	0.0128
$dr_{Out}\,(arcsec)$	11	11.1366	1.24
$inc\,(rad)$	1.26	1.2735	1.342
$PA\,(rad)$	0.63	0.63172	0541
$xShift\,(arcsec)$	0	0.323	N/A
$yShift\,(arcsec)$	0	-0.204	N/A
$iWarp0\,(rad)$	0.17	0.18427	5.579
$phiWarp0\,(rad)$	0.79	0.883	12.439
$iWarp1\,(rad)$	0.17	0.176	3.529
$phiWarp1\,(rad)$	0.79	1.0097	27.81
$maxTwistWarp\,(rad)$	0.79	0.5236	33.72
		Average Error	7.2×10^{-4}

Table 11: The parameters used to create the artificial galaxy is shown under "Artificial Galaxy Value", and the parameter values used for the model are shown in "Recovered Model Value". The beam size for this artificial galaxy was 30 arcseconds. These results were for an artificial galaxy with the parameters being based off of the best guess values for NGC 3198 with the warp on and no SDMs searched for. GalAPAGOS was run on the non-optically thin version, with 11 CPU cores. The average error was calculated using the observable parameters.

NGC 2188 Pars.	Velocity [km/s]	# of points	Mean $\left[\frac{\mu Jy}{Beam}\right]$	Std. Dev.
Artificial Galaxy	817.02 (a)	2500	337.901	1777.57
	770.34 (b)	2500	846.763	4389.68
	723.67 (c)	2500	854.078	4401.45
	677.02 (d)	2500	346.785	1809.48
Model	817.02 (a)	2500	337.688	1777.46
	770.34 (b)	2500	847.058	4389.95
	723.67 (c)	2500	854.184	4400.89
	677.02 (d)	2500	346.665	1809.27

NGC 2188 Pars.	Velocity [km/s]	Min. $\left[\frac{\mu Jy}{Beam}\right]$	Max. $\left[\frac{\mu Jy}{Beam}\right]$	Sum $\left[\frac{\mu Jy}{Beam}\right]$	Total flux [mJy]
Artificial Galaxy	817.02 (a)	0	18891	844752	82.84
	770.34 (b)	0	47178.3	2.12×10^6	207.59
	723.67 (c)	0	47013.1	2.14×10^6	209.38
	677.02 (d)	0	19055.1	866962	85.02
Model	817.02 (a)	0	18901.8	844219	82.79
	770.34 (b)	0	47182	2.12×10^6	207.66
	723.67 (c)	0	47015.7	2.14×10^6	209.41
	677.02 (d)	0	19044.1	866662	84.99

Table 12: The top four rows have intensity values for the input artificial galaxy (art2188) for different velocity channels. These can be compared with the next four rows with intensity values for the output model for the same velocity channels. a) 817.02 km/s. b) 770.34 km/s. c) 723.67 km/s. d) 677.02 km/s. Column 2 lists the velocity channel we are examining. Column 3 lists the number of points used in our sample region. Column 4 lists the mean intensity of the sample region. Column 5 lists the standard deviation of that intensity. Column 8 lists the minimum intensity. Column 9 lists the maximum intensity. Column 10 lists the sum of intensities. Column 11 lists the total flux of the sample region.

	Artificial Galaxy	Optically Thin/Non-Thin	Noise	Warp	Fitness	Avg. % error
1	3198	Non-Thin	No Noise	Off	0.729	1.45
2	2188	Non-Thin	No Noise	On	0.2784	15.7
3	2188	Non-Thin	Noise	Off	1.2695	10.8
4	3198	Non-Thin	Noise	On	1.0765	9.19
5	3198	Thin	No Noise	Off	0.651	8.674
6	3198	Thin	No Noise	On	0.465	6.389
7	3198	Thin	Noise	Off	2.404	12.9
8	2188	Thin	Noise	On	1.0765	9.19

Table 13: Results of testing without the SDMs being searched for. In this case the SDMs were all set to equal one. The ranges searched for all other parameters were identical, with the only difference being whether or not the artificial galaxy was created with or without noise.

	Artificial Galaxy	Optically Thin/Non-Thin	Noise	Warp	# of SDMs searched for	Fitness	Avg. % error
1	art3198-d	Non	No Noise	On	0	8.61×10^{-7}	0.3779
2	art3198-d	Non	Noise	On	0	0.94892	0.451
3	art2188	Non	No Noise	On	0	4.66×10^{-6}	0.274
4	art3198-d	Non	Noise	On	4	1.3692	2.694
5	art3198-d	Non	No Noise	On	5	0.066625	3.143
6	art3198-d	Non	Noise	On	5	1.1041	2.704
7	art3198-d	Non	No Noise	On	6	3.09×10^{-4}	0.398
8	art3198-d	Thin	No Noise	On	6	0.00263	1.798
9	art3198-d	Thin	Noise	On	6	0.93358	0.5426
10	art3198-d	Non	Noise	On	6	0.96551	0.6462
11	art3198-d	Non	Noise	On	8	0.93363	0.457

Table 14: Results of testing with the SDMs being searched for. Column 6 lists the number of SDMs being searched for. Column 8 lists the % error, which was calculated by taking the average % error between the input artificial galaxy and the model for all of the observable parameters, see Table 2 for more information.

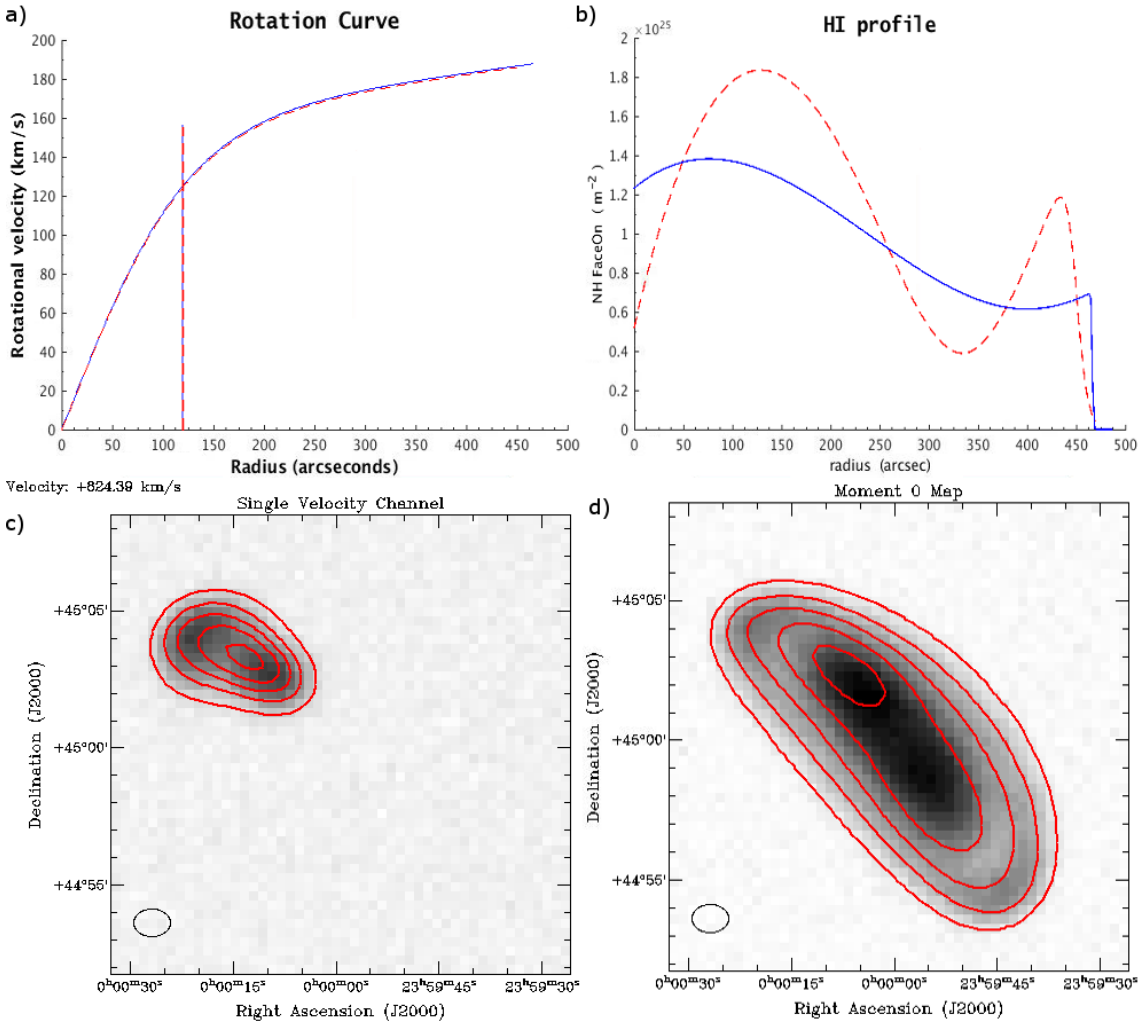

Figure 52: The input data was art3198-d (see Table 3), **with noise**. The best fit model (reduced $\chi^2 = 1.37$) produced after 1000 generations using the **non-optically thin** version of the code is shown. There were **4 SDMs** searched for. a) Input RC (R), Model RC (B). Note that the maximum difference in velocity is only 1.1 km/s. b) Input HI profile (R), Model HI profile, using 5 SDMs (B). c) Single Velocity Channel Input is the greyscale data, Model is the Red contour (3σ) overlaid, and the intensity increases by 20% of the maximum in each step. Maximum discrepancy is 1.2x the beam size. d) The zeroth moment map of the input and output models with the same contours as in c).

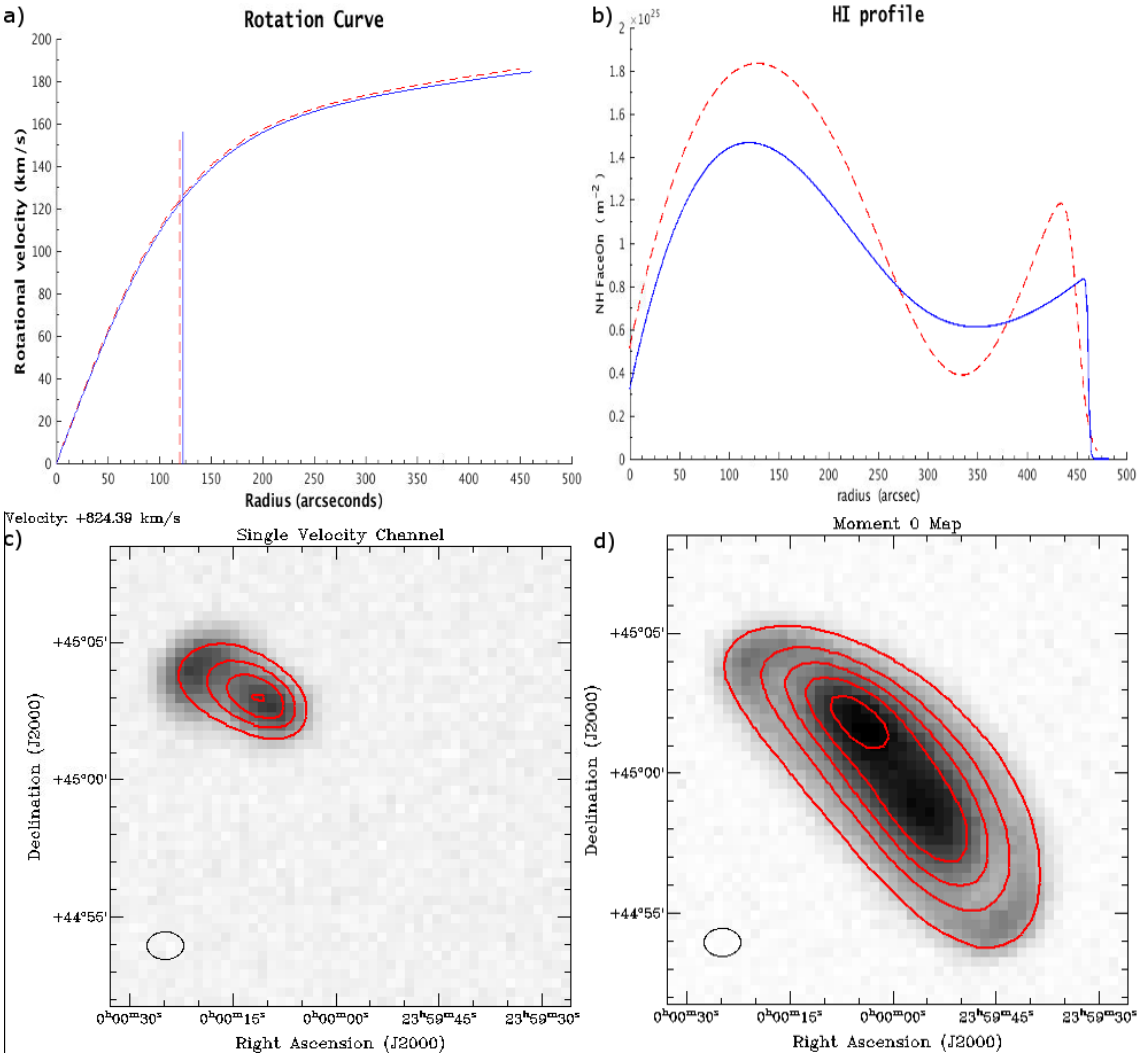

Figure 53: The input data was art3198-d (see Table 3), **with noise**. The best fit model (reduced $\chi^2 = 1.10$) produced after 1000 generations using the **non-optically thin** version of the code is shown. There were **5 SDMs** searched for. a) Input RC (R), Model RC (B). Note that the maximum difference in velocity is only 1.0 km/s. b) Input HI profile (R), Model HI profile, using 5 SDMs (B). c) Single Velocity Channel Input is the greyscale data, Model is the Red contour (3σ) overlaid, and the intensity increases by 20% of the maximum in each step. Maximum discrepancy is 1.0x the beam size. d) The zeroth moment map of the input and output models with the same contours as in c).

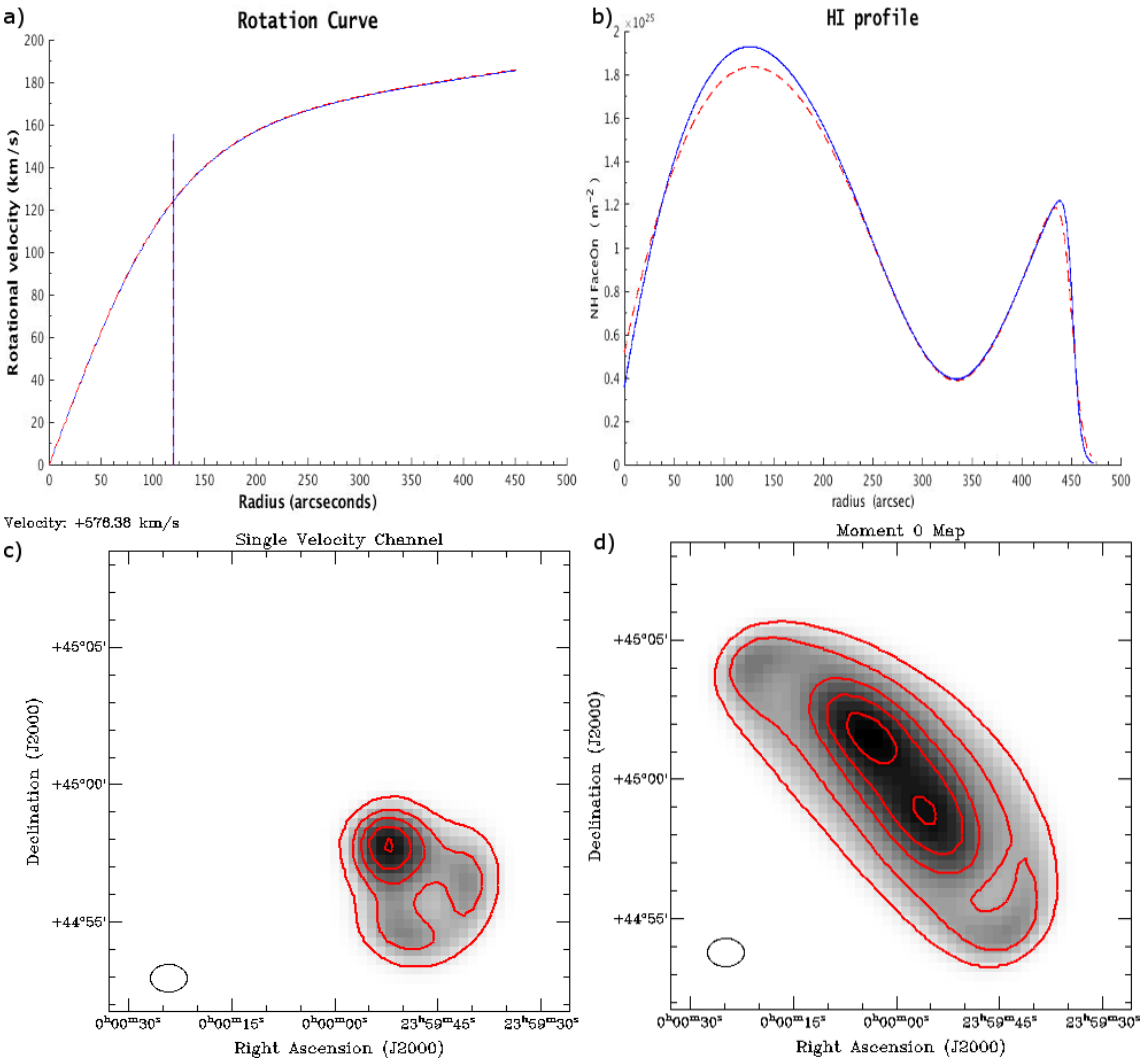

Figure 54: The input data was art3198-d (see Table 3), **without noise**. The best fit model (reduced $\chi^2 = 3.09 \times 10^{-4}$) produced after 1000 generations using the **non-optically thin** version of the code is shown. There were **6 SDMs** searched for. a) Input RC (R), Model RC (B). Note that the maximum difference in velocity is only 0.04 km/s. b) Input HI profile (R), Model HI profile, using 6 SDMs (B). c) Single Velocity Channel Input is the greyscale data, Model is the Red contour (3σ) overlaid, and the intensity increases by 20% of the maximum in each step. Maximum discrepancy is 0.01x the beam size. d) The zeroth moment map of the input and output models with the same contours as in c).

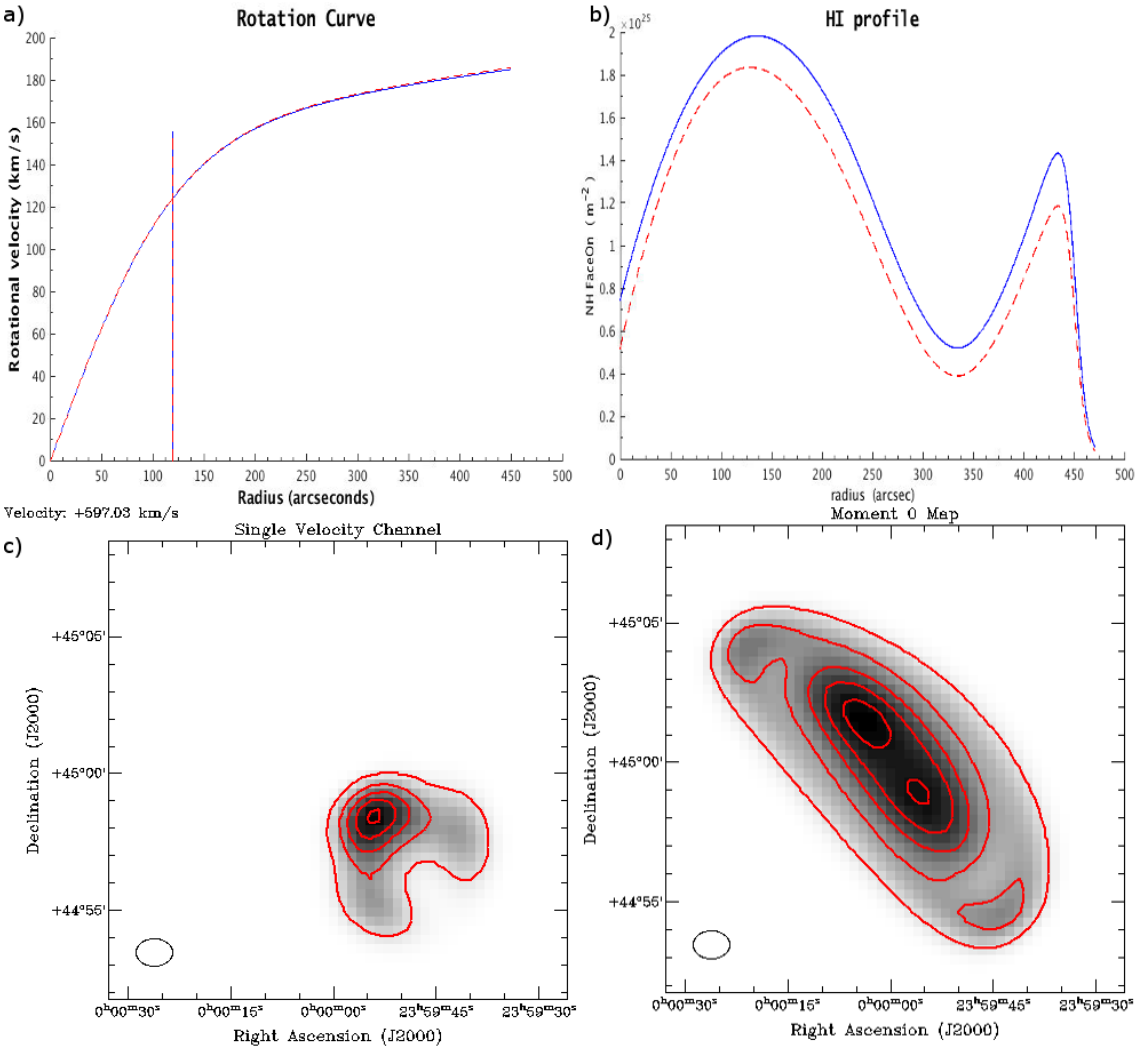

Figure 55: The input data was art3198-d (see Table 3), **without noise**. The best fit model (reduced $\chi^2 = 0.0026$) produced after 1000 generations using the **optically thin** version of the code is shown. There were **6 SDMs** searched for. a) Input RC (R), Model RC (B). Note that the maximum difference in velocity is only 0.05 km/s. b) Input HI profile (R), Model HI profile, using 6 SDMs (B). c) Single Velocity Channel Input is the greyscale data, Model is the Red contour (3σ) overlaid, and the intensity increases by 20% of the maximum in each step. Maximum discrepancy is 0.9x the beam size. d) The zeroth moment map of the input and output models with the same contours as in c).

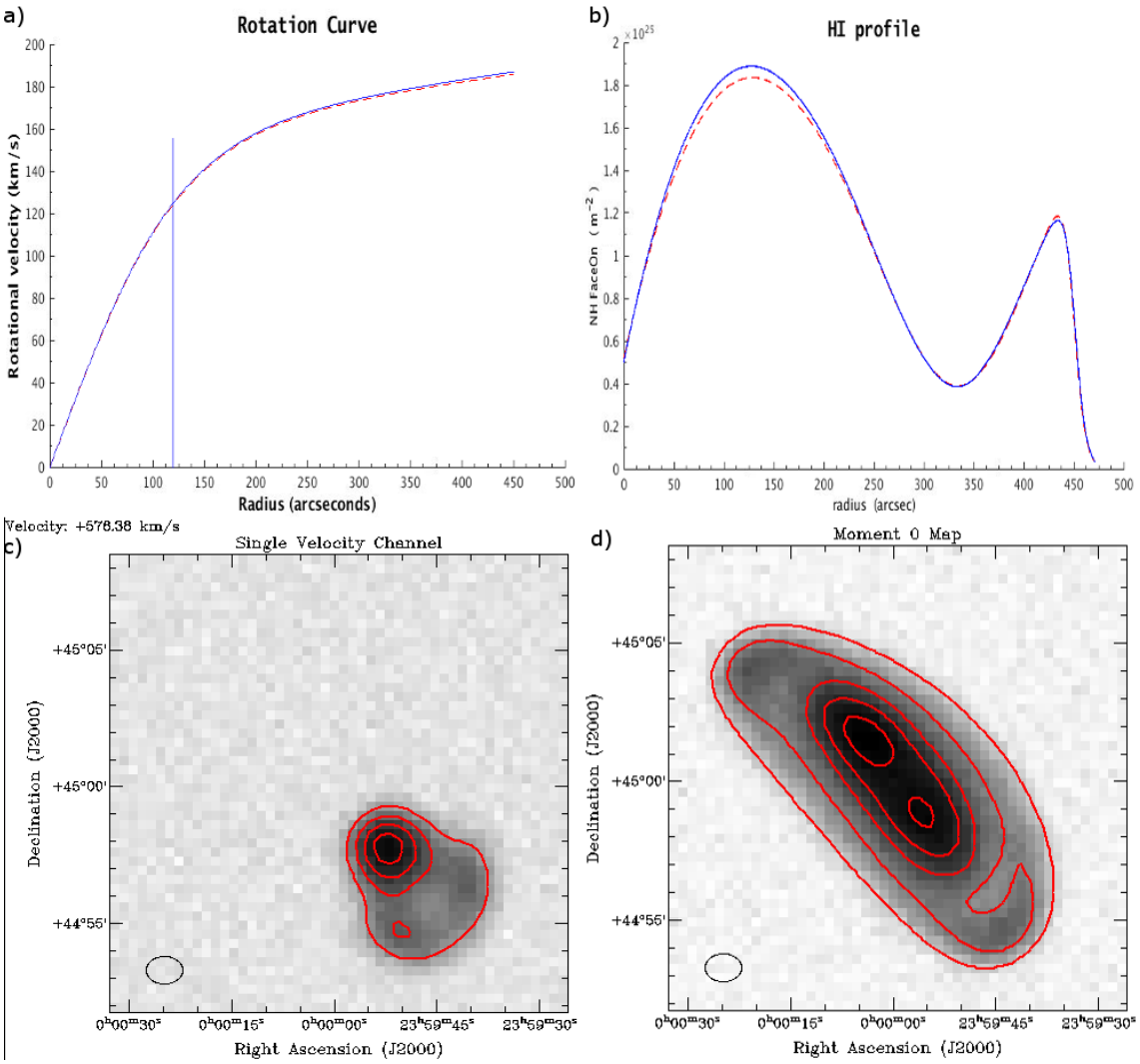

Figure 56: The input data was art3198-d (see Table 3), **with noise**. The best fit model (reduced $\chi^2 = 0.93$) produced after 1000 generations using the **non-optically thin** version of the code is shown. There were **6 SDMs** searched for. a) Input RC (R), Model RC (B). Note that the maximum difference in velocity is only 0.3 km/s. b) Input HI profile (R), Model HI profile, using 6 SDMs (B). c) Single Velocity Channel Input is the greyscale data, Model is the Red contour (3σ) overlaid, and the intensity increases by 20% of the maximum in each step. Maximum discrepancy is 0.3x the beam size. d) The zeroth moment map of the input and output models with the same contours as in c).

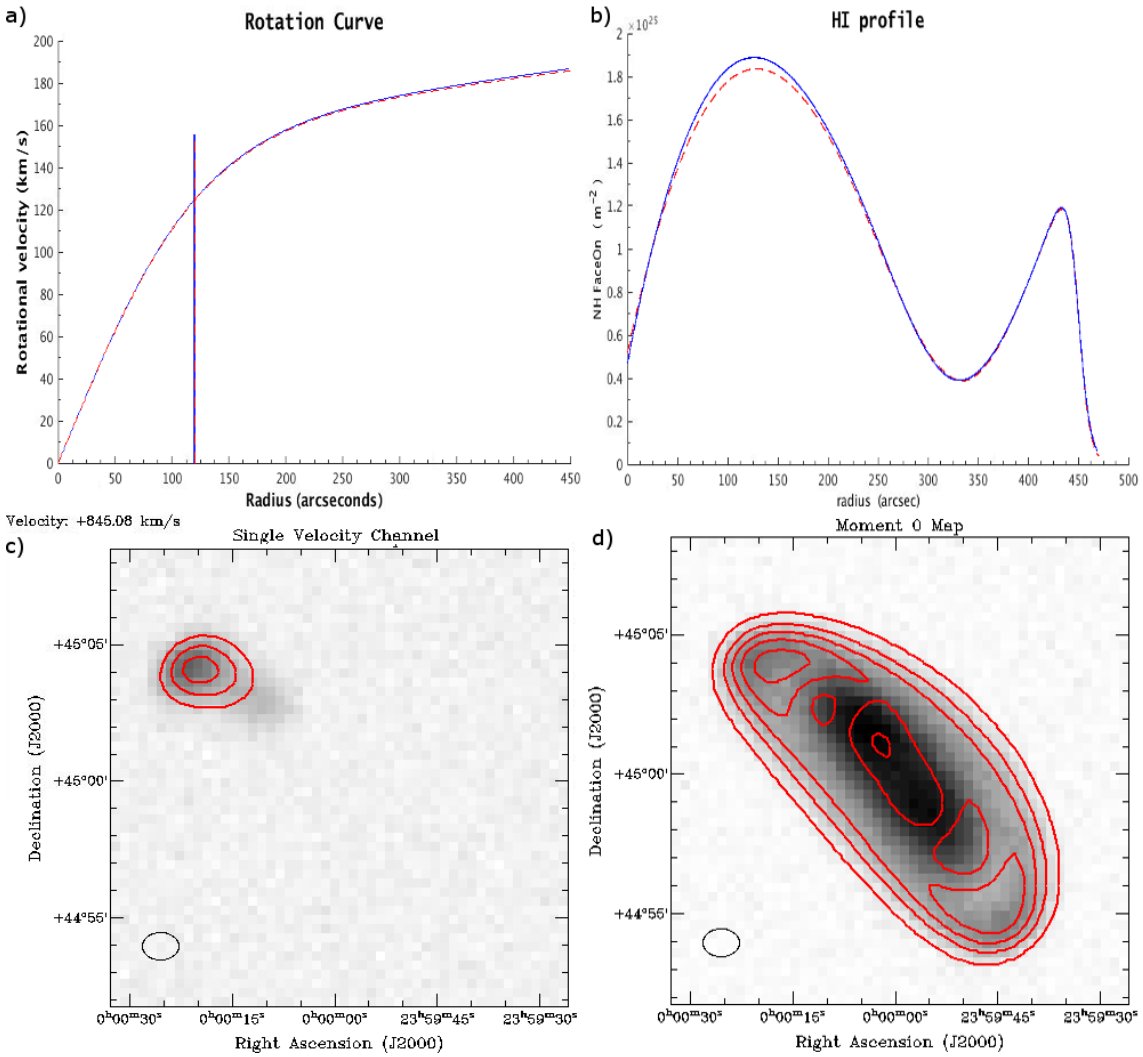

Figure 57: The input data was art3198-d (see Table 3), **with noise**. The best fit model (reduced $\chi^2 = 0.93$) produced after 1000 generations using the **non-optically thin** version of the code is shown. There were **8 SDMs** searched for. a) Input RC (R), Model RC (B). Note that the maximum difference in velocity is only 0.2 km/s. b) Input HI profile (R), Model HI profile, using 8 SDMs (B). c) Single Velocity Channel Input is the greyscale data, Model is the Red contour (3σ) overlaid, and the intensity increases by 20% of the maximum in each step. Maximum discrepancy is 1.3x the beam size. d) The zeroth moment map of the input and output models with the same contours as in c).

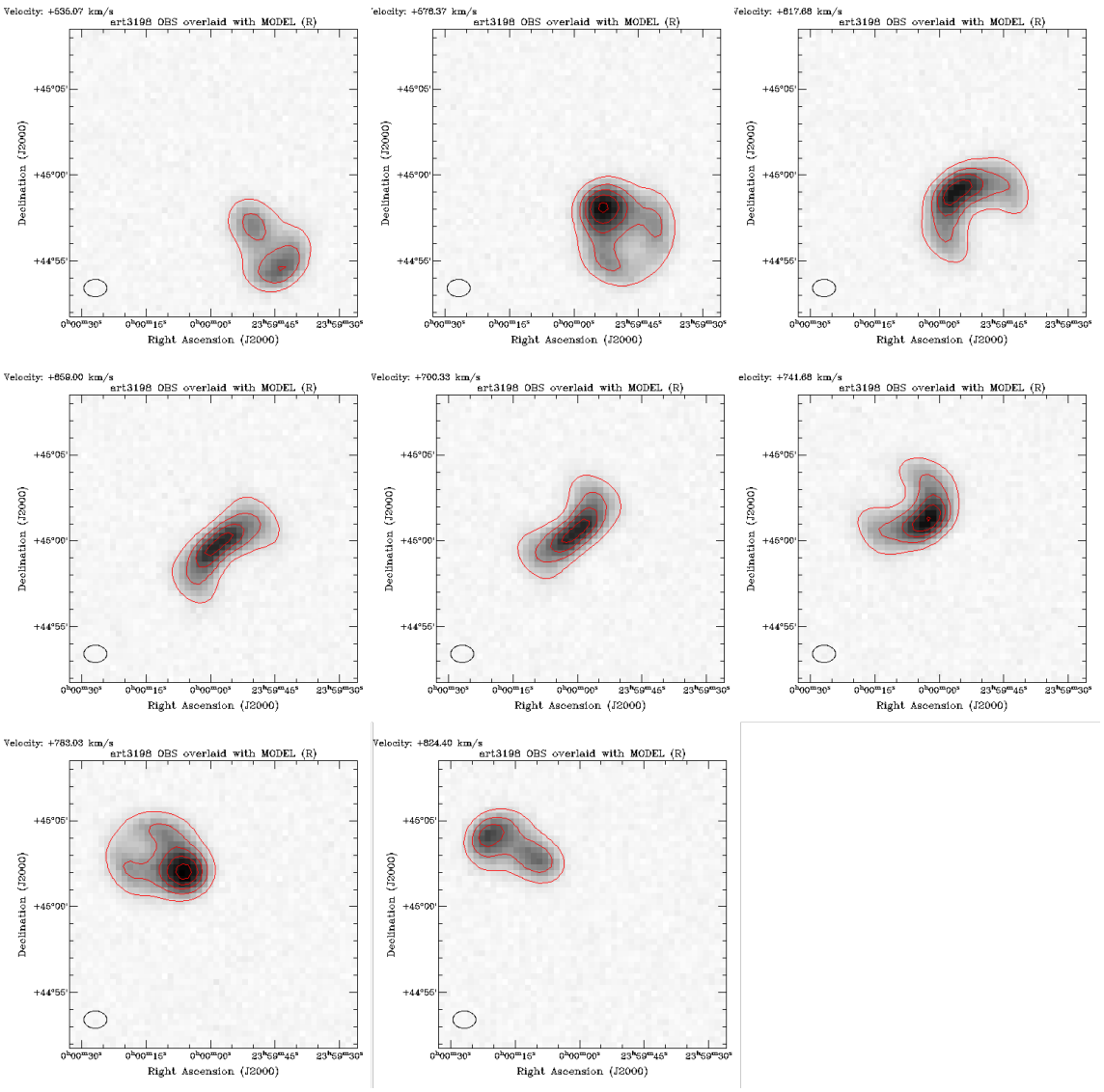

Figure 58: The input data was art3198-d (see Table 3), with noise. The best fit model (reduced $\chi^2 = 0.93$) produced after 1000 generations using the non-optically thin version of the code is shown. There were 6 SDMs searched for. The greyscale data is the input art3198-d, and the red contours represent the model. Again, the minimum contour is at the 3σ level, and increase by 20% of the maximum with each step.

B Computer Information

The primary computers used for this project consisted of:

Champion:

- Dual CPU (Six-Core AMD Opteron Processor 2439 SE, 2.793 GHz)x2;
- Ten cores were used at a time during runs, keeping two available to run a separate MATLAB session for analysis;
- 32 GB RAM; and
- Scientific Linux release 6.9 (Carbon).

Dalek:

- CPU (Six-Core AMD Opteron Processor 2439 SE, 2.793 GHz)x2;
- Ten cores were used at a time during runs, keeping two available to run a separate MATLAB session for analysis;
- 32 GB RAM; and
- Scientific Linux release 6.9 (Carbon).

Hydra:

- CPU (Eight-Core AMD Opteron Processor 6376)x4;
- Thirty cores were used at a time during runs, keeping two available to run a separate MATLAB session for analysis;
- 64 GB RAM; and
- Scientific Linux release 6.9 (Carbon).

Bibliography

Optimization through evolution and recombination, 1962.

The DiVAs Mask: Iconifying Galaxies and Revealing HI Anomalies, New York, 2010. Springer Science + Business Media, LLC 2010.

The atlas^{3D} project - iii. a census of the stellar angular momentum within the effective radius of early-type galaxies: unveiling the distribution of fast and slow rotators. *Monthly Notices of the Royal Astronomical Society*, 414, 2011.

Cds portal. http://cdsportal.u-strasbg.fr/?target=NGC Accessed: 2017-11-06.

Cds portal. http://cdsportal.u-strasbg.fr/?target=NGC Accessed: 2017-11-06.

Nrao image gallery. http://images.nrao.edu/Galaxy/Peculiar/116, 2017. Accessed: 2017-10-25.

A. Abragam and W. G. Proctor. Spin temperature. *Physical Review*, 109, 1958.

A. Abramson, J. D. P. Kenney, H. H. Crowl, A. Chung, J. H. Van Gorkom, B. Vollmer, and D. Schiminovich. Caught in the act: Strong, active ram pressure stripping in virgo cluster spiral ngc 4330. *The Astronomical Journal*, 141, 2011.

K. Alatalo et al. The atlas^{3D} project - xvii. carma co imaging survey of early-type galaxies. *Monthly Notices of the Royal Astronomical Society*, 432, 2013.

J. Sanchez Almeida, B. G. Elmegreen, C. Munoz-Tunon, and D. M. Elmegreen. Star formation sustained by gas accretion. *The Astronomy and Astrophysics Review*, 22, 2014.

R. Andrae, T. Schulze-Hartung, and P. Melchior. Dos and don'ts of reduced chi-squared. *ArXiv e-prints*, December 2010.

Space and Spaceball, volume 77, San Fransisco, 1995a. ASP Conf. Series, R. A. Shaw, H. E. Payne, and J. J. E. Hayes, ASP.

A Retrospective View Of MIRIAD, volume 77, San Fransisco, 1995b. ASP Conf. Series, R. A. Shaw, H. E. Payne, and J. J. E. Hayes, ASP.

J. Bak and T. S. Statler. The intrinsic shape distribution of a sample of elliptical galaxies. *The Astronomical Journal*, 120, 2000.

K. Begeman. *HI rotation curves of spiral galaxies.* PhD thesis, University of Groningen, 1987.

K. G. Begeman, A. H. Broeils, and R. H. Sanders. Extended rotation curves of spiral galaxies - dark haloes and modified dynamics. *Monthly Notices of the Royal Astronomical Society*, 249:523, 1991.

C. L. Bennet et al. Nine-year wilkinson microwave anisotropy probe (wmap) observations: Final maps and results. *The Astrophysical Journal Supplement*, 208, 2013.

Gianfranco Bertone. *Particle Dark Matter: Observations, Models and Searches.* Cambridge University Press, first edition, 2010.

P. R. Bevington and D. K Robinson. *Data Reduction and Error Analysis.* McGraw-Hill, third edition, 2003.

J. Binney and M. Merrifield. *Galactic Astronomy.* Princeton University Press, first edition, 1983a.

J. Binney and M. Merrifield. *Galactic Astronomy.* Princeton University Press, first edition, 1983b.

R. Braun. The cosmic web in focus. *Nature*, 497:191–192, 2013.

M. Cappellari. Anisotropic jeans models of stellar kinematics: second moments including proper motions and radial velocities. *Monthly Notices of the Royal Astronomical Society*, 2012.

M. Cappellari et al. The atlas^{3D} project - xx. mass-size and mass-sigma distributions of early-type galaxies: bulge fraction drives kinematics, mass-to-light ratio, molecular gas

fraction and stellar initial mass function. *Monthly Notices of the Royal Astronomical Society*, 432, 2013b.

Planck Collaboration. Planck 2015 results. *Astronomy and Astrophysics*, 594, 2016.

A. Crocker et al. The atlas^{3D} project - xi. dense molecular gas properties of co-luminous early-type galaxies. *Monthly Notices of the Royal Astronomical Society*, 421:1298–1314, 2012.

T. A. Davis et al. The atlas^{3D} project - xiv. the extent and kinematics of the molecular gas in early-type galaxies. *Monthly Notices of the Royal Astronomical Society*, 429, 2013.

W. J. G. de Blok. Review article: The core-cusp problem. *Advances in Astronomy*, 2010. Article ID 789293.

W. J. G. de Blok, S. S. McGaugh, and J. M. van der Hulst. Hi observations of low surface brightness galaxies: Probing low density galaxies. *Monthly Notices of the Royal Astronomical Society*, 283:18–54, 1996.

W. J. G de Blok, F. Walter, E. Brinks, C. Trachternach, S-H. Oh, and R. C. Kennicutt Jr. High-resolution rotation curves and galaxy mass models from things. *The Astronomical Journal*, 136:2648–2719, 2008.

A. Dekel and Y. Birnboim. Galaxy bimodality due to cold flows and shock heating. *Monthly Notices of the Royal Astronomical Society*, 368:2–20, 2006.

H. Domgorgen, M. Dahlem, and R.-J. Dettmar. What perturbs ngc 2188? *Astronomy and Astrophysics*, 313:96–100, 1996.

J. Dubinsky and R. G. Carlberg. The structure of cold dark matter halos. *The Astrophysical Journal*, 378:496–503, 1991.

A. E. Eiben and J. E. Smith. *Introduction to Evolutionary Computing*. Springer Heidelberg New York Dordrecht London, second edition, 2015.

J. Einasto. Dark matter, 2010.

E. Emsellem, G. Monnet, and R. Bacon. The multi-gaussian expansion method: a tool for building realistic photometric and kinematical models of stellar systems i. the formalism. *Astronomy and Astrophysics*, 285:723–738, 1994.

P. Fernique, M. G. Allen, T. Boch, F. X. Pineau, D. Durand, C. Bot, L. Cambresy, S. Derriere, F. Genova, and F. Bonnarel. Hierarchical progressive surveys. multi-resolution healpix data structures for astronomical images, catalogues, and 3-dimensional data cubes. *Astronomy and Astrophysics*, 578, 2015.

Jason Fiege. *Qubist User's Guide*, 2010. URL `www.nqube.com`.

L. J. Fogel, A. J. Owens, and M. J. Walsh. *Artificial Intelligence through Simulated evolution*. Wiley, 1966.

F. Fraternali, G. van Moorsel, R. Sancisi, and T. Oosterloo. *The Astrophysical Journal*, 123:3124, 2002.

R. Genzel, N. M. Forster Schreiber, H. Ubler, P. Lang, R. Bender, L. J. Tacconi, E. Wisnioski, S. Wuyts, T. Alexander, A. Beifiori, S. Belli, G. Brammer, A. Burkert, C. M. Carollo, J. Chan, R. Davies, M. Fossati, A. Galametz, S. Genel, O. Gerhard, D. Lutz, J. T. Mendel, I. Momcheva, E. J. Nelson, A. Renzini, R. Saglia, A. Sternberg, S. Tacchella, K. Tadaki, and D. Wilman. Strongly baryon-dominated disk galaxies at the peak of galaxy formation ten billion years ago. *Nature*, 543:397–401, 2017.

P. F. Goldsmith. Collisional excitation of carbon monoxide in interstellar clouds. *The Astrophysics Journal*, 176:597–610, 1972.

Carl Heiles. Hi shells and supershells. *The Astrophysical Journal*, 229:533–544, 1979.

Fast and Slow Rotators: The Build-up of the Red Sequence, 2007. IAU symposium No. 247.

J. H. Jeans. The motions of stars in a kapteyn universe. *Monthly Notices of the Royal Astronomical Society*, 82:22–32, 1922.

K. A. De Jong. *An Analysis of the Behaviour of a Class of Genetic Adaptive Systems*. PhD thesis, University of Michigan, 1975.

E. M. Kirby, B. Koribalski, K. Helmut, and A. Lopez-Sanchez. The local volume hi survey: Galaxy kinematics. *Monthly Notices of the Royal Astronomical Society*, 420: 2924–2943, 2011.

M. B. N. Kouwenhoven, M. Bureau, S. Kim, and P. T. de Zeeuw. Optical bvi imaging and hi synthesis observations of the dwarf irregular galaxy eso 364-g029. *Astronomy and Astrophysics*, 470:123–135, 2007.

S. W. Lee and J. A. Irwin. Neutral hydrogen in the edge-on spiral galaxy ngc 3044 - global properties and discovery of hi supershells. *The Astrophysical Journal*, 490: 247–262, 1997.

K. Y. Lo, T. G. Phillips, G. R. Knapp, H. A. Wootten, and H. A. Huggins. Optically thin co emission from m82 and ngc 253. *Bulletin of the American Astronomical Society*, 12, 1980.

T. P. K. Martinsson, M. A. W. Verheijen, M. A. Bershady, K. B. Westfall, D. R. Andersen, and R. A. Swaters. The diskmass survey. x. radio synthesis imaging of spiral galaxies. *Astronomy and Astrophysics*, 585:Article A99, P. 15, 2015.

M. J. Meyers, M. A. Zwaan, R. L. Webster, et al. The hipass catalogue - i. data presentation. *Monthly Notices of the Royal Astronomical Society*, 350:1195–1209, 2004.

E. J. Murphy, J. D. P. Kenney, G. Helou, A. Chung, and J. H. Howell. Environmental effects in clusters: Modified far-infrared-radio relations within virgo cluster galaxies. *The Astrophysical Journal*, 694:1435–1451, 2009.

J. F. Navarro, C. S. Frenk, and S. D. M. White. A universal density profile from heirarchical clustering. *The Astrophysical Journal*, 490:493–508, 1997.

K. Onishi, S. Iguchi, T. A. Davis, M. Bureau, M. Cappellari, M. Sarzi, and L. Blitz. Wisdom project - i: Black hole mass measurement using molecular gas kinematics in

ngc 3665. *Monthly Notices of the Royal Astronomical Society in Press*, pages 1–12, 2017a.

K. Onishi, S. Iguchi, T. A. Davis, M. Bureau, M. Cappellari, M. Sarzi, and L. Blitz. Wisdom project - i: Black hole mass measurement using molecular gas kinematics in ngc 3665. *Monthly Notices of the Royal Astronomical Society in Press*, page 11, 2017b.

J. Pearl. *Heuristics: intelligent search strategies for computer problem solving*. United States: Addison-Wesley Pub. Co., Inc., 1984.

I. Rechenberg. Evolutionstrategie: Optimierung technisher systeme nach prinzipien des biologischen evolution. *Frommann-Hollboog Verlag, Stuttgart*, 1973.

D. H. Rogstad, I. A. Lockhart, and M. C. H. Wright. Aperture-synthesis observations of hi in the galaxy m83. *The Astrophysics Journal*, 193:309, 1974.

M. P. Rupen. Spectral line observing ii: Calibration and analysis. *Synthesis Imaging in Radio Astronomy II*, 180:229, 1999.

F. J. Sicking. *The thickness of the HI gas layer in spiral galaxies*. PhD thesis, University of Groningen, 1997.

L. S. Sparke and J. S. Gallagher. *Galaxies in the Universe: An Introduction*. Cambridge University Press, second edition, 2007.

R. B. Tully. *Nearby galaxies catalog*. Cambridge and New York, Cambridge University Press, 1988.

F. Walter, E. Brinks, W. J. G. de Blok, F. Bigiel, R. C. Kennicutt, M. D. Thornley, and A. K. Leroy. Things: The hi nearby survey. *The Astronomical Journal*, 136:2563–2647, 2008.

D. C. Wells, E. W. Greisen, and R. H. Harten. Fits: A flexible image transport system. *Astronomy and Astrophysics Supplement Series*, 44:363–370, 1981.

Theresa Wiegert. *Spiral galaxy HI models, rotation curves and kinematic classifications*. PhD thesis, University of Manitoba, 2011a.

Theresa Wiegert. *Spiral galaxy HI models, rotation curves and kinematic classifications*. PhD thesis, University of Manitoba, 2011b.

J. P. Williams, L. Blitz, and C. F. McKee. The Structure and Evolution of Molecular Clouds: from Clumps to Cores to the IMF. *Protostars and Planets IV*, page 97, May 2000.

Haifeng Yang, Zhi-Yun Li, Leslie W. Looney, Josep Girart, and Ian Stephens. Scattering-produced (sub)millimeter polarization in inclined disks: Optical depth effects, near-far side asymmetry, and dust settling. 05 2017.

M. S. Yun, P. T. P. Ho, and K. Y. Lo. A high-resolution image of atomic hydrogen in the m81 group of galaxies. *Nature*, 372:530–532, 1994.

M. V. Zombeck. *Radio Astronomy*. Cambridge University Press, first edition, 2006.

F. Zwicky. Die rotverschiebung von extragalaktischen neblen. *Helvetica Physica Acta*, 6: 110, 1933.

Glossary

a_v outer slope of the rotation curve.

dr_{Out} derived width of the outer fall of the surface density profile.

r_{0v} scaling factor to control the position of the turnover radius.

r_{Out} outer radius of the galaxy, derived from the mask aperture.

v_0 asymptotic velocity amplitude for $a_v = 0$.

v_{cm} the average velocity a galaxy is moving relative to the Sun.

brightness temperature the temperature of a blackbody that would emit the same intensity as is measured from the astronomical object.

column density total the number of particles, within a specified unit area, summed along a line-of-sight velocity range. In our case this is the number of particles within 1 square metre integrated along a column with the length of the velocity range of the data cube..

density profile the galaxy's column density as a function of radius.

effective radius the radius at which half of the total light of the system is emitted.

evolutionary algorithm class of techniques for finding the global best solution or set of solutions inspired by the process of natural evolution.

family of solutions an optimal set of solutions consisting of many single sets of parameters (a model), each distinct from each other numerically, although indistinguishable statistically due to the noise in the data.

fitness function evaluates how close any given intermediate solution is to the optimal solution of the problem.

GalAPAGOS position angle the angle of the galaxy's major axis measured clockwise from the south celestial pole.

global minimization is the principle of finding the optimal solution or set of solutions within the entire parameter space and subject to one or more objectives and all applicable constraints involved in the problem to be solved.

heuristic approach a heuristic function [also called a heuristic] ranks alternatives in search algorithms at each branching step based on available information to decide which branch to follow.

inclination the angle with respect to the plane of the sky of a galaxy disk's tilt. Edge-on: $inc = 90°$; Face-on $inc = 0°$.

large scale structure the structure of the universe on scales larger than that of a galaxy.

mask buffer radius sets the minimum radius for the number of pixels not to be masked after a bright pixel is found in each velocity channel.

mask velocity buffer sets the minimum number of velocity channels in which a pixel is not masked after a bright pixel is found.

metaheuristic a heuristic designed to find, generate, or select a heuristic.

minimum neighbour fraction sets the minimum fraction for the number of nearest neighbours searched relative to a bright pixel.

model a singular set of parameters.

molecular cloud an interstellar region dense enough to form molecules such as H_2 and CO, from which stars may be formed. Also known as stellar nurseries.

moment 0 map an integrated intensity map made by collapsing the data cube along the velocity axis. It can be taken as a measure of the column density.

moment 1 map a velocity field map, made by collapsing the data cube along the velocity axis and weighting by intensity. It can be taken as a measure for the mean velocity of the gas.

optical depth measure of the amount of absorption that occurs when light travels through a medium.

position angle the angle of the galaxy's major axis measured counter clockwise from the north celestial pole.

renzogram a plot of the same single intensity iso-contour (with the intensity contour level set by the user) from multiple velocity channels. These contours are typically overlaid on a single channel or moment map. Each velocity channel has a different

colour (chosen by the user) assigned to the contour. This allows the user to examine the velocity distribution of a particular feature throughout selected velocity ranges in the galaxy..

rotation curve the distribution of the radial velocity of a galaxy as a function of the distance from the galaxy's center corrected for the inclination of the galaxy to the observer's line of sight.

S/N edge threshold sets the lower limit on the desired signal to noise value, used to detect regions in the cube with signal.

scale height the vertical distance over which the density and pressure fall by a factor of 1/e.

SDM a vector of a user chosen number of values ranging from -1 to 1, corresponding to the Surface Density Modulation values.

spin temperature the temperature that would produce the observed ratio of parallel to antiparallel spins if the HI gas were in thermal equilibrium.

superbubbles bubbles in the interstellar medium associated with supernovae which can expand and break to become a chimney, or conduit for gas outflow.

tidal tails a thin, elongated region of stars and gas stretching out from the interacting galaxy's disk.

virial radius the radius at which objects will be gravitationally bound to a galaxy and will settle into regular orbits.

voxel is a value on a regular grid in three-dimensional space, and is analogous to a pixel in a bitmap.

voxel search radius sets the radius for the number of voxels searched relative to a bright (high brightness temperature) voxel.